

Rheological and Colloidal Approaches to Characterizing and Producing Dispersions for Advanced Manufacturing

A Dissertation

Presented to

the faculty of the School of Engineering and Applied Science

University of Virginia

in partial fulfillment

of the requirements for the degree

Doctor of Philosophy

by

Matthew A. Diasio

December 2019

Abstract

Products made from particles and polymers are found everywhere in modern life. Seventy percent of all polymers contain particles whose dispersion optimizes desirable properties. Colloidal and interfacial phenomena drive important processes in industries from food processing to pharmaceuticals to petrochemicals. Novel multifunctional fluids and composites can be developed from new colloid systems. In this dissertation, I use rheological techniques and colloid theory to investigate novel manufacturing processes.

The first task was to study the use of ultraviolet (UV)-curable polymeric coatings for electroplating processes. UV-curable polymers provide many potential benefits as coatings for the manufacturing of metallic parts, especially through the reduced time and labor costs of applying them in comparison to other material systems. Automated application of UV-curable coatings would enable significant further cost and time savings. Automation requires a more detailed understanding of the mechanical and interfacial properties of the maskants before and after curing. The shorter-chained burn-off materials showed greater adhesion and resistance to plating species than their peel-off counterparts. The focus on macro scale parts and the maskant mechanical properties represent a novel contribution to the UV-curable coating literature.

The second process studied was the liquid-phase exfoliation of graphite into the two-dimensional nanomaterial graphene. There has been an explosion of interest in two-dimensional nanomaterials generally because of their many outstanding properties. A major limit in the practical use of graphene is the synthesis of large amounts with the desired properties, such as electronic conductivity or flake size. Liquid-phase exfoliation by shear is especially attractive because it is scalable and produces significantly fewer defects than older methods based on ultrasonication. I have evaluated liquid viscosity and dielectric constant as previously unstudied parameters relevant to the production of few-layer graphene by liquid-phase shear exfoliation and which could explain observations that the surface tension framework fails to describe. Through a rheological study, I demonstrated that a higher viscosity liquid, propylene glycol (PG), can produce more few-layer graphene by shear exfoliation than a lower viscosity liquid, the standard graphene solvent N-methyl-2-pyrrolidone (NMP), under identical conditions. This was followed up by a larger-scale study in an industrial impeller mixer, where PG produced equivalent quality material compared to that exfoliated in NMP, and at higher concentrations at all exfoliation times. Additionally, graphene dispersions in PG showed similar dispersion stability to those in NMP over the course of 160 hours and a greater predicted stability based on the second virial coefficient of the dispersions.

This work on few-layer graphene produced by exfoliation should be generalizable to other two-dimensional nanomaterials. The fuller understanding of exfoliation and dispersion stability provided will enhance solvent selection and design for exfoliation of specific materials with characteristics tailored to specific applications. Additionally, these dispersions may be useful multifunctional high-performance fluids for applications like heat transfer or lubrication or as “inks” for manufacturing. They can also be a platform for further chemical modification of graphene and other 2D nanomaterials.

This dissertation is dedicated to the memory of my grandparents:

Thomas and Yolanda Diasio

and

Benedict and Bernadette Joy

Acknowledgements

Working on a dissertation is a long process, and over the many years I've been here, I was fortunate to be supported by many groups and people. I can't possibly name them all, but I would like to recognize some who have been especially helpful on this journey. First, I want to thank my incredibly supportive parents, Robert and Monica, who have been my cheerleaders, my sounding board, and so many other helpful things for all my life and especially through graduate school. I want to thank Dr. David Green, for letting me work in his lab as I sought a transition at the end of my second year of grad school and then for taking me on as one of his students. Dr. Green's mentorship in colloid science and rheology has exposed me to so many other fascinating aspects of nanoscience and materials science, and I've appreciated the flexibility he has given me in my dissertation research. To Dr. Petra Reinke, thank you so much for your mentorship and your willingness to discuss my research when I needed to consider a problem in a new way. I also wish to thank the rest of my dissertation committee, Dr. Eric Loth, Dr. Stephen McDonnell, and Dr. Prasanna Balachandran for other helpful conversations about my work and potential future directions.

To my old friends from before and the new friends I have made in graduate school, whether in Charlottesville or beyond, I truly appreciate any support you've given me and listing all the ways I valued our interactions could be another dissertation in itself. Shadi (or I suppose now Dr. Khalil), I'm glad we were able to meet each other when we were at such similar points in our programs and I've treasured our conversations as scientists and good friends. To Steve (now Dr. Merz) I want to thank you for being such a great colleague during our time together in the Green lab. For as different as our work was, it was always helpful to bounce ideas off you. LeighAnn, I've enjoyed our MSE bonding in everything we ended up doing outside of MSE and I'm excited that we're now Team #AggressivelyDissertating. And to the members of the Graduate Engineering Student Council, Science Policy Initiative, and the Jefferson Literary and Debating Society, thank you for supporting the groups that let me explore myself in graduate school and providing the spaces for some of my favorite moments here.

Table of Contents

1. Introduction	8
1.1 References for Introduction.....	10
2. Characterizing UV-Curable Maskants for Automated Application on Aerospace Turbine Blades	12
Abstract.....	12
2.1 Introduction	12
2.2 Methods.....	15
2.2.1 Materials	15
2.2.2 Characterization of Uncured Maskants	16
2.2.3 Characterization of Cured Maskants.....	17
2.3 Results.....	19
2.3.1 Behavior of Uncured Maskants.....	19
2.3.2 Hardness	22
2.3.3 Adhesion and Cohesion	23
2.3.4 Maskant Application, Platinum Plating, and Post-Plating Inspection.....	26
2.4 Analysis	27
2.5 Conclusions	28
2.6 Acknowledgements.....	28
2.7 References for Chapter 2	28
Appendix A: Curing, Adhesion, and Pull-Off Experimental Data	30
A.1 Rates of Cure.....	30
A.1.1 Methods.....	30
A.1.2 Results and Analyses.....	31
A.2 Adhesion	36
3. Graphene, Its Colloids, and Their Applications	43
Abstract.....	43
3.1 Graphene	44
3.1.1 Potential Applications of Graphene	45
3.1.2 Graphene Production.....	46
3.2 Graphene Colloids.....	49
3.3 Interaction Forces in Colloids.....	56
3.4 Motivation.....	61

3.4.1	Functionalization of Graphene.....	61
3.4.2	Future Solvents: Designed Ionic Liquids	64
3.5	References for Chapter 3	66
4.	Rheological Investigation of Few-Layer Graphene Production by Shear Exfoliation of Graphite	72
	Abstract.....	72
4.1	Introduction	73
4.2	Methods.....	75
4.2.1	Materials	75
4.2.2	Exfoliation	75
4.2.3	Characterization.....	76
4.3	Results.....	76
4.3.1	UV-Visual spectroscopy.....	76
4.3.2	Quality of Exfoliated Material.....	78
4.4	Conclusions	79
4.5	Acknowledgements.....	80
4.5	References for Chapter 4	80
5.	Producing Few-Layer Graphene by Shear Exfoliation in a Viscous Liquid in a Large-Scale Mixer	83
	Abstract.....	83
5.1	Introduction	83
5.2	Methods.....	85
5.2.1	Exfoliation	85
5.2.2	Ultraviolet-Visual Spectroscopy.....	86
5.2.3	Morphology Characterization	88
5.3	Results.....	89
5.3.1	Ultraviolet-Visual Spectroscopy.....	89
5.3.2	Morphology.....	94
5.4	Conclusions	99
5.5	Acknowledgments.....	99
5.6	References for Chapter 5	99
6.	Conclusions	103
6.1	Summary	103
6.1.1	UV-Curable Maskants for Electroplating	103
6.1.2	Graphene Production by Liquid-Phase Shear Exfoliation	103

6.2 Future Work.....	104
6.2.1 UV-Curable Maskants for Electroplating	104
6.2.2 Two-Dimensional Nanomaterial Production by Liquid-Phase Shear Exfoliation	105
6.3 Final Remarks.....	108
6.4 References for Conclusions.....	109

1. Introduction

Products made from particles and polymers are found everywhere in modern life. In fact, seventy percent of all polymers contain particles whose dispersion optimizes desirable properties. For example, paints, coatings, and lotions, among other consumer products, are all engineered to effectively disperse chemicals or materials of interest. Colloidal and interfacial phenomena drive important processes in industries from food processing to pharmaceuticals to petrochemicals¹. Novel multifunctional composites can be developed from new colloid systems²⁻⁴. In this dissertation, I use rheological techniques and colloid theory to investigate novel manufacturing processes.

The first task was to study the use of ultraviolet (UV)-curable polymeric coatings for electroplating processes. UV-curable polymers provide many potential benefits as coatings for the manufacturing of metallic parts, especially through the reduced time and labor costs of applying them in comparison to other material systems⁵⁻⁷. Automated application of UV-curable coatings would enable significant further cost and time savings. Automation requires a more detailed understanding of the mechanical and interfacial properties of the maskants before and after curing. While extensive literature exists on UV-curable polymers, much of it focuses on those used as photoresists in lithography processes for the electronics industry. Few studies have explored the importance of mechanical properties for application to large-scale parts such as those in the aerospace and automotive industries. Through the use of multiple characterization techniques, we investigated structure-process-property relationships of UV-curable polymer resins in relation to their potential as maskants in platinum electroplating, the results of which are shown in chapter 2.

The second process studied was the liquid-phase exfoliation of graphite into the two-dimensional nanomaterial graphene. A major limit in the practical use of graphene, and 2-D

nanomaterials generally, is the synthesis of large amounts with the desired properties, such as electronic conductivity or nanoparticle size. Liquid-phase exfoliation by shear is attractive because it is scalable and potentially size-selective. Shear exfoliation also produces significantly fewer defects than prior methods based on ultrasonication⁸.

Much of the prior work on liquid-phase exfoliated graphene focuses on optimizing exfoliation by choosing solvents that have surface energies close to that of graphite/graphene mitigating their aggregation. However, the pre-existing literature shows this focus has unresolved problems, including the inability to explain differences in graphene yield and quality produced by solvents with similar surface energies and the inability to predict long-term dispersion stability of the exfoliated material^{9,10}. Colloid science shows that long-range attractive forces between particles are more effectively cancelled by matching the polarizability of the particles and the solvent, which corresponds to dispersing the particles in a solution with a matching refractive index or dielectric constant, and would improve stability by preventing aggregation. Fluid mechanics, in particular Newton's viscosity equation, also predicts elevating the viscosity of the exfoliation liquid increases the shear forces transmitted to the graphite flakes augmenting exfoliation and could improve yield. The effect of viscosity on exfoliation has not been studied until now. Hence, the work on graphene is divided into three sections.

- Chapter 3 – *Graphene, Its Colloids, and Their Applications*. This is an overview of the literature on applications driving interest in graphene and investigations into the exfoliation and dispersion of graphene in liquids. The mechanical exfoliation model of layered materials and the theory of interparticle forces in colloids are introduced to explain the respective interest in liquid viscosity and polarizability as exfoliation and dispersion parameters.

- Chapter 4 – *Rheological Investigation of Few-Layer Graphene Production by Shear Exfoliation of Graphite*. The exfoliation of graphite dispersed in liquids of various viscosities and dielectric constants is investigated through a stress-controlled rheometer. The most viscous liquid is observed to exfoliate more graphene than the “standard” solvent for liquid-phase exfoliation, based on concentrations determined by UV-visual spectroscopy.
- Chapter 5 – *Producing Few-Layer Graphene by Shear Exfoliation in a Viscous Liquid in a Large-Scale Mixer*. Exfoliation of graphite into graphene is performed using an industrial high-shear mixer in the standard and one viscous liquid. The viscous liquid is observed to exfoliate more graphene than the standard solvent at all mixing times, and the graphene produced is of similar quality and shows similar dispersion stability.

Future directions and applications for the study of both material processes are generalizable to many systems of interest in advanced manufacturing and materials development. These will be discussed in Chapter 6.

1.1 References for Introduction

1. Shaw, D. J. The colloidal state. in *Introduction to Colloid and Surface Chemistry* 1–20 (Butterworth-Heinemann Publications, 1992).
2. Shevchenko, E. V., Talapin, D. V., Murray, C. B. & O’Brien, S. Structural characterization of self-assembled multifunctional binary nanoparticle superlattices. *J. Am. Chem. Soc.* **128**, 3620–3637 (2006).
3. Yoon, M., Kim, Y. & Cho, J. Multifunctional colloids with optical, magnetic, and superhydrophobic properties derived from nucleophilic substitution-induced layer-by-layer assembly in organic media. *ACS Nano* **5**, 5417–5426 (2011).
4. Pellegrino, T. *et al.* On the development of colloidal nanoparticles towards multifunctional structures and their possible use for biological applications. *Small* **1**, 48–63 (2005).
5. Maag, K., Lenhard, W. & Loeffles, H. New UV curing systems for automotive applications. *Prog. Org. Coatings* **40**, 93–97 (2000).

6. Nudelman, A. K. New Options for Masking of Medical Devices — UV Curable Masks. *BONEZone* 47–51 (2004).
7. Nudelman, A. UV curable masking resins come of age. *Met. Finish.* **101**, 65–71 (2003).
8. Paton, K. R. *et al.* Scalable production of large quantities of defect-free few-layer graphene by shear exfoliation in liquids. *Nat. Mater.* **13**, 624–630 (2014).
9. Hernandez, Y., Lotya, M., Rickard, D., Bergin, S. D. & Coleman, J. N. Measurement of Multicomponent Solubility Parameters for Graphene Facilitates Solvent Discovery. *Langmuir* **26**, 3208–3213 (2010).
10. Shen, J. *et al.* Liquid Phase Exfoliation of Two-Dimensional Materials by Directly Probing and Matching Surface Tension Components. *Nano Lett.* **15**, 5449–5454 (2015).

2. Characterizing UV-Curable Maskants for Automated Application on Aerospace Turbine Blades

Abstract

UV-curable polymers provide many potential benefits as coatings for the manufacturing of metallic parts, especially through the reduced time and labor costs of applying them in comparison to other material systems. Automated application of UV-curable coatings would enable significant further cost and time savings. Automation requires a more detailed understanding of the mechanical and interfacial properties of the maskants before and after curing. Through the use of multiple characterization techniques, we investigated structure-process-property relationships of UV-curable polymer resins in relation to their potential as maskants in platinum electroplating. We tested two types of maskants: burn-off maskants that were removed through incineration; and peel-off maskants, which were removed simply by peeling the maskant from the substrate. The burn-off maskants were lower in viscosity and faster to cure as determined, respectively, by rheological flow curves and Fourier transform infrared spectroscopy. The burn-off maskants cured into harder materials that more effectively prevented bleed from the electroplating than the softer, peel-off maskants. The better performance of the burn-off maskants was related to the increased adhesion between the substrate and the maskant, associated with its higher crosslinking density.

This work is being prepared for submission to a journal.

2.1 Introduction

The masking of components with coatings to protect part areas that should not be processed is a vital step in the fabrication and finishing of metallic parts during electroplating^{1,2}. While waxes, tapes, paints, and lacquers are commonly used, ultraviolet (UV)-curable polymers have

great potential as maskant materials, and several commercial polymers are now available for this purpose. The majority of commercial UV-curable resins are based on the free radical curing of acrylates, such as in polyester and epoxy resins, urethanes, silicones, and polyethers; there are also cationic curing systems based on epoxy and vinyl ether, which are not subject to cure inhibition by oxygen³. One of the most notable benefits of UV-curable systems is a reduction in the application time during the masking processes as UV-curable polymers can be spray applied and cure in seconds to minutes upon exposure to UV radiation^{1,4}. In comparison, solvent-based lacquers can require several hours to cure and often require multiple applications to develop suitable coats. Masking with tape must often be redone between steps and is generally unsuitable for liquid processes like electroplating. Thus, production rates with UV-curable masks can easily increase by a factor of four in comparison to traditional masking processes⁵. In addition, organic solvents in traditional lacquers and solvent-based coats pose health and environmental hazards, and may require additional air handling systems to protect workers from volatile organic compounds and generally have more stringent disposal requirements^{5,6}. UV-curable polymers contain no solvents and can generally be disposed of as plastic waste⁵.

Given their versatility, there is an extensive literature on UV-curable polymers. However, few studies focus on the performance of UV-curable maskants during electroplating processes. A great deal of the peer-reviewed literature has examined the use of these materials as photoresists for lithographic patterning of microelectronics. Because UV lithography is optimized to control micro- and nano-scale features upon light exposure,⁷⁻¹⁰ this application does not translate well to the large-scale electroplating of machined parts. Additionally, photoresists are uniformly deposited by spin-coating onto thin, flat wafers, which is very different from the application methods of UV-curable polymers onto complex geometries by painting, dipping, or spraying^{7,11}. Published studies

on UV-curable maskants for electroplating applications typically focus on the polymer chemistry of the curing system, and not the in-situ performance of the mask^{4,12-14}. Industrial literature that evaluates the structure-property-performance relationships of commercial UV-curable masks is sparse, and constrained by limited open knowledge of proprietary mask formulations.

We evaluated the performance of several commercially available, UV-curable polymers as electroplating maskants for gas turbine blades. The maskants were applied to a turbine blade similar to that in Figure 2-1, which is representative of modern single-crystal blades¹⁵, to prevent the plating of platinum. The UV-curable resins were five urethane acrylates. Two are “burn-off” maskants, which cure into hard, brittle coats and are removed from the substrate through incineration. The other three are “peel off” maskants that cure into flexible coatings that can be mechanically removed by peeling from the substrate. The burn-off and peel-off maskants were compared to a traditional solvent-based lacquer that is commonly used as a maskant.



Figure 2-1. An example of a turbine blade. The ridged area on the left is the root. The curved area to the right of the airfoil is the shroud. From *The Engineer*^{Ref 15}.

To determine the suitability of the maskants as barriers to platinum, we characterized the maskants and evaluated their performance on the turbine blades in electroplating baths under typical operating conditions. The analysis of experiments facilitated connections between maskant performance, bulk and interfacial properties, and polymer structure. Scanning electron microscopy

(SEM) was used to visualize the masked regions of the turbine blades subsequent to maskant removal to determine whether (or not) the maskant prevented plating in unwanted areas. The plating performance was correlated to the stiffness, cohesive, and adhesive properties of the cured maskants by hardness measurements and pull-off testing. The bulk and interfacial properties were connected to the polymer structure by inferring it through the rheology of the uncured maskants and Fourier transform infrared (FTIR) spectroscopy. Rheology was used to quantify the shear-dependent viscosity of the uncured maskant, which relates to formulation properties such as the molecular weight; formulations with lower viscosities typically contain pre-polymers of lower molecular weight. These materials have more desirable flow properties for spray application. FTIR was used to evaluate the kinetics and degree of cross-linking during curing; faster kinetics and greater cross-linking typically correspond to formulations with higher amounts of cross-linker, resulting in harder coatings. On this basis, the burn-off maskants had lower high-shear viscosities, cross-linked faster and to a higher degree, and formed harder coats that failed cohesively, i.e., they adhered to the substrate more than themselves. Accordingly, they performed better during electroplating than the peel-off maskants. We provide thorough comparisons of the performance between the burn-off and peel-off maskants in the sections below.

2.2 Methods

2.2.1 Materials

The turbine blades, made of CMSX-4 alloy, were obtained from Chromalloy and Rolls Royce. The commercially available UV-curable maskants and lacquer chosen for study were obtained from industrial sources. The UV-curable maskants studied were all based on urethane acrylates according to publicly available Safety Data Sheets. We organized the maskants into two groups: 1) Burn-off maskants, Tangent 20108 and Dymax 717-R; and 2) Peel-off maskants, Dymax 730-BT, Dymax, 734-BT, and Dymax 726-SC. The burn-off maskants were removed from

the turbine blades after electroplating by incineration at Chromalloy. The peel-off maskants were peeled from the turbine blades by hand in our laboratory at the University of Virginia after electroplating at Chromalloy. The two maskant groups were then compared to the lacquer typically used to mask the turbine blades during the plating process. The lacquer served as a baseline to assess the performance of the burn-off and peel-off maskants. The turbine blades were used as a substrate to assess the degree of successful application, plating barrier performance, and removal of the maskants. Flat plates of Inconel 625 were also used to provide a suitable substrate for hardness and adhesion testing.

2.2.2 Characterization of Uncured Maskants

An Anton Paar MCR 301 stress-controlled rheometer was used for flow curve measurements of the uncured maskants. Measurements were carried out at 20 °C using a 25 cm cone-and-plate geometry to apply a constant shear stress throughout the polymer. A step-down shear test was performed to obtain viscosity flow curves by first shearing each maskant at 2000 1/s for 15 minutes to obtain the equilibrium value of the high shear viscosity, followed by step decreases in shear rate, at which the corresponding equilibrium viscosity was obtained after a 15-minute plateau value.

The cross-linking kinetics and degree of curing of the maskants were evaluated by FTIR. For completely uncured maskant, 1 mL of material was placed in a glass vial which was then filled with 10 mL of trichloroethylene, which is a volatile solvent known to have a high solubility for both uncured and cured acrylate resins. These vials were sonicated until the contents were well-mixed, i.e., the color became consistent throughout the solution. To prepare maskant samples for curing, a small amount of uncured maskant was spread on a glass microscope slide and exposed to UV radiation for 30 seconds, 1 minute, or 3 minutes to cure the resin. Following cure, the maskants were removed from the slide with a razor blade and placed into glass vials which were

then filled with 10 mL trichloroethylene. These vials were sonicated for 16 hours in order to dissolve as much cured maskant as possible. The cross-linking kinetics and degree of crosslinking were determined by comparing the reactive C=C peak to an internal standard C=O peak based on the equation:

$$\% \text{ Conversion} = 100 - 100 \times \frac{(\text{Height}_{\text{C=C}}/\text{Height}_{\text{C=O}})_{\text{cured}}}{(\text{Height}_{\text{C=C}}/\text{Height}_{\text{C=O}})_{\text{uncured}}} \quad (\text{Eq. 2.1})$$

Spectra were taken in the range of 1600 to 1800 cm^{-1} , with the C=C peak appearing in the 1630-1680 cm^{-1} region and the C=O peak appearing in the 1735-1750 cm^{-1} region.

2.3.3 Characterization of Cured Maskants

2.2.3.1 Hardness

Hardness measurements were performed with a Rex Gauge 1600-D, Shore D durometer. The 0.635 cm (specified as 0.25 inches) thick sample needed for testing was prepared by applying thinner layers of maskants 2-3 times to the flat Iconel 625 plates, while curing between each application. The sample was lightly sanded until flat for testing. Two sets of readings, an initial and a settled reading were taken, ensuring that the presser foot of the durometer was firmly on and flush to the flat area of the maskant, which led to the settling of the 30-degree conical indenter of the durometer in the maskant. The initial readings corresponded to the Shore D values given on the various maskant technical data sheets from the manufacturer. Subsequently, the settled reading was taken after 30 seconds, which relates to creep or cold flow in the specimen.

2.2.3.2 Pull-Off Testing

Pull-off tests were performed with a Quantum Digital PATTI (Pneumatic Adhesion Tensile Testing Instrument) to ascertain the adhesive and cohesive behavior of the maskant materials on the flat Iconel 625 plates. An adhesive ring, or “mask”, with an outer diameter of 25.4 mm and an inner diameter of 12.7 mm was placed directly on each plate. A small amount of test maskant was

deposited in the region of plate in the inner diameter of the mask ring and made level, then cured for 1 minute. To investigate the adhesion properties of the lacquer, it was applied by painting it into the region inside the mask ring. Three layers of lacquer were applied, with a 30-minute wait time between coats. The maskants and lacquer were sanded smooth to ensure even contact with the pull-off dolly of the PATTI. Subsequently, an epoxy was applied to the surface of the testing stub, which was then pressed onto the surface of the maskants. The stubs were left undisturbed for 24 hours to let the epoxy cure. Testing was performed by the PATTI gradually increasing pull-off pressure until a material or interface failure occurs. After failure, the failure surfaces of the dolly and substrate were both examined with a Hirox KH-7700 optical microscope to determine which layers failed and the relative areas of these surfaces.

2.2.3.3 Maskant and Lacquer Application

The UV-curable maskants were applied to the turbine blades with a McMaster-Carr air-powered dispenser, chosen to approximate automated application systems. An 18-gauge needle with an inner diameter of 0.84 mm and outer diameter of 1.27 mm was used for application. In addition to the areas typically masked on the blade, straight lines of maskant were also applied on the airfoil of the blade as test regions for platinum bleed studies. Visual inspections were performed to assess application quality and barrier properties. The maskants were cured onto the turbine blades for one minute under a UV lamp. In contrast, the lacquer was applied manually to the turbine blades by painting with a brush. The lacquer was applied in two coats, with 30 minutes to 1 hour passing between each coat, and given 4 hours to dry after the final coat was applied. Visual inspections were performed with a Hirox KH-7700 optical microscope.

2.2.3.4 Post-Plating Inspection

The platinum electroplating of masked turbine blades was performed off-site by Chromalloy. They performed the incineration step for the burn-off maskants, leaving some

untreated, i.e., leaving the burn-off maskant on some turbine blades, for reference in our post-plating observations. The peel-off maskants were removed manually in our laboratory. An FEI Quanta 200 scanning electron microscope was used for elemental mapping by energy-dispersive X-ray spectroscopy (EDS) to investigate platinum bleed and polymer contamination after maskant removal.

2.3 Results

2.3.1 Behavior of Uncured Maskants

All UV-curable maskants displayed shear-thinning behavior, which is typical of polymer solutions, and showed an increasing viscosity at low shear indicative of a gelling material. Figure 2-2 shows the viscosity flow curves of the maskants and Table 2.1 summarizes the important values of yield stress and high-shear viscosity. A low high-shear viscosity is desired for spray application and a relatively high viscosity is desired at low shear to prevent the maskant from flowing to regions that should remain unmasked after application¹⁶.

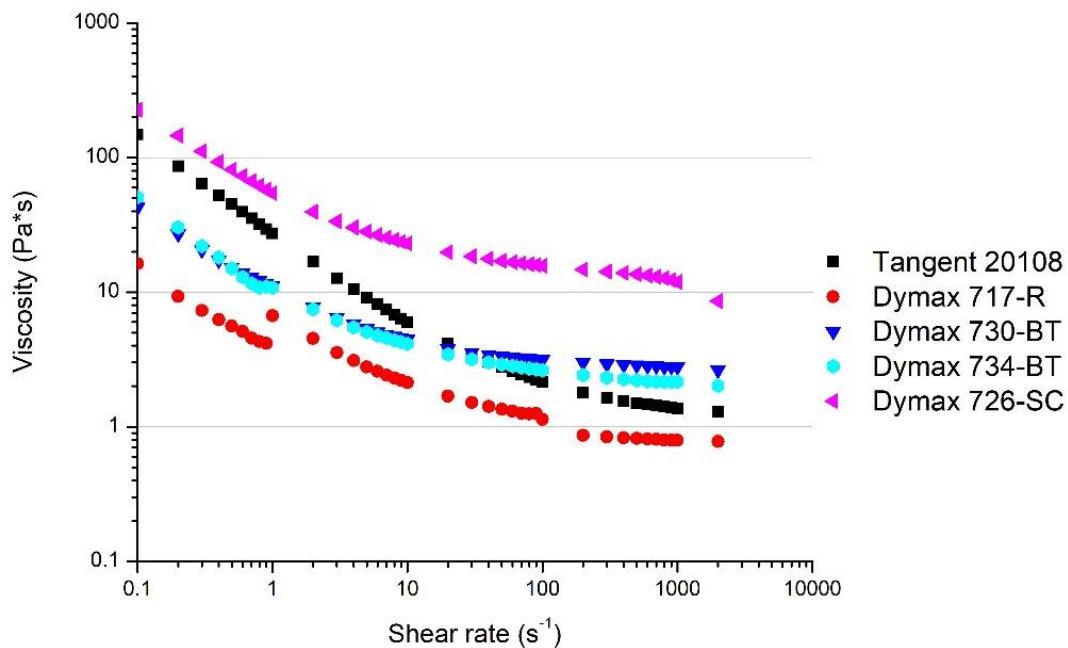


Figure 2-2. Viscosity flow curves of the UV-curable maskants before curing. Burn-off maskants are Tangent 20108 and Dymax 717-R; peel-off maskants are Dymax 730-BT, 734-BT, and 726-SC. Refer to Table 2.1 for the analysis of the viscosity flow curves.

Table 2.1. High-shear viscosity, low-shear yield stress, and Sisko model parameters of uncured maskants

Maskant	Removal Type	High Shear Viscosity - η_{∞} (Pa*s)	Yield Stress - τ_s (Pa)	Consistency - K	Power-law index - n
Tangent 20108	Burn-off	1.4	14.9	25.6	0.24
Dymax 717-R	Burn-off	1.1	1.6	3.4	0.37
Dymax 730-BT	Peel-off	2.8	4.3	7.8	0.29
Dymax 734-BT	Peel-off	2.5	5.1	7.5	0.19
Dymax 726-SC	Peel-off	13.5	22.6	42	0.29

The flow curves in Figure 2-1 can be described by the Sisko model, a power law relationship where the viscosity η as a function of shear rate $\dot{\gamma}$ is described by

$$\eta = \eta_{\infty} + K\dot{\gamma}^{n-1} \quad (\text{Eq. 2.2})$$

where η_{∞} is the viscosity in the high shear limit, K is the consistency, and n is the power-law index¹⁷. The consistency, K , can be related to the energy needed to cause shear deformation within concentrated polymer solutions, the power-law index, n , is related to the ease of disentangling chains¹⁸. As the shear rate approaches zero, viscosity approaches infinity in this model. We are interested in the viscosity at shear rates of 0.1 to 1 s⁻¹, corresponding to deformation at “rest” in storage conditions, and the yield stress representing the start of fluid flow behavior.

Dymax 717-R and the peel-off maskants all have similar power-law indices of $n \approx 0.30$ and K values that increase with the low-shear viscosity of the respective resins. The similar power-law indices presumably reflect a related polymer structure across the maskants (urethane acrylates), and the increasing consistency suggest an increase in molecular weights of the polymers in the resins. The difference in K and n for Tangent 20108 is suggestive of a different formulation approach than that of the Dymax maskants, which may reflect the different manufacturers. Tangent 20108 has the highest yield stress and viscosity at low shear, which should prevent flow or creep of the material between application and curing, while also having one of the lowest viscosities at high shear, which helps in applying the material evenly.

FTIR spectroscopy was used to evaluate the curing times based on an estimated degree of conversion of the carbon-carbon (C=C) double bonds relative to the carbon-oxygen (C=O) bonds in the maskants. Table 2.2 summarizes the results. (The raw spectra can be found in Section A of the appendix.) With the burn-off polymers, Tangent 20108 and Dymax 717-R, and peel-off polymer Dymax 726-SC, the majority of conversion of C=C, and thus, crosslinking is completed within a minute of UV exposure. The analysis of peel-off polymers Dymax 730-BT and 734-BT yielded non-physical results, as the C=C absorption peak increased relative to the C=O peak during UV exposure (see figures A.4 and A.5 in appendix). However, these materials did cure, as the formulations solidified. We suspect that additives in Dymax 730-BT and 734-BT convolute the C=C and C=O peaks.

The flow curves and the FTIR conversions suggest differences in formulation between the burn-off and peel-off maskants. An exact determination of the polymer structures cannot be made without knowing additional proprietary information such as the composition and concentration of additives and the specific polymer chemistry, but we can determine relative trends within the formulations. The higher high-shear viscosities of the peel-off maskants suggest that the peel-off maskants have longer pre-polymers, or precursors, than the burn-off maskants. Longer pre-polymers should result in softer materials. The higher low-shear viscosity and faster crosslinking kinetics of Tangent 20108 over Dymax 717-R suggest the increased presence of additives like particles and high levels of crosslinking agents in Tangent 20108. Thus, cured Tangent 20108 should be harder than Dymax 717-R. Maskant Dymax 726-SC was excluded from further characterization because of problems with adhesion before characterization and plating tests.

Table 2.2 C=C bond conversions after UV exposure for maskants and manufacturer's specifications ('---' denotes non-physical values)

Percent C=C Bond Conversion					Manufacturer Specifications	
Maskant	Removal Type	Cure Time			Time to cure (s)	Thickness (mm)
		30 seconds	1 minute	3 minutes		
Tangent 20108	Burn-off	64.8%	85.6%	89.1%	10	2
Dymax 717-R	Burn-off	10.0%	56.9%	51.4%	30	0.38
Dymax 730-BT	Peel-off	0.13%	---	---	4	0.38
Dymax 734-BT	Peel-off	---	---	---	5	0.38
Dymax 726-SC	Peel-off	86.3%	92.8%	88.3%	8	0.38

2.3.2 Hardness

Shore hardness measures the resistance of a material to indentation and is related to the stiffness/flexibility of the cured coating. In turn, its hardness is related to the density of cross-links between polymer chains in the network. The results of the durometer measurements are shown in the bar graph of Figure 2-3 below. The burn-off maskants were harder than the peel-off maskants and showed significantly less change in hardness after settling. This behavior is indicative of less creep within the cured material, and indicates the burn-off maskants have higher crosslink densities than the peel-off maskants. Based on the rheology and FTIR measurements, the harder coatings stem from formulations containing shorter precursors and higher amounts of crosslinker.

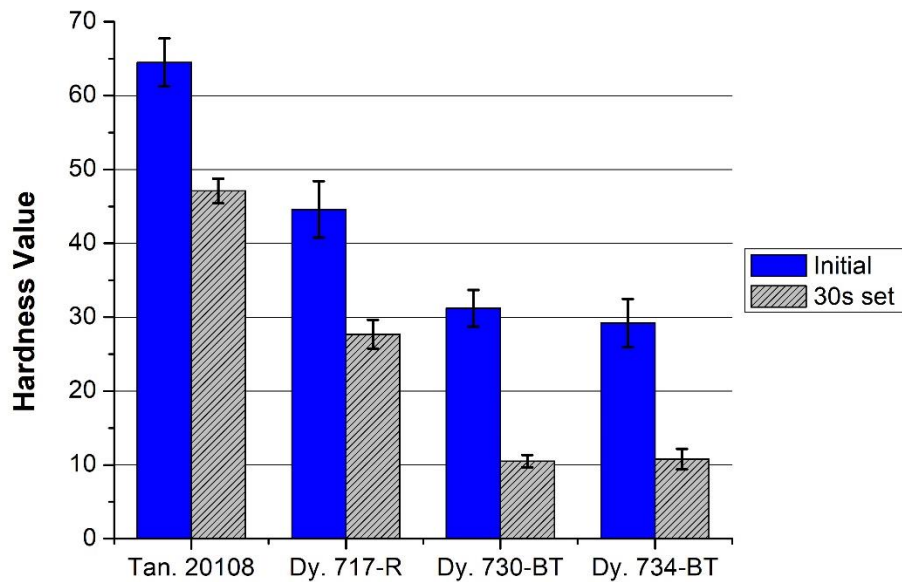


Figure 2-3. Shore hardness values of UV-cured maskants, average of 10 tests for each. Refer to Table 2.1 for mask removal categories.

2.3.3 Adhesion and Cohesion

PATTI testing was performed to quantify the combined adhesion/cohesion strength of the UV-curable maskants for comparison to the lacquer, a traditional maskant for turbine blades. The mechanism of failure, adhesive or cohesive, was confirmed through optical microscopy of the maskant/metal interface. In principle, strong adhesion to the metal is desired to prevent delamination of the maskant from the substrate, which could lead to plating bleed under the maskant. An adhesive/cohesive failure was not observed for Dymax 734-BT; hence, it was omitted from this analysis.

The adhesive/cohesive strength of the remaining UV-curable maskants were equal to or greater than that of the lacquer during pull-off testing, as observed in Figure 2-4. Figure 2-5 shows the representative failure surfaces at the metal/maskant interface; the left and right columns of Figure 2-5 are the tear and metal surfaces, respectively. On this basis, the lacquer and Tangent 20108 failed cohesively, as shown in Figs. 5a-d, leaving residual maskant adhered to the metal as

well as straight edges at the failure surface indicative of embrittlement. In contrast, the burn-off maskant Dymax 717-R in Figs. 5e-f and the peel-off maskant Dymax 730-BT in Figs. 5g-h failed adhesively as both maskants completely delaminated from the metal as evidenced by the complete pull-off of a circular region of polymer coating (Figs. 5e and g), leaving a similar size void on the metal (Figs. 5f and h).

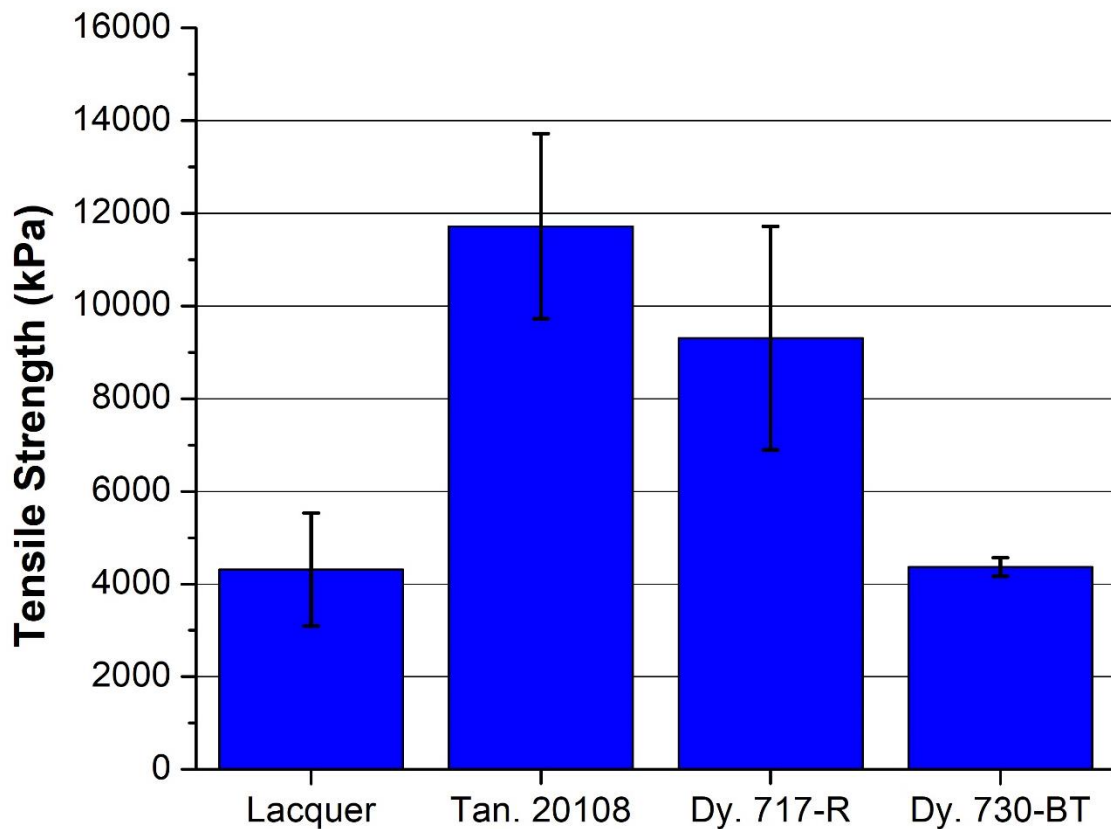


Figure 2-4. Average adhesive/cohesive failure strength of the maskants during PATTI testing. Dymax 734-BT did not fail during testing and is excluded from the figure. Values based on 2-5 tests. Refer to Table 2.1 for mask removal categories.

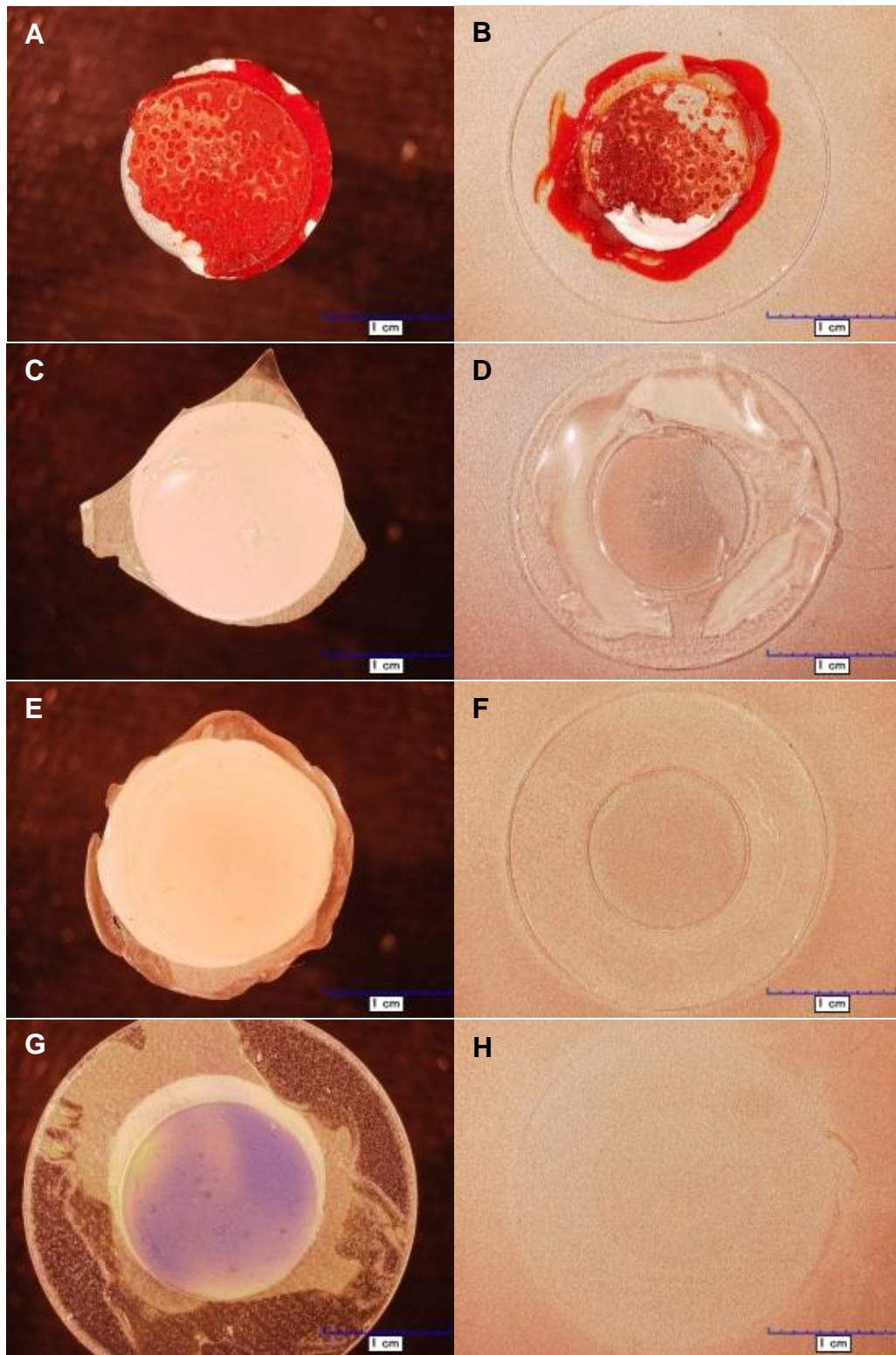


Figure 2-5. Micrographs of the PATTI test surface with maskant (left column) and metal substrate (right column) of maskants after failure during PATTI tests. A) and B) Lacquer; C) and D) Burn-off maskant Tangent 20108; E) and F) Burn-off maskant Dymax 717-R; G) and H) Peel-off maskant Dymax 730-BT

2.3.4 Maskant Application, Platinum Plating, and Post-Plating Inspection

The maskants were applied to the flat airfoil region of the turbine blade to improve the visualization of the maskant/metal interface and the detection of platinum bleed under the maskant. Figure 2-6 shows a representative micrograph of cured maskant on the flat air foil region after platinum plating. The electrodeposition of platinum onto the turbine blades was performed, followed by maskant removal. The two burn-off maskants were incinerated by Chromalloy on-site following deposition. The peel-off maskants were manually removed in our laboratory.



Figure 2-6. Representative image of a cured maskant on a flat, platinum-plated airfoil region.

Subsequently, energy-dispersive X-ray spectroscopy (EDS) was used to make an elemental map of the flat airfoil region where the UV-curable maskant had been removed. A representative image for each maskant is shown in Figure 2-7. The major elements of interest were nickel (Ni), carbon (C), and platinum (Pt), as the turbine blade is a Ni alloy coated with Pt, and higher levels of C can stem from incomplete maskant removal. The burn-off and peel-off maskants performed differently. Pt did not bleed under the previously masked regions of the two burn-off maskants in Figures 2-7a and b. Overplating resulted in the crumpled sheets of platinum in Figure 2-7a and trace Pt from handling these structures is thought to explain the slight Pt signal in the Ni-dominated, masked region. In contrast, Pt bled under the previously masked regions of the peel-off maskants. Thus, the peel-off maskants delaminated, whereas the burn-off maskants did not.

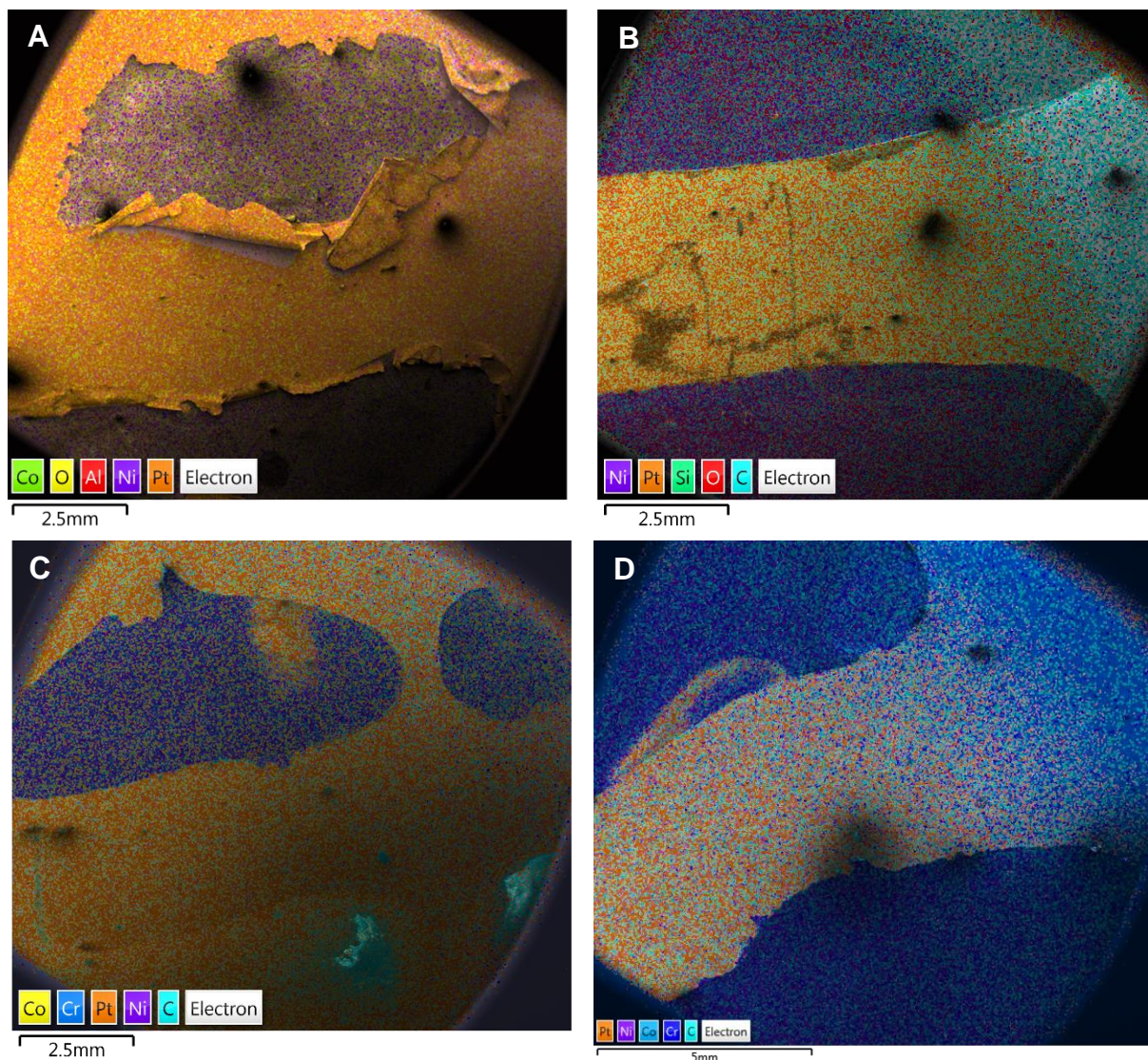


Figure 2-7. EDS map of Pt electroplating around removed maskant regions. In all figures, the legend of elements of interest is as follows: Ni is purple, Pt is orange, C is cyan. Burn-off maskants Tangent 20108 and Dymax 717-R were removed by incineration: A) Burn-off maskant Tangent 20108. Pt overplating resulted in the crumpled structures; B) Burn-off maskant Dymax 717-R. Peel-off maskants Dymax 730-BT and 734-BT removed by peeling: C) Peel-off maskant Dymax 730-BT. Cyan regions are elemental carbon from unremoved maskant; and D) Peel-off maskant Dymax 734-BT. Pt bleed was observed under regions of peel-off maskants. No Pt bleed was observed under burn-off maskants.

2.4 Analysis

The differences in masking performance correlated to the mechanical and interfacial properties of the resins. The burn-off masks had a higher crosslink density, and thus were harder. The burn-off maskants failed cohesively under stress, indicative of strong adhesion to the

substrate; thus, the burn-off maskants were better at preventing platinum bleed under the masked regions. Conversely, the peel-off maskants were softer, and they failed adhesively, which is indicative of better maskant cohesion, but worse substrate adhesion. While these properties permit manual peel-off, they increased the risk for delamination and platinum bleed. Partial delamination likely exposed the masked substrate to the electrolyte plating bath while the blade was submerged.

2.5 Conclusions

We evaluated the structure-property-performance relationships of commercial UV-curable maskants for electroplating operations, characterizing their uncured and cured behavior in addition to evaluating plating bleed. Rheology, FTIR, and Shore hardness measurements indicate that the burn-off maskants likely contain short pre-polymers with higher amounts of crosslinker, resulting in harder coatings upon curing. Adhesion/cohesion measurements and in-situ plating performance tests showed that the burn-off maskants adhered more strongly to the substrate, resulting in coatings that better protected against plating bleed than the softer, peel-off maskants. Thus, burn-off maskants are likely better for masking unprocessed regions during electroplating operations.

2.6 Acknowledgements

Rolls-Royce Corporation and Chromalloy provided financial support of this project through the Commonwealth Center for Advanced Manufacturing (CCAM). Two former Green lab members assisted: Dr. Sara Davis assisted in initial coating selection; Dr. Zachary Farrell assisted in FTIR. Dr. Elizabeth Young-Dohe, then-principal scientist in materials characterization at CCAM, and Philip Grudier, a CCAM intern, assisted in obtaining the hardness values.

2.7 References for Chapter 2

1. Nudelman, A. K. New Options for Masking of Medical Devices — UV Curable Masks. *BONEZone* 47–51 (2004). at <<https://compomat.com/masking-technical-article/>>
2. Altmayer, F. Masking for Surface Finishing. *Prod. Finish.* (2012). at <<https://www.pfonline.com/articles/masking-for-surface-finishing>>

3. Hiemenz, P. C. & Lodge, T. P. *Polymer Chemistry*. CRC Press, Boca Raton, FL (2007)
4. Maag, K., Lenhard, W. & Loeffles, H. New UV curing systems for automotive applications. *Prog. Org. Coatings* **40**, 93–97 (2000).
5. Nudelman, A. UV curable masking resins come of age. *Met. Finish.* **101**, 65–71 (2003).
6. Jusko, J., Baker, G., Hone, C., Naguy, T., Baum, A., Campbell, M. & Straw, R. *Ultraviolet (UV)-Curable Coatings for Aerospace Applications*. (2012) at <<http://www.dtic.mil/docs/citations/ADA627872>>
7. Yonkoski, R. K. & Soane, D. S. Model for spin coating in microelectronic applications. *J. Appl. Phys.* **72**, 725–740 (1992).
8. Decker, C. Light-induced crosslinking polymerization. *Polym. Int.* **51**, 1141–1150 (2002).
9. Choi, S. J., Yoo, P. J., Baek, S. J., Kim, T. W. & Lee, H. H. An ultraviolet-curable mold for Sub-100-nm lithography. *J. Am. Chem. Soc.* **126**, 7744–7745 (2004).
10. Ronse, K. Optical lithography-a historical perspective. *Comptes Rendus Phys.* **7**, 844–857 (2006).
11. Chandra, D. & Crosby, A. J. Self-Wrinkling of UV-Cured Polymer Films. *Adv. Mater.* **23**, 3441–3445 (2011).
12. Fieberg, A. & Reis, O. UV curable electrodeposition systems. *Prog. Org. Coatings* **45**, 239–247 (2002).
13. Bajpai, M., Shukla, V. & Kumar, A. Film performance and UV curing of epoxy acrylate resins. *Prog. Org. Coatings* **44**, 271–278 (2002).
14. Hwang, J. W., Kim, K. N., Lee, G. S., Nam, J. H., Noh, S. M. & Jung, H. W. Rheology and curing characteristics of dual-curable automotive clearcoats using thermal radical initiator derived from O-imino-isourea and photo-initiator. *Prog. Org. Coatings* **76**, 1666–1673 (2013).
15. Nathan, S. Jewel in the crown: Rolls-Royce’s single-crystal turbine blade casting foundry. *Eng.* (2017). at <<https://www.theengineer.co.uk/rolls-royce-single-crystal-turbine-blade/>>
16. Saint-Jaceques, P. Method of Protecting a Surface. (2015).
17. Mezger, T. G. in *Rheol. Handb.* 29–75 Vincentz Network, Hnnover, Germany (2006)
18. Stratton, R. A. The dependence of non-Newtonian viscosity on molecular weight for ‘Monodisperse’ polystyrene. *J. Colloid Interface Sci.* **22**, 517–530 (1966).

Appendix A: Curing, Adhesion, and Pull-Off Experimental Data

A.1 Rates of Cure

A.1.1 Methods

Fourier transform infrared (FTIR) spectroscopy is a characterization method which is used to probe the nature of chemical bonds in a sample by measuring the absorbance or transmittance of infrared light over a range of wavelengths in the far, mid, and near infrared spectrum. Using this technique, it is possible to measure the conversion of polymerizable bonds in a UV-curable resin after specified exposure times by comparison of a reactive bond with a reference (internal standard) peak both before and after UV exposure. In the case of the maskants studied in our trials which are primarily urethane acrylates (as well as other unknown, proprietary mixtures of additives), the polymerizable bond is a carbon-carbon (C=C) double bond which is compared against an internal standard of a carbonyl (carbon-oxygen, C=O) bond making up part of the ester in urethane acrylate monomer.

To prepare resin samples for FTIR characterization, two different approaches were taken depending on whether the material had been cured or not. For uncured maskant, ~1 mL was placed in a glass vial which was then filled with ~10 mL of trichloroethylene, which is a volatile solvent known to have a high solubility for both uncured and cured methyl methacrylate resins. These vials were sonicated until the color became consistent throughout the solution. To prepare cured maskant samples, a small amount of uncured maskant was spread on a glass microscope slide and exposed to UV radiation for 30 seconds, 1 minute, or 3 minutes to cure the resin. Following cure, maskants were removed from the slide with a razor blade and placed into glass vials which were

then filled with ~10 mL trichloroethylene. These vials were sonicated for ~16 hours in order to dissolve as much cured maskant as possible.

To begin the process of infrared spectrum collection, two potassium bromide plates (transparent to infrared light) were cleaned with dichloromethane to remove any residual organics, dried, and placed into the infrared spectrometer. Using this configuration, a background spectrum was collected. Subsequently, the potassium bromide plates are removed from the spectrometer and a small amount (~ 5 drops) of maskant solution in trichloroethylene was withdrawn from the vial and placed onto one plate. The sample was passed over with a gentle stream of air to speed drying and sandwiched underneath a second potassium bromide plate. The sample was inserted into the spectrometer and a second infrared spectrum collected. The spectra collected in this way were then exported for further analysis.

A.1.2 Results and Analyses

In order to analyze the collected spectra to determine the degree of C=C conversion, a reactive C=C peak and an internal standard C=O peak were selected from the mid-infrared range based on literature sources. The C=C peak typically appears in the 1630-1680 cm^{-1} range while the C=O ester peak appears between 1735-1750 cm^{-1} with some variation possible due to bond conjugation. Via the formula in Eq. A.1

$$\% \text{ Conversion} = 100 - 100 \times \frac{(\text{Height}_{\text{C=C}}/\text{Height}_{\text{C=O}})_{\text{cured}}}{(\text{Height}_{\text{C=C}}/\text{Height}_{\text{C=O}})_{\text{uncured}}} \quad \text{Eq. A.1}$$

the degree of C=C bond conversion via polymerization is easily calculated from the peak heights of the C=C and C=O peaks before and after curing. The spectra from 1600-1800 cm^{-1} for each of the five resins tested appear below.

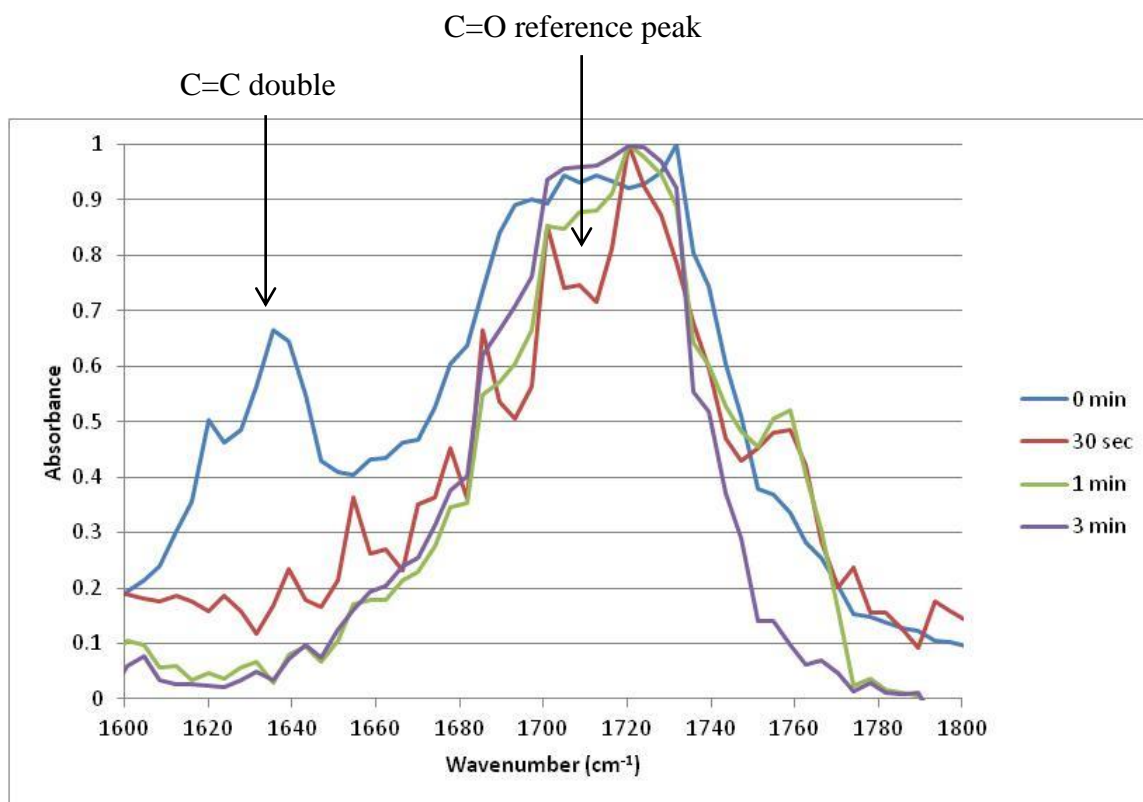


Figure A.1. Infrared absorption spectra for Tangent 20108 resin. The large peak present at ~ 1640 cm^{-1} in the $t=0$ spectrum disappears as the exposure time increases, indicating conversion of the C=C bonds and therefore polymerization of the resin. The crosslinking reaction is complete after one minute.

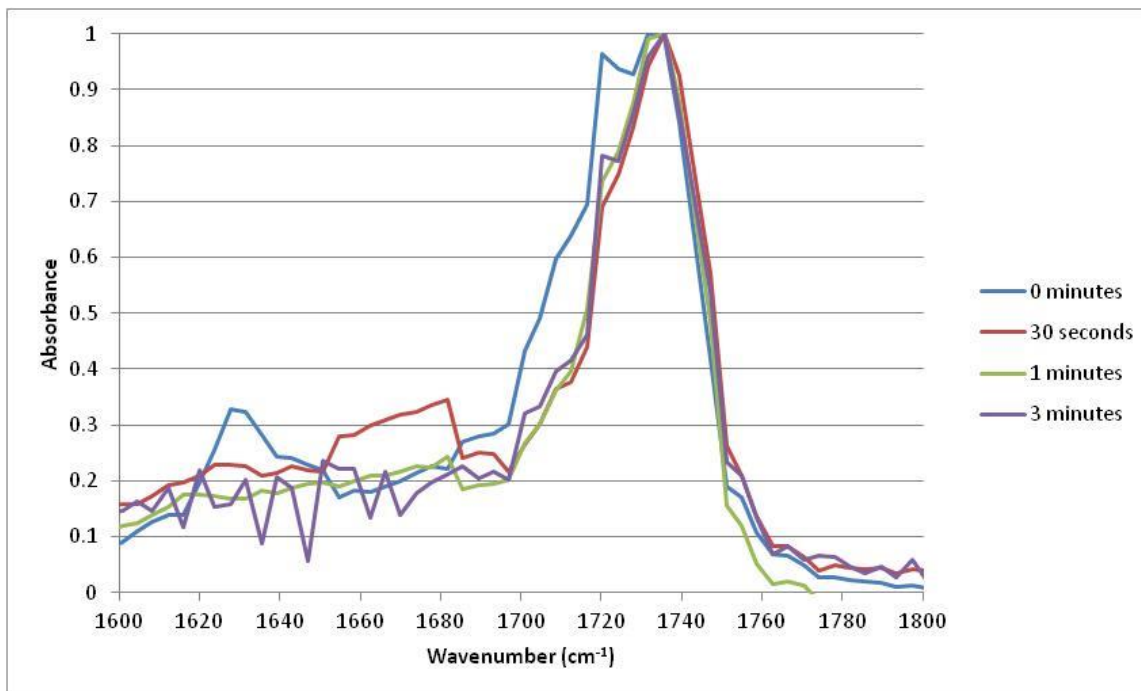


Figure A.2. Infrared absorption spectra for Dymax 717-R resin. The small peak present at ~1630 cm⁻¹ in the $t=0$ spectrum drops as the exposure time increases, indicating conversion of the C=C bonds and polymerization of the resin. The crosslinking reaction reaches completion around 60 s.

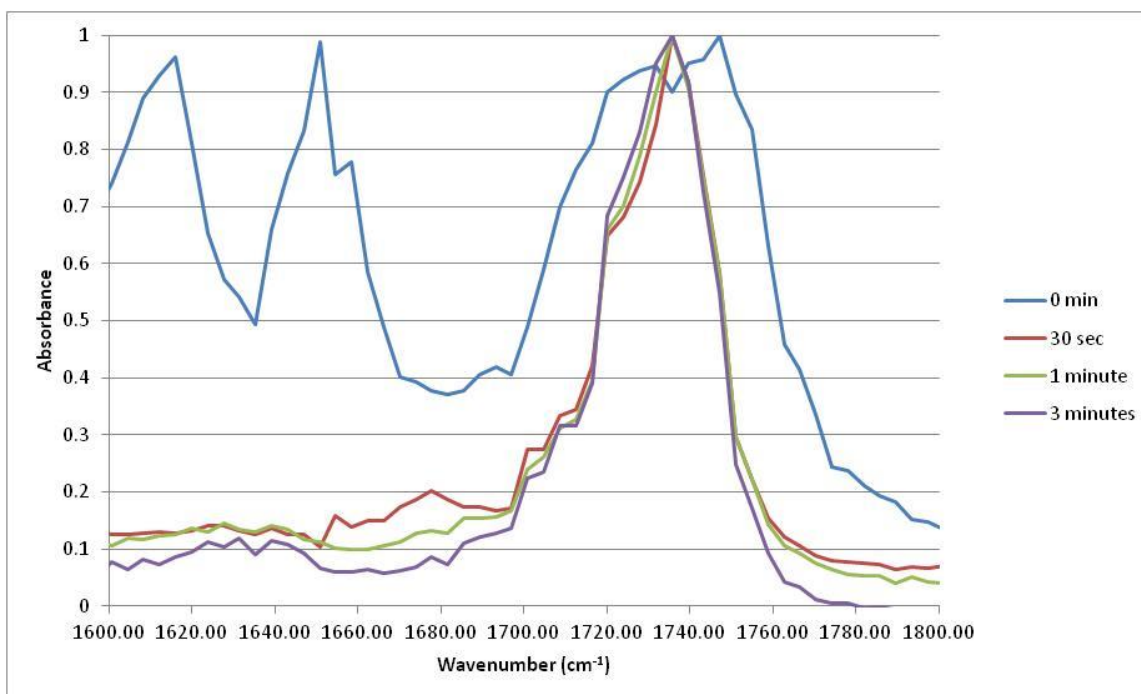


Figure A.3. Infrared absorption spectra for Dymax 726-SC resin. The large peak present at ~1650 cm⁻¹ in the $t=0$ spectrum disappears as the exposure time increases, indicating conversion of the C=C bonds and polymerization of the resin. The crosslinking reaction reaches completion around 30-60 s.

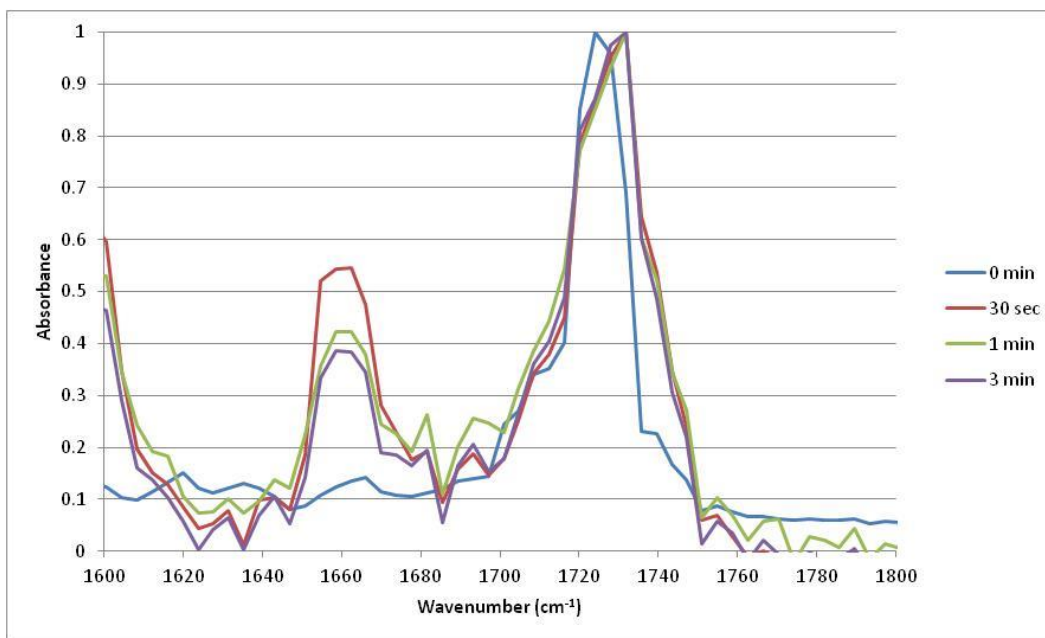


Figure A.4. Infrared spectra for Dymax 730-BT resin. A peak appears at $\sim 1660\text{ cm}^{-1}$ which is within the expected range for C=C bonds. This behavior is strange as bond disappearance is expected rather than formation. Hence, either the C=O reference or C=C peaks are convoluted with an unknown additive.

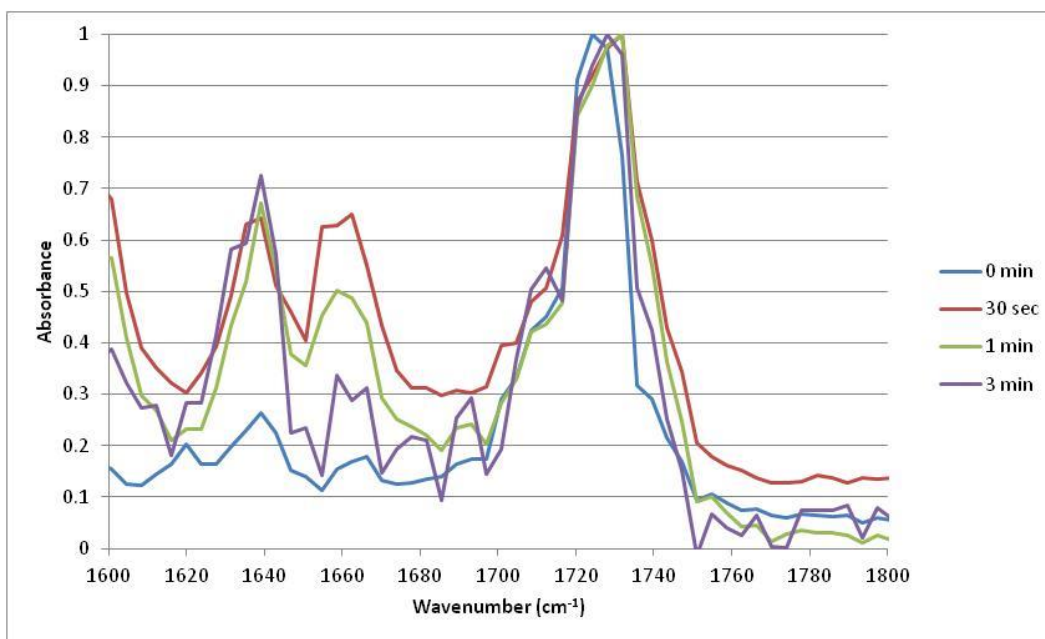


Figure A.5. Infrared spectra for Dymax 734-BT resin. Peaks appear at $\sim 1640\text{ cm}^{-1}$ and $\sim 1660\text{ cm}^{-1}$, which are within the range for C=C bonds. This behavior is strange as bond disappearance is expected rather than formation. Hence, the C=O reference or C=C peaks are convoluted with an unknown additive.

From examination of the above plots, some conclusions may immediately be noted. In Tangent 20108, Dymax 717-R, and Dymax 726-SC maskants in Figures A.1 – A.3, the C=C and C=O peaks appear and behave as expected, with the reactive C=C peak dropping relative to the reference C=O peak from an initial maximum at $t=0$ minutes to a minimum at $t=3$ minutes. This indicates polymerization proceeding as expected for these materials. In each of these resins, the majority of polymerization is completed after only one minute of UV exposure.

For Dymax 730-BT and 734-BT in Figures A.4 and A.5, respectively, the C=C peak increases relative to the C=O peak after UV exposure. This absorption behavior is unexpected as both a color change from the uncured to cured material and progression from a gel to a solid indicates that polymerization is occurring. As we do not know the proprietary additives in these resins, we hypothesize that an additive is convoluting the infrared signal of either the C=O reference peak (rendering it reactive, and therefore not useable as a reference) or the C=C peak. It is not possible to draw further conclusions on this topic without additional experimental characterization via methods such as GC-MS and/or Raman spectroscopy.

From the data illustrated in the spectra above in conjunction with the Equation A.1 for C=C bond conversion, the conversions for each resin at $t=0$ minutes, 30 seconds, 1 minute, and 3 minutes were calculated. These conversions are shown in the table below.

Table A-1. C=C bond conversions after UV exposure for maskants and manufacturer's specifications

Experimental Results				Manufacturer Specifications	
	30 seconds	1 minute	3 minutes	Time to cure (s)	Thickness (mm)
Tangent 20108	Burn-off	64.8%	85.6%	89.1%	10
Dymax 717-R	Burn-off	10.0%	56.9%	51.4%	30
Dymax 730-BT*	Peel-off	0.13%	---	---	4
Dymax 734-BT*	Peel-off	---	---	---	5
Dymax 726-SC	Peel-off	86.3%	92.8%	88.3%	8

*Unphysical result

As mentioned previously, the burn-off maskants as well as the peel-off maskant Dymax 726-SC exhibit expected curing behavior, where the majority of curing is complete after 1 minute, as evidenced by the disappearance of the C=C bond infrared peak. More specifically, the Tangent 20108 maskant reaches a stable C=O conversion value around this time, which is slower than manufacturer specifications, while the crosslinking reaction of maskant Dymax 717-R reaches completion around 30 seconds in line with manufacturer's specifications. The degree of conversion, and hence, the degree of crosslinking of Dymax 717-R is less than Tangent 20108, which reflects why the Tangent 20108 is harder.

The crosslinking reaction of the peel-off maskant Dymax 726-SC, is completed by 30 seconds; however, the Dymax 730-BT and 734-BT maskants in Table A-1 show negative conversions, which are not physically realizable; presumably, some additive present is convoluting with one of the peaks of interest. Thus, further experimentation is necessary to quantify curing of Dymax 730-BT and 734-BT.

A.2 Adhesion

The burst pressures are failures are listed in Table A-2. Full analysis of the PATTI tests involves looking at failure within all the layers and interfaces of the substrate-maskant-dolly

system and is in Table A-3 below for samples that actually failed below the maximum burst pressure of 120 PSI.

Table A-2. Burst pressure and tensile strengths from PATTI testing.

Sample	Material	Raw burst pressure (PSI)	Pull-off tensile strength (PSI)
1	Lacquer	37.7	750
2	Lacquer	24.6	500
3	Tangent 20108	108.9	2200
4	Tangent 20108	76.5	1550
5	Tangent 20108	75.8	1500
6	Tangent 20108	76.7	1550
7	Tangent 20108	86.3	1700
8	Dymax 717-R	86.1	1700
9	Dymax 717-R	67	1350
10	Dymax 717-R	50.4	1000
11	Dymax 730-BT	32.3	650
12	Dymax 730-BT	32	650
13	Dymax 730-BT	31.2	600
14	Dymax 730-BT	120	2400
15	Dymax 730-BT	120	2400
16	Dymax 734-BT	120	2400
17	Dymax 734-BT	120	2400
18	Dymax 734-BT	120	2400
19	Dymax 734-BT	120	2400
20	Dymax 734-BT	120	2400

Table A-3. Analysis of PATTI material failures

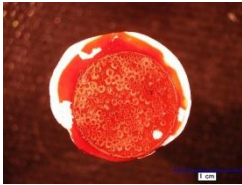
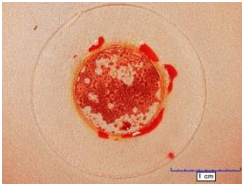
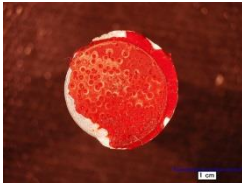
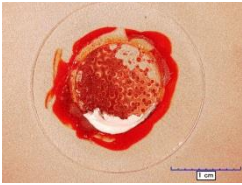
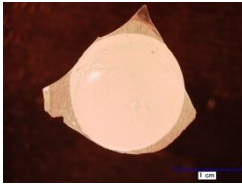
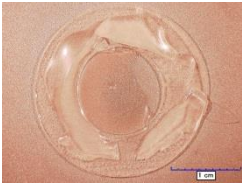
Test Sample Data		Dolly Side	Substrate Side	Failure Breakdown (%)		Analysis									
<table border="1"> <tr><td>Sample No.</td><td>1</td></tr> <tr><td>Maskant</td><td>Lacquer</td></tr> <tr><td>Thickness</td><td>.015"</td></tr> <tr><td>Burst fail (psi)</td><td>38</td></tr> <tr><td>Coating fail (psi)</td><td>750</td></tr> </table>	Sample No.	1	Maskant	Lacquer	Thickness	.015"	Burst fail (psi)	38	Coating fail (psi)	750			0	Dolly Body	Failure at substrate/maskant interface. Maskant is patchy.
	Sample No.	1													
	Maskant	Lacquer													
	Thickness	.015"													
	Burst fail (psi)	38													
	Coating fail (psi)	750													
0	Dolly/Adhesive Interface														
0	Adhesive (Cohesive)														
0	Adhesive/Maskant Interface														
70	Maskant (Cohesive)														
30	Substrate/Maskant Interface														
0	Substrate														
<table border="1"> <tr><td>Sample No.</td><td>2</td></tr> <tr><td>Maskant</td><td>Lacquer</td></tr> <tr><td>Thickness</td><td>.01"</td></tr> <tr><td>Burst fail (psi)</td><td>25</td></tr> <tr><td>Coating fail (psi)</td><td>500</td></tr> </table>	Sample No.	2	Maskant	Lacquer	Thickness	.01"	Burst fail (psi)	25	Coating fail (psi)	500			0	Dolly Body	Failure mostly at substrate/maskant interface, but some epoxy still remains on maskant on substrate.
	Sample No.	2													
	Maskant	Lacquer													
	Thickness	.01"													
	Burst fail (psi)	25													
	Coating fail (psi)	500													
0	Dolly/Adhesive Interface														
10	Adhesive (Cohesive)														
0	Adhesive/Maskant Interface														
70	Maskant (Cohesive)														
20	Substrate/Maskant Interface														
0	Substrate														
<table border="1"> <tr><td>Sample No.</td><td>3</td></tr> <tr><td>Maskant</td><td>Tangent 20108</td></tr> <tr><td>Thickness</td><td>.05"</td></tr> <tr><td>Burst fail (psi)</td><td>109</td></tr> <tr><td>Coating fail (psi)</td><td>2200</td></tr> </table>	Sample No.	3	Maskant	Tangent 20108	Thickness	.05"	Burst fail (psi)	109	Coating fail (psi)	2200			0	Dolly Body	20% failure at maskant-metal interface. Failure plane is at low angle (~30 deg) across cured polymer. Fracture is brittle. Slight cracks at edge.
	Sample No.	3													
	Maskant	Tangent 20108													
	Thickness	.05"													
	Burst fail (psi)	109													
	Coating fail (psi)	2200													
0	Dolly/Adhesive Interface														
0	Adhesive (Cohesive)														
0	Adhesive/Maskant Interface														
80	Maskant (Cohesive)														
20	Substrate/Maskant Interface														
0	Substrate														

Table A-3. Analysis of PATTI material failures

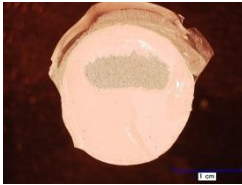

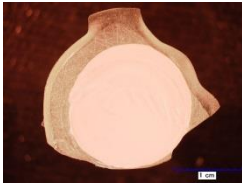
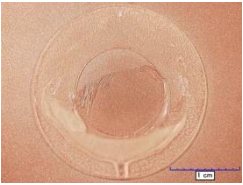
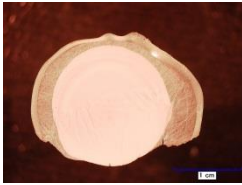
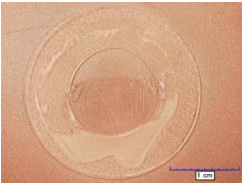
Test Sample Data		Dolly Side	Substrate Side	Failure Breakdown (%)		Analysis
Sample No.	4			0	Dolly Body	No cracks in failure surface. Failure is not along single plane.
Maskant	Tangent 20108			40	Dolly/Adhesive Interface	
Thickness	.05"			0	Adhesive (Cohesive)	
Burst fail (psi)	77			20	Adhesive/Maskant Interface	
Coating fail (psi)	1550			40	Maskant (Cohesive)	
				0	Substrate/Maskant Interface	
			0	Substrate		
Sample No.	5			0	Dolly Body	20% failure at maskant-metal interface. Failure plane is at low angle (~30 deg) across cured polymer. Fracture is brittle. Slight cracks along failure surface.
Maskant	Tangent 20108			0	Dolly/Adhesive Interface	
Thickness	.05"			0	Adhesive (Cohesive)	
Burst fail (psi)	76			0	Adhesive/Maskant Interface	
Coating fail (psi)	1500			80	Maskant (Cohesive)	
				20	Substrate/Maskant Interface	
			0	Substrate		
Sample No.	6			0	Dolly Body	30% failure at maskant-metal interface. Failure plane is at low angle (~30 deg) across cured polymer. Fracture is brittle. Cracks along failure surface.
Maskant	Tangent 20108			0	Dolly/Adhesive Interface	
Thickness	.04"			0	Adhesive (Cohesive)	
Burst fail (psi)	77			0	Adhesive/Maskant Interface	
Coating fail (psi)	1550			75	Maskant (Cohesive)	
				25	Substrate/Maskant Interface	
			0	Substrate		

Table A-3. Analysis of PATTI material failures

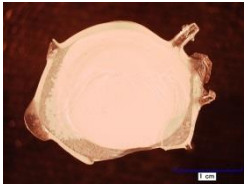

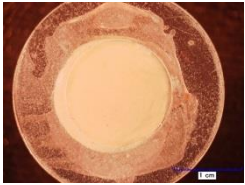
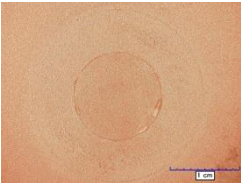
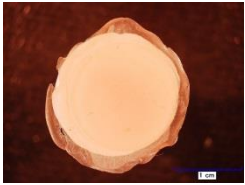
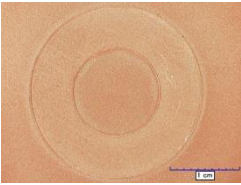
Test Sample Data		Dolly Side	Substrate Side	Failure Breakdown (%)		Analysis
Sample No.	7			0	Dolly Body	20% failure at maskant-metal interface. Failure plane is at low angle (~30 deg) across cured polymer. Fracture is brittle. Slight cracks along failure surface.
Maskant	Tangent 20108			0	Dolly/Adhesive Interface	
Thickness	.06"			0	Adhesive (Cohesive)	
Burst fail (psi)	86			0	Adhesive/Maskant Interface	
Coating fail (psi)	1700			80	Maskant (Cohesive)	
				20	Substrate/Maskant Interface	
		0	Substrate			
Sample No.	8			0	Dolly Body	Smooth pull-off from substrate surface.
Maskant	Dymax 717-R			0	Dolly/Adhesive Interface	
Thickness	.03"			0	Adhesive (Cohesive)	
Burst fail (psi)	86			0	Adhesive/Maskant Interface	
Coating fail (psi)	1700			0	Maskant (Cohesive)	
				100	Substrate/Maskant Interface	
		0	Substrate			
Sample No.	9			0	Dolly Body	Smooth pull-off from substrate surface.
Maskant	Dymax 717-R			0	Dolly/Adhesive Interface	
Thickness	.03"			0	Adhesive (Cohesive)	
Burst fail (psi)	67			0	Adhesive/Maskant Interface	
Coating fail (psi)	1350			0	Maskant (Cohesive)	
				100	Substrate/Maskant Interface	
		0	Substrate			

Table A-3. Analysis of PATTI material failures

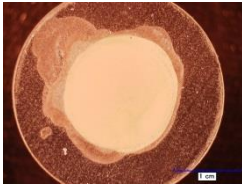
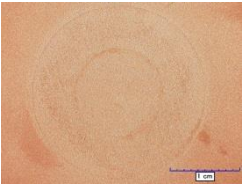
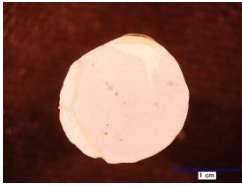
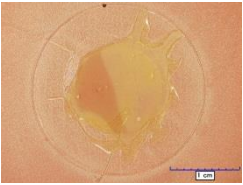
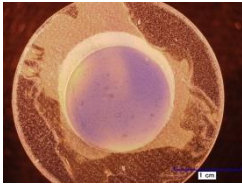
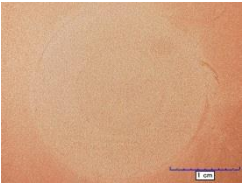
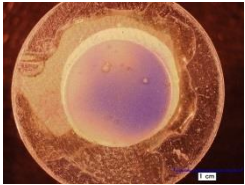
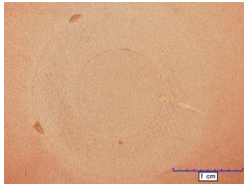
Test Sample Data		Dolly Side	Substrate Side	Failure Breakdown (%)		Analysis
Sample No.	10			0	Dolly Body	Smooth pull-off from substrate surface.
Maskant	Dymax 717-R			0	Dolly/Adhesive Interface	
Thickness	.03"			0	Adhesive (Cohesive)	
Burst fail (psi)	50			0	Adhesive/Maskant Interface	
Coating fail (psi)	1000			0	Maskant (Cohesive)	
				100	Substrate/Maskant Interface	
				0	Substrate	
Sample No.	11			0	Dolly Body	Complete, smooth pull-off at epoxy-maskant interface
Maskant	Dymax 730-BT			0	Dolly/Adhesive Interface	
Thickness	.03"			0	Adhesive (Cohesive)	
Burst fail (psi)	32			100	Adhesive/Maskant Interface	
Coating fail (psi)	650			0	Maskant (Cohesive)	
				0	Substrate/Maskant Interface	
				0	Substrate	
Sample No.	12			0	Dolly Body	Complete, smooth pull-off from substrate.
Maskant	Dymax 730-BT			0	Dolly/Adhesive Interface	
Thickness	.025"			0	Adhesive (Cohesive)	
Burst fail (psi)	32			0	Adhesive/Maskant Interface	
Coating fail (psi)	650			0	Maskant (Cohesive)	
				100	Substrate/Maskant Interface	
				0	Substrate	

Table A-3. Analysis of PATTI material failures

Test Sample Data		Dolly Side	Substrate Side	Failure Breakdown (%)		Analysis
Sample No.	13			0	Dolly Body	Complete, smooth pull-off from substrate.
Maskant	Dymax 730-BT			0	Dolly/Adhesive Interface	
Thickness	.025"			0	Adhesive (Cohesive)	
Burst fail (psi)	31			0	Adhesive/Maskant Interface	
Coating fail (psi)	600			0	Maskant (Cohesive)	
				100	Substrate/Maskant Interface	
				0	Substrate	

3. Graphene, Its Colloids, and Their Applications

Abstract

There has been an explosion of interest in two-dimensional nanomaterials, in particular, the carbon allotrope graphene, because of their many outstanding properties. A major limit in the practical use of graphene, and 2-D nanomaterials generally, is the synthesis of large amounts with the desired properties, such as electronic conductivity or nanoparticle size. Size is particularly important for determining the properties that result from incorporating these nanomaterials as fillers in novel polymer nanocomposites. Liquid-phase exfoliation by shear is attractive because it is scalable and potentially size-selective. Shear exfoliation also produces significantly fewer defects than prior methods based on ultrasonication.

Prior work on liquid-phase exfoliated graphene focuses on optimizing exfoliation by choosing solvents that have surface energies close to that of graphite/graphene. However, this framework is unable to explain differences in graphene yield and quality produced by solvents with similar surface energies and cannot predict the long-term dispersion stability of the exfoliated material. Fluid mechanics predicts that higher viscosity liquids should increase the shear forces transmitted to the graphite flakes, which could improve yield. Colloid science shows that long-range attractive forces between particles are more effectively cancelled by matching the polarizability of the particles and the solvent, which corresponds to dispersing the particles in a solution with a matching refractive index or dielectric constant.

Studying how these properties affect exfoliation and dispersion stability will enable better understanding of the mechanisms encountered in large-scale manufacturing. This will enable better selection of solvents to exfoliate 2D materials for a given application, or to perhaps even

design new solvents, such as room-temperature ionic liquids, to optimize a specific exfoliation. Graphene dispersions have a great deal of potential as functional fluids, a solution for printed materials (both 2-D and 3-D), and as a precursor for polymer nanocomposites. All these applications require dispersions to be stable over long timescales.

3.1 Graphene

In the most technical sense, the term “graphene” refers to an isolated atomic monolayer of sp^2 -hybridized carbon. In literature, graphene is often used more loosely to refer to any material with a small number of layers of sp^2 -carbon, though it is more precise to refer to bilayer, trilayer, or few-layer graphene as appropriate¹. At 10 or more layers, graphene’s electronic properties start to closely resemble graphite, and precision suggests that “graphene” should no longer be used to refer to such structures^{1,2}.

It is also important to distinguish graphene from the closely related graphene oxide. Graphene oxide (GO) is formed from the exfoliation of graphite oxide. Graphite oxides have layer spacings that are about twice as large as those of pure graphite, allowing for easier isolation of graphene oxide compared to pristine graphene. Due to the oxidation, graphene oxide has many functional groups on its surface, including epoxy, hydroxyl, and carbonyl groups³. These groups disrupt the sp^2 -bonded carbon network, reducing electronic and thermal conductivity in the plane. However, graphene’s impressive mechanical properties may still be retained. Graphene oxide is

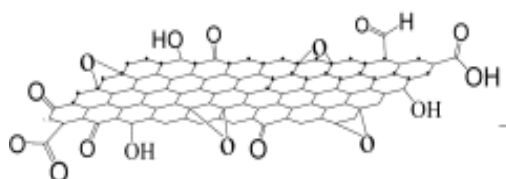


Figure 3-1. Graphene oxide exfoliated from graphite oxide, showing hydroxyl, carboxyl, and epoxy groups. From Fang et al., 2009^{Ref 3}

often used as a starting material for the production of graphene-based derivatives as these functional groups are useful for further chemical reactions. It is also possible to reduce graphene oxide, either thermally or chemically. This material is often specified as reduced graphene oxide (RGO) instead of just graphene, because while it is more conductive than the oxide, it still contains relatively large amounts of oxygen in comparison to pristine graphene and does not fully recover its high conductivity⁴⁻⁶. Density functional theory models also suggest that complete reduction is impossible⁴. A high-resolution transmission electron microscopy study shows RGO has an extensive number of topological defects, both as isolated heptagon-pentagon pairs and extended regions with amorphous structure, which would not be detected by spectroscopy⁷. When I want to refer to a “broad” sense of graphene including these derivatives, I will use the term “graphene-related material” (GRM).

3.1.1 Potential Applications of Graphene

Graphene has caught the attention of scientists and engineers across fields because of its many impressive properties, especially its high mechanical strength, with a Young’s modulus of over a terapascal, and electronic properties^{8,9}. Academia and industry are both interested in deploying graphene in a wide array of applications^{10,11}. Because of graphene’s high charge carrier mobility, even at high carrier concentrations, there is great interest in using it for electronics, but current attempts for computing applications are limited by the absence of a bandgap in pristine graphene⁸. The inherent high surface area and specific volume of a two-dimensional material make graphene effective at the absorption of species for removal, or combined with the sensitivity of graphene’s electronic properties to adsorbed molecules, make it a promising sensor^{12,13}. As a sensor, graphene has a comparative advantage to closely related carbon nanotubes because nanotubes are contaminated with metals from their synthesis¹². Graphene can also be used as a selective filter or impermeable barrier for liquids and/or gases depending on how it is processed,

with applications ranging from water desalination to food packaging^{12,14,15}. There is also interest in modified graphene or graphene-based composites to break down pollutants^{12,16}.

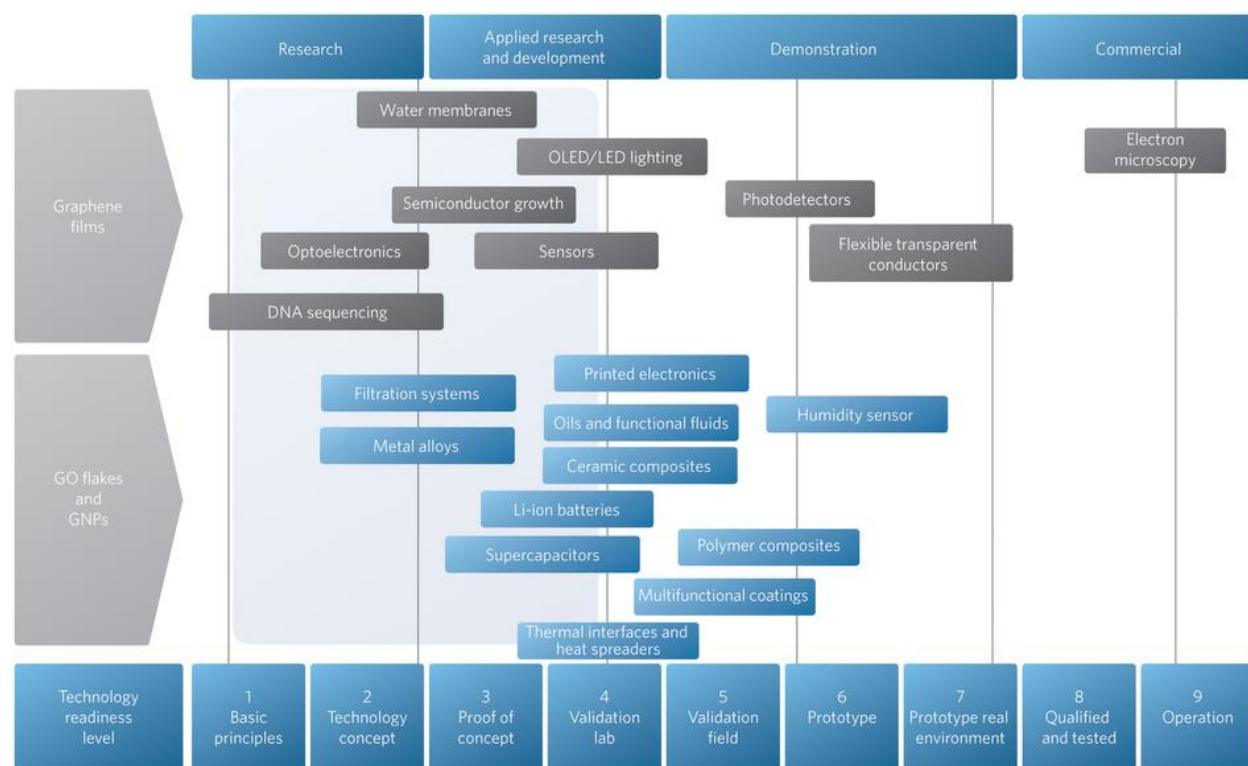


Figure 3-2. An evaluation of the state of various potential applications of graphene and related materials. From Zurutuza and Marinelli., 2014^{Ref 10}.

3.1.2 Graphene Production

Graphene can be produced in many different ways, with both bottom-up and top-down techniques being cost-effective, which also makes graphene distinct among contemporary nanomaterials¹⁷. Fabrication methods are generally chosen with desired properties/applications in mind. High-tech (opto-)electronic applications such as computing require relatively large areas of very high-quality, pristine graphene, which can currently only be produced by bottom-up chemical techniques like chemical vapor deposition¹⁸. Although micromechanical cleavage was used by Novoselov et al. in their original paper characterizing graphene, and still often used to make graphene for concept devices, it is impractical for industrial scale-up^{17,19}.

Similar to micromechanical cleavage, liquid-phase exfoliation uses mechanical forces to separate graphite or graphite oxide into layers of graphene/GO. (Graphite oxide can also be exfoliated by heating to temperatures around 550 K²⁰.) Like in cleavage, the size of the resulting material is limited by the size of the starting graphitic material, but exfoliation can produce greater amounts of material. Early work focused on graphite oxide because the greater spacing between layers makes it easier to exfoliate²¹. In 2008, Hernandez et al. from Jonathan Coleman's group showed that it is possible to directly exfoliate few-layer graphene flakes on the order of hundreds of nm from graphite in organic solutions²².

Much work on liquid-phase exfoliation has focused on sonication, where the shock waves from collapsing cavitation bubbles provide the mechanical force, as seen in Figure 3- 3²³. A recent review even complained that the graphene exfoliation and dispersion literature relies too much on sonication research, while high shear or agitation methods will probably become the foundation for large-scale manufacturing⁵. One major issue is that sonication is hard to scale up^{5,24}. The energy of a sonicator is primarily dissipated near the agitator, so unless the agitator or bulk fluid moves, material further away will never experience strong forces²³. The production rate in sonication is proportional to the energy density of the system and almost completely independent of volume²⁵. Additionally, it has been discovered that graphene produced through sonication has significantly more defects than initially expected, which is attributed to the extreme conditions that take place during cavitation, such as high local temperatures and pressures, which can even lead to localized chemical modification of the graphene^{23,26}.

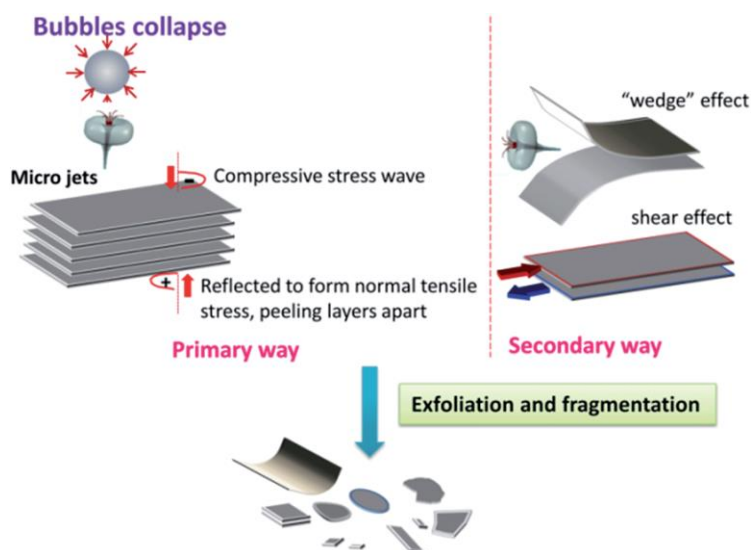


Figure 3-3. In sonication, the layers are primarily exfoliated by the shock waves from cavitation. From Yi and Shen, 2015^{Ref 23}

The disadvantages of sonication-assisted exfoliation have led to an interest in processes that would primarily shear graphene layers off of each other instead. 10-20 times less energy is required to separate graphite layers by sliding than by changing the interlayer distance²⁴. In 2014, Paton et al., again from Coleman's group, showed that it is possible to directly produce few-layer graphene flakes from graphite by applying a high rate of shear to both organic and aqueous solutions containing graphite²⁷. These flakes were relatively large, ranging from 300 to 800 nm. They also showed that the graphene produced does not have significantly more defects than the graphite precursor, with the exception of edge defects attributable to the smaller size of the graphene flakes relative to the initial graphite grains. This method is scalable to larger set-ups, which is promising for manufacturing applications. Using the same set-up, they were able to exfoliate flakes of BN, WS₂, MoSe₂, and MoTe₂, showing that the technique is applicable to layered solids generally²⁷. Most interestingly, while the initial work used a high-shear rotor/stator mixer, Coleman's group and Yi and Shen have found that turbulent flow in conventional blenders (even consumer kitchen blenders) can provide the requisite shear for graphene exfoliation^{25,27,28}. In addition to shear forces, Yi and Shen suggest that collisions between

graphite flakes and localized pressure differences in the turbulent flow regime may also contribute to graphene exfoliation²⁸.

3.2 Graphene Colloids

In a discussion of graphene colloids and dispersions, it is worth bringing up another terminological point. It has been noted by Giordani et al. and Cheng et al. that the carbon nanotube literature often causally uses the word “solution” to refer to a system without knowing the thermodynamic stability of nanotube solvation in that system, and so “solution” is often used to describe what are actually sols, a colloidal dispersion of solids in liquid^{29,30}. Similar ambiguity exists in the graphene dispersion/solution literature due to overlap in research on both materials. Generally, I will try to stick to the terms “dispersion”, “colloidal solution”, or “sol” as appropriate. However, the liquids used will often still be described as “solvents” due to the typical reference of commonly used liquid organic chemicals as such instead of the more technical “dispersant”. Also, one must deal with the above-mentioned ambiguity of graphene-related materials, as graphene oxide is more easily dispersed than reduced graphene oxide, which is more easily dispersed than pristine graphene^{5,31}.

The mechanisms of graphene dispersion are illustrated in Figure 3-4, which involve the following processes: (1) immersion – wetting of the bulk layered material by the solvent, (2) insertion – penetration of the solvent molecules between interior layers, (3) exfoliation – breaking up of the material into layers, and (4) stabilization – the prevention of aggregation of the layers in the solvent³².

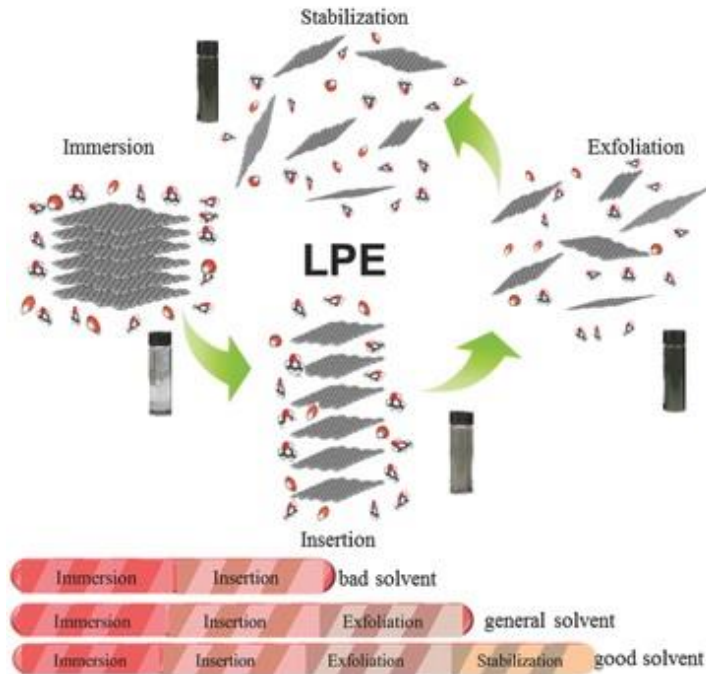


Figure 3-4. The four processes involved in liquid-phase exfoliation (LPE) of a layered solid. From Shen et al., 2016^{Ref 32}

The use of surface energies represents a macroscopic, thermodynamic approach for calculating the total (free) mixing energy of delamination and predicting the conditions for platelet stabilization. For two weakly-bound square platelets of length L in a solvent, the initial total surface energy $E_{tot,i}$ is

$$E_{tot,i} = -L^2[E_{SS} + E_{PP} + 2E_{SP}] \quad (\text{Eq. 3.1})$$

where E_{SS} , E_{PP} , E_{SP} are the intensive areal interfacial binding energies for solvent-solvent, platelet-platelet, and solvent-platelet interfaces respectively²⁷. (The solvent-solvent term is to account for the area the sheared platelet will move into). After full delamination, the total energy $E_{tot,f}$ is

$$E_{tot,f} = -L^2[4E_{SP}] \quad (\text{Eq. 3.2})$$

giving an energy change ΔE during delamination of

$$\Delta E = -L^2[2E_{SP} - E_{PP} - E_{SS}] \quad (\text{Eq. 3.3})$$

Equations 3.1-3.3 are true for all exfoliation systems. The prediction of stabilization is facilitated by the assumption of purely London dispersion forces (a component of van der Waals interactions) between the platelets (discussed in section 3.3), which results in approximating E_{SP} as the geometric mean $E_{SP} = \sqrt{E_{SS}E_{PP}}$, yielding²⁷

$$\Delta E = L^2 [\sqrt{E_{SS}} - \sqrt{E_{PP}}]^2 \quad (\text{Eq. 3.4})$$

On the basis of Eq. 3.4, it is observed that the energy change is always positive except in the case of perfect surface energy matching, corresponding to a prediction of dispersion stability; delamination requires additional energy to overcome the platelet-platelet cohesion. The magnitude of the minimum force F for breaking up the layers can be approximated by taking the derivative of Eq. 3.4 with respect to the platelet length, L , yielding

$$F = L [\sqrt{E_{SS}} - \sqrt{E_{PP}}]^2 \quad (\text{Eq. 3.5})$$

Considering the applied shear stress, $\tau = F/L^2 = \eta\dot{\gamma}$, the corresponding minimum shear rate $\dot{\gamma}$ is

$$\dot{\gamma} = \frac{[\sqrt{E_{SS}} - \sqrt{E_{PP}}]^2}{\eta L} \quad (\text{Eq. 3.6})$$

where η is the liquid viscosity. Hence, the matching of the surface energies of the solvent and platelets maximizes exfoliation at a given input energy, and suggests dispersion stability as there is no energetic penalty for the creation of new platelet-solvent interfaces compared to the original system (suggesting wetting/immersion, insertion, and exfoliation are all allowed).

Papers from Coleman's group tend to consider surface energy in understanding solvent effects, which is closely related to surface tension, Γ . These are related by $\Gamma = E_{SS} - TS_{sur}^{sol}$ where T is temperature, and S_{sur}^{sol} is the solvent surface entropy^{22,33}. (Thus, E_{SS} is the heat of vaporization,

ΔH_v , per area.) Solvent surface entropies are usually in the range of 0.07-0.14 mJ/m²K, and organic solvents tend to fall near 0.11 mJ/m²K, leading Hernandez et al. to consider $S_{sur}^{sol} \sim 0.1$ mJ/m²K for nearly all graphene solvents (and $\Gamma \approx E_{SS} - 30$ mJ/m² for organic solvents at room temperature)^{22,34}. From this, they estimate graphene has a surface energy $E_{PP} \approx 71$ mJ/m² based on the surface energies of exfoliation solvents and exfoliation is optimized by matching the surface energies of graphene and the solvent²⁷. Hernandez acknowledges that while surface energy is an important parameter, it is a “blunt tool”³⁵. Similarly, Shen argues that while total surface tension matching may be sufficient for predicting good exfoliants, it does not predict dispersal behavior³⁶, which is supported by a review of the literature below.

Much research on graphene solutions is inspired by work on the dispersion of carbon nanotubes (CNTs), due to their similar structures, e.g. nanotubes can be considered as a rolled-up graphene sheet. Peng et al. provide a good overview of solvents used in nanotube solutions and dispersions. It has been noted repeatedly that chemical structure alone is a poor predictor of a given liquid’s ability to disperse nanotubes or graphene. For instance, the aromaticity of solvent molecules or the presence of phenyl groups turns out to be an unreliable predictor of effectiveness as a nanotube or graphene solvent³⁷. Common aromatic solvents such as benzene, toluene, xylenes, and pyridine poorly disperse graphite³⁸. Good nanotube solvents tend to be characterized by high electron pair donicity (e.g. behavior as a Lewis base) and negligible hydrogen bonding, though this does not appear to be a sufficient condition as solvents like dimethylsulfoxide (DMSO) have those qualities and are still poor nanotube solvents^{29,39}. The ordering of solvent molecules imposes an entropic cost, so it is suggested that good solvents do not π -stack on nanotube sidewalls²⁹. On the other hand, graphene seems to benefit from π -stacking with solvents; a great deal of non-covalent functionalization work on graphene is based on π -stacking^{4,40}. The best CNT solvents are

dimethylformamide (DMF) and N-methyl-2-pyrrolidone (NMP), though even they still show nanotube aggregation on a timescale of days³⁹. However, Giordani et al. claim NMP solutions of nanotubes do not show re-aggregation after a storage time as long as 17 days²⁹. Kim et al. claim a stability period of over eight months for a dispersion of single-walled nanotubes in ortho-dichlorobenze (ODCB)⁴¹.

Johnson et al. propose a tentative ranking of common solvents' ability to disperse graphene based on molecular dynamics simulations and experiment: NMP \approx DMSO > DMF > GBL > H₂O (where GBL is γ -butyrolactone)⁵. As another difference from nanotubes, note that DMSO is considered a good solvent for graphene. Bourlinos et al. somewhat reject the suggestion of the nanotube literature, having found evidence of better graphene solubility in both electron donating and electron accepting π -stacking solvents and specifically report decent dispersal in pyridine⁴². NMP is the most widely used graphene solvent, followed by DMF³⁸. Graphene isolated from its graphite source can exist in concentrations up to 63 mg/mL (that fell to 33 mg/mL over 200 hours) in NMP⁵.

Initial refinements of theoretical approaches to solvent interactions with nanotubes and graphene were based on Hansen solubility parameters. The Hansen solubility parameters are meant to more quantitatively predict the solubility of materials in a solvent based on their similarity in three components of intermolecular interactions: London dispersion forces δ_d ,

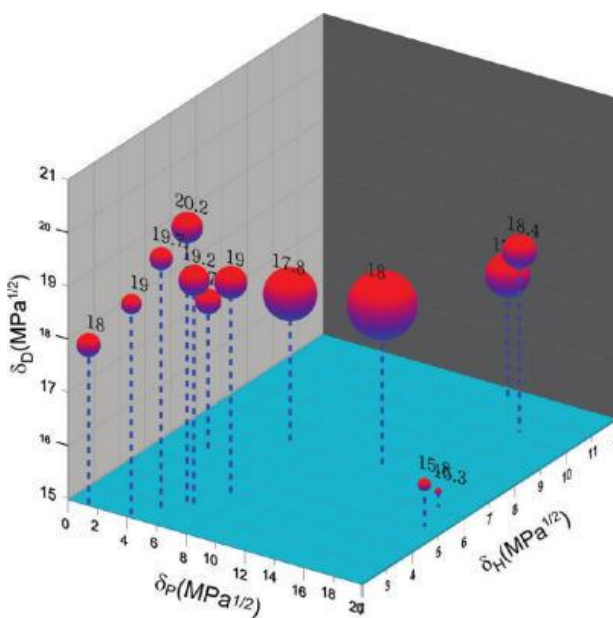


Figure 3-5. Position of nanotube solvents in Hansen parameter space. The text value is the exact δ_D value. Sphere size represents relative solubility. From Cheng et al, 2010^{Ref 44}.

(permanent) polar interactions δ_p , and hydrogen bonding δ_h . The total Hansen solubility parameter δ_t is related to the component parameters by $\delta_t^2 = \delta_d^2 + \delta_p^2 + \delta_h^2$ ⁴³. The total parameter is sometimes called the Hildebrand solubility parameter, based on earlier work on a one-component theory of solubility. The Hildebrand parameter is also directly given by $\delta_t = \sqrt{c} = \sqrt{\frac{\Delta H_v - RT}{V_m}} \approx V_m^{-1/6} \sqrt{E_{SS} - (RT)/V_m^{4/3}}$, where c is the cohesive energy density, ΔH_v is the heat of vaporization, R is the universal gas constant, T is the temperature, and V_m is the molar volume³⁰. The Hansen parameters are then the square root of the portions of the molecular cohesive energies attributed to the respective interactions. Hansen and Hildebrand solubility parameters have units of (energy/volume)^{1/2}, equating to (pressure)^{1/2}.

Cheng et al. claim to not see a relationship between the dispersion parameter and solubility of nanotubes, but this relationship may be obscured by the relatively narrow range of dispersion parameters they used (they only varied from 17.4-20.2 MPa^{1/2} in the studied solvents)³⁰. In another paper with a wider range of values, Cheng goes further to argue that the dispersion parameter is inappropriate in determining a “good” nanotube solvent because solvents with similar δ_D may still be poor based on the other components⁴⁴. But the graph (Figure 3-5 above) from that paper suggests they are getting the order wrong: while liquids with similar δ_D may have very different graphene solubilities based on the other Hansen parameters, one almost never finds a good solvent with δ_D far away from the suggested value of 18 MPa^{1/2}.

Regarding nanotube solvents, Ham suggests the minimum value of the dispersive component is 16.5 MPa^{1/2}, and for surfactants recommends a molar volume of at least 179.5 cm³/mol⁴⁵. This carries over into the graphene literature. Good solvents for graphene have δ_D between 15 and 21 MPa^{1/2}, and dispersed concentration peaks at around 18. Hernandez et al.

calculated the Hansen parameters of graphene: $\delta_D=18.0 \text{ MPa}^{1/2}$, $\delta_P=9.3 \text{ MPa}^{1/2}$, and $\delta_H=7.7 \text{ MPa}^{1/2}$. In that paper, they also note that it is interesting that good graphene solvents are characterized by non-zero values for δ_P and δ_H , as one would expect a nonpolar substance like graphene to be described almost entirely by the London dispersion component (and the similar fullerene C_{60} is)³⁵.

However, even the more complicated Hansen solubility parameter approach does not fully capture the solution behavior of graphene and nanotubes, especially with regard to exfoliation. For instance, the dispersion concentration can vary widely between solutions with similar Hansen parameters, which should not occur in the Hansen framework⁴⁶. In Hernandez et al.'s study, cyclopentanone, the solvent with Hansen parameters closest matched to graphene had significantly less few-layer graphene after exfoliation compared to NMP, but dispersed almost twice as much material³⁵.

Bergin et al. proposed a set of solubility parameters for nanotubes based on surface energy (instead of Hansen's based on cohesive energy), but still see the same spread in dispersibility for similar values⁴⁶. Shen et al. follow a similar route looking at the polar and dispersive components of just the surface tension. In matching the relative values of the surface tension components in the solvent mixture and 2D material they claim to achieve better dispersibility for various 2D materials than studies optimizing Hansen parameters, though these ratios did not maximize exfoliation. Because the cosolvents contained low-boiling point solvents, they may also be more suitable for processing into polymer composites³². They measure the polar to dispersive component of surface tension for 2D materials as follows: 0.471 for graphite, 0.563 for WS₂, 0.449 for MoS₂, 0.45 for h-BN. In their work, most effective solvents for graphite and WS₂ have surface tensions around 40 mN/m, agreeing with Paton again for graphene/graphite³⁶.

3.3 Interaction Forces in Colloids

The benefit of using the surface energy matching approach in Section 3.2 is that solvent surface energies, E_{SS} , can be readily calculated or obtained from available macroscopic thermodynamic data. This availability leads to the calculation of platelet surface energies, E_{PP} , and facilitates the development of experimental correlations that predict platelet stability in common processing solvents. However, use of the approach in Section 3.2 introduces several drawbacks that limit accuracy and applicability. First, researchers such as Paton focus only on the enthalpic contribution to the free energy of platelet mixing, thus ignoring the entropic (or configurational) contribution, which also effects platelet delamination and stability. Second, the assumption of London dispersion interactions, which leads to convenient relationships for the mixing energy and minimum force of delamination in Equations 3.4 and 3.5, yield order of magnitude estimates. Third, common organic solvents within a desirable surface tension range ($\Gamma \approx 30\text{-}40 \text{ mJ/m}^2$) are limited in number. Fourth, common organic solvents possess low viscosities ($\eta \approx 1 \text{ cP}$) resulting in high minimum shear rates for exfoliation.

A more fundamental, microscopic approach can be used to address the drawbacks. The starting point is the always true relations for exfoliation in Equations 3.1-3.3. The intensive areal interfacial binding energies E_{PP} , E_{PS} , and E_{SS} for the dispersion of the platelets in the solvent are estimated from the Hamaker constant, A , for the whole process depicted in Figure 3- 6. The platelet-platelet, platelet-solvent, and solvent-solvent interactions are quantum-mechanical in origin, stemming from the charge fluctuations between the condensed phases. The Hamaker constant for colloidal bodies can be estimated from the pairwise summation of the atoms in the material. For example, consider the Lennard-Jones potential,

$$\varphi_T(r) = -\frac{B}{r^6} + \frac{S}{r^{12}} \quad (\text{Eq. 3.7})$$

where $\varphi_T(r)$ is the isotropic intermolecular interaction potential energy, r the intermolecular separation distance, B the van der Waals constant representing the (relatively) long-range attraction between molecules, and S the constant that captures the short-range intermolecular repulsion between overlapping electron clouds. (The three-dimensional cohesive energy density, c , discussed in Section 3.2, is the attractive term in Equation 3.7, $-B/r_m^6$, at r_m corresponding to intermolecular distances in the condensed phase.)

Integrating over all molecules between two macroscopic surfaces separated by a distance D , yields the attractive free energy, φ_{PP} , between platelets of length, L .

$$\varphi_{PP}(D) = -\frac{A}{12\pi D^2} L^2 \quad (\text{Eq. 3.8})$$

The Hamaker constant A is $B \left(\frac{\rho N_A \pi}{M} \right)^2$ where ρ is the material density, M the molar mass, and N_A the Avogadro's number. The platelet cohesion energy, E_{PP} , can be estimated by calculating φ_{PP} between graphene platelets with D equal to the equilibrium graphite interlayer spacing 3.35 Å. Using the pairwise-summation approximation simplifies the prediction of van der Waals interactions between colloidal bodies and results in relationships like Equation 3.8 that depend on a material-specific constant and material dimensions. This informs the development of experiments that lead to the tabulation of Hamaker constants or their direct calculation.

The van der Waals constant B can be estimated by summing the contributions from the London dispersion force of instantaneous induced dipole-induced dipole interactions, the Debye force between permanent and induced dipoles, and the Keesom force between permanent dipoles, in Equations 3.9-3.11

$$B_{London} = -\frac{3\alpha_{0,1}\alpha_{0,2}}{4(4\pi\epsilon_0\epsilon_M)^2} \frac{I_1 I_2}{I_1 + I_2} \quad (\text{Eq. 3.9})$$

$$B_{Debye} = -\frac{\mu_1\alpha_{0,2} + \mu_2\alpha_{0,1}}{(4\pi\epsilon_0\epsilon_M)^2} \quad (\text{Eq. 3.10})$$

$$B_{Keesom} = -\frac{\mu_1\mu_2}{3(4\pi\epsilon_0\epsilon_M)^2k_B T} \quad (\text{Eq. 3.11})$$

where $\alpha_{0,1}$ and $\alpha_{0,2}$ are the static polarizabilities of molecules 1 and 2 (excess polarizabilities in media besides free vacuum), I_1 and I_2 the ionization energies of the respective molecules, ϵ_0 the permittivity of free space, ϵ_M the dielectric constant of the dispersing medium, μ_1 and μ_2 the respective dipole moments of the molecules, k_B is the Boltzmann constant, and T the temperature of the system. On the basis of Equation 8, the Hamaker constant has units of energy, and so one can consider Hamaker constants for the whole delamination process,

$$A = A_{PP} + A_{SS} - 2A_{SP} \quad (\text{Eq. 3.12})$$

which mirrors Equation 3.3. To determine A_{PP} for nonpolar materials like graphene, the van der Waals force can be approximated as just being the result of the dispersion force, and so B is just B_{London} . The Hamaker constant for the solvent A_{SS} can be found similarly by calculating it from B , using a D corresponding to the intermolecular distance in the liquid phase, or by looking up tables of Hamaker values for many common solvents.

The ionization energies for various forms of carbon can be found in the literature; however, care should be taken in their use. For example, as graphene is a chemically bound molecule with an electronic structure distinct from a carbon atom, one should not substitute the ionization energy of carbon (11.26 eV) for graphene. For comparison, structurally similar groups of chemicals - polycyclic aromatic hydrocarbons and the fullerenes - show significantly lower ionization energies than isolated carbon atoms^{47,48}. As the number of sp^2 -bound carbons in the polycyclic aromatic structure increases, the ionization energy approaches the work function of graphite/graphene, and this trend is predicted both by classical and density functional theory calculations^{49,50}. Graphite is reported to have a thermionic work function of 4.34 eV and a photoelectric work function of 4.81 eV⁵¹, but the reported value of 4.7 eV for bilayer graphene is a more appropriate choice⁵². (The

4.81 eV value is reported in its reference as carbon without specifying allotrope, but they fit older literature values of graphite⁴⁹ and low-doped diamond's photoelectric work function for commonly cited faces is not close to those values⁵³.)

The excess α_1 polarizability of a molecule 1 compared to its dispersing medium can be calculated from macroscopic properties as⁵⁴

$$\rho_{N,1}\alpha_1 = 2\varepsilon_0\varepsilon_M(\varepsilon_1 - \varepsilon_M)/(\varepsilon_1 + \varepsilon_M) \quad (\text{Eq. 3.13})$$

where $\rho_{N,1}$ is the number density of molecule 1 ($\rho_N = \frac{\rho N_A}{M}$) and ε_1 its dielectric constant. We consider the relative difference in polarizabilities because this affects the propagation of the dispersion force. Differences in polarizability reflect differences in the response of the molecules' electrons to the electric field of the instantaneous dipoles. Compared to identical molecules, this leads to interaction effects that are less correlated and increase the system energy. At the macroscopic scale, this is found as reflections or changes in electric field strength at interfaces between different dielectrics⁵⁵. The use of macroscopic values is also useful as they implicitly take into account higher-order interactions between molecules in the condensed phase unlike the pairwise summation based only on molecular polarizabilities.

In our system, molecules 1 and 2 are identical. Following the derivation laid out in Chapter 11 of Israelachvili, we approximate the frequency dependence of the dielectric constant for our range of interest (the ultraviolet and visible spectrum) as $\varepsilon(i\nu) = 1 + (n^2 - 1)/(1 + \frac{\nu^2}{\nu_e^2})$, where ν_e is the frequency corresponding to the first ionization energy (and also assuming ν_e is close enough for the material and medium we can approximate them as one value). This then gives a slightly simplified estimate of the Hamaker constant A_{SP} for identical platelets dispersed in a solvent based on the macroscopic properties of the materials and ionization frequency⁵⁴:

$$A_{SP} = \left[\frac{3}{4} k_B T \left(\frac{\varepsilon_1 - \varepsilon_M}{\varepsilon_1 + \varepsilon_M} \right)^2 \right] + \frac{3h\nu_e}{16\sqrt{2}} \frac{(n_1^2 - n_M^2)^2}{(n_1^2 + n_M^2)^{3/2}} \quad (\text{Eq. 3.14})$$

The first term (in brackets) represents the summed Keesom and Debye contribution and the second term is the London contribution. The dielectric constant and index of refraction are related by $n = \varepsilon^{1/2}$, and so one could further simplify the equation to just be in dielectric or refractive index terms.

Though simplified, this Hamaker constant calculation yields an important insight: a system where the particles and medium have similar dielectric constants/refractive indices experiences weaker attractive forces than a system with more dissimilar constants. In the “index-matched” limit, the Hamaker constant drops to zero and the van der Waals forces between particles essentially vanish. This ties in well with notions of the importance of the Hansen dispersion parameter, as these values all reflect the polarizability of molecules. The refractive index and the dielectric constant can both be related to the polarizability through the Clausius-Mossotti and Lorentz-Lorenz equations, respectively, as follows

$$\frac{\alpha}{4\pi\varepsilon_0} = \left(\frac{\varepsilon - 1}{\varepsilon + 2} \right) \frac{3\nu}{4\pi} \quad (\text{Eq. 3.15})$$

$$\frac{\alpha_0}{4\pi\varepsilon_0} = \left(\frac{n^2 - 1}{n^2 + 2} \right) \frac{3\nu}{4\pi} \quad (\text{Eq. 3.16})$$

where in these equations ν represents the molecular volume and α_0 represents the electronic polarizability, the component that is attributed only to the displacement of the molecule’s electron cloud⁵⁵. An objective of this research is to apply the understanding of index matching to improve the selection of processing solvents, as I hypothesize matching the refractive indices of the platelets and solvent will be a more accurate predictor of graphene stability.

3.4 Motivation

3.4.1 Functionalization of Graphene

Many different kinds of functionalization are performed on graphene depending on desired applications, but I will focus on the addition of oligomers and polymers to the surface of graphene. (In particular, “functionalized graphene sheets” that are primarily reactive derivatives of graphene oxide⁵⁶ are excluded from this review.) Such functionalization is most often performed with two goals in mind. First, functionalizing graphene in solution can improve dispersion stability as the polymer chains contribute a steric repulsion to the interparticle interactions, and may also have favorable interactions with the solvent molecules. It has also been found that polymers in solution may improve the exfoliation of graphene. For instance, graphene has been exfoliated in organic solvents with polystyrene⁵⁷. Second, functionalization is often done as part of preparing graphene flakes for incorporation into a polymer nanocomposite. Pristine graphene is essentially unworkable for composites, especially mechanical composites, without some surface modification as the modifier helps transfer load from the bulk matrix to the graphene flakes.⁵⁸ Polymer composites with only a few weight percent of graphene as a filler have drastically improved mechanical and electronic properties compared to the pure polymer⁵⁹, and this has inspired a great deal of interest in new graphene/polymer nanocomposites for a wide variety of applications.

Georgakilas and Layek provide a comprehensive overview of contemporary approaches to graphene functionalization for general applications in their reviews^{4,58}. Functionalization is mainly done through covalent bonding of the polymers to graphene (or its related materials), but there is interest in noncovalent

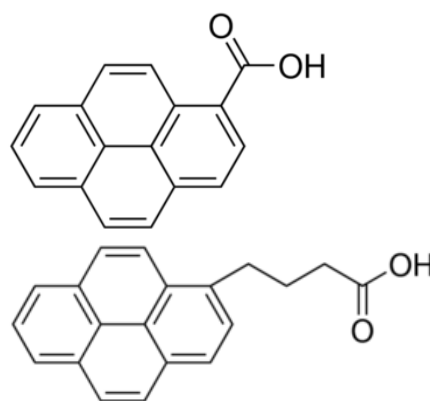


Figure 3-6. Short chain derivatives of pyrene used in references^{61,62}.

functionalization to avoid disruption to the sp^2 bonding network and preserve graphene's electronic properties. Covalent functionalization can be divided into broad approaches – “grafting to” and “grafting from”. In “grafting to” techniques, the polymer chains are already made and reactions are performed to bond the polymer to the graphene surface. In “grafting from” techniques, the polymer is actually synthesized from initiators on the surface. Grafting to a surface is considered easier, but it generally cannot accommodate high graft densities because of steric hindrances as more chains graft to the surface and reaction times can be long due to the slow diffusion of polymers. Because there are no initial chains to crowd out others, grafting from can result in higher graft densities and longer chains. Atom transfer radical polymerization (ATRP) and reversible addition fragmentation chain transfer (RAFT) are commonly used as grafting from techniques, and they can enable control over the molecular weight and polydispersity of the resulting polymers⁵⁸. When looking at graphene functionalization literature, it is important to pay attention to the actual graphene-related material. Graphene oxide is an easier starting material to work with because of its surface functional groups and many studies use that instead of pristine graphene. Layek's discussion of both grafting to and grafting from studies is almost completely about papers starting with graphene oxide. (In some studies, the final material may be considered an RGO composite because of a reduction reaction that occurs during functionalization.) Georgakilas points out that there are some covalent functionalization studies of pristine graphene based on adding free radicals to the surface or reactions between dienophiles and the C-C double bonds in graphene⁴.

Noncovalent functionalization is based on interactions like hydrogen bonding or π - π stacking, which can attract ligands to the GRM surface, but do not add sp^3 defects that would disrupt its electronic properties. Many researchers are interested in ligands with a pyrene moiety⁵⁸,

the smallest peri-fused polycyclic aromatic hydrocarbon⁶⁰. The pyrene end will π -stack with graphene and other parts of the ligand can have other functionalities. Most work with pyrene uses short molecules^{61,62}, but there are some studies where a long polymer is modified to have or is synthesized with a pyrene end^{63,64}. Non-ionic surfactants are believed to stabilize graphene in aqueous solutions through adsorption of hydrophobic tail groups onto the graphene surface while hydrophilic head groups spread into the water and will sterically repel each other⁴⁰.

Most work on graphene/polymer composites has excluded the physics of interfacial wetting between the matrix polymers and filler surfaces that governs dispersion. The nature of polymers does not always favor the incorporation of filler materials, especially in longer polymers. This is because configurational entropy, or the desire of free matrix chains to maximize their free volume, drives fillers from the matrix, leading to filler aggregation⁶⁵. Even if the graphene is well-dispersed, poor adhesion between the matrix and graphene can concentrate stress, leading to premature failure at the interface instead of effectively transferring stress between the matrix and platelets⁵⁶. Attaching chains to the surface is not

sufficient for dispersion stability if the free polymer chains in the bulk do not wet, or interpenetrate, the graft chains on the surface⁶⁶. Interpenetration between graft and bulk chains improves dispersibility and improves the transfer of stress from the matrix to the filler. Our group has studied particle stability in concentrated polymers⁶⁷. Figure 3-7 shows the phase diagram of homopolymer wetting. Particles aggregate in the allophobic and autophobic regimes due to the expulsion of the

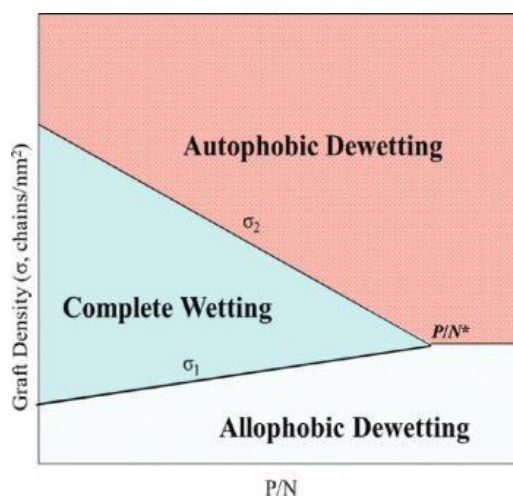


Figure 3-7. Phase diagram of free polymer chains wetting grafted chains. P/N is ratio of free and graft polymer molecular weights. From Sunday et al., 2010^{Ref 68}

free polymer from the grafts, and particles disperse uniformly in the complete wetting regime where free and graft polymers interpenetrate. Our group was the first to achieve such high particle loadings (over 50% by volume) in a polymer nanocomposite by varying the grafting density and free/graft chain length ratio to optimize for complete wetting⁶⁸⁻⁷¹.

Functionalization of graphene is currently restricted by the available solvents for dispersions. The current standard solvents of NMP and DMF are highly polar, which are not suitable for a variety of reactions, and hygroscopic, which can limit the long-term stability of the graphene dispersion as water is absorbed^{38,72}. Inspired by its use as a solvent for fullerene reactions and its ability to disperse single-walled carbon nanotubes, the Tour group proposed ODCB as a potential solvent and dispersant for graphene. ODCB is non-polar, which could make it useful for certain graphene functionalization reactions. In their work, the Tour group noted that ODCB performed very well, unlike a reference group of standard solvents, including (mono)chlorobenzene³⁸. This does not seem to have caught on yet in the graphene dispersion literature, as ODCB is rarely used in most experiments. Another concern with several solvents is the relatively high boiling point, which may make it hard to fully remove solvent molecules in further processing steps⁴⁰. A more rigorous understanding of the role of solvent physical properties would enable engineers and chemists to more rationally select solvents and avoid properties that are undesirable for functionalization and additional processing reactions.

3.4.2 Future Solvents: Designed Ionic Liquids

Any ionic salt is technically an ionic liquid in its molten state. However, the term has mostly come to refer to room-temperature ionic liquids as research over the last few decades has focused on the many potential applications that are possible with their specific properties. These room-temperature ionic liquids commonly consist of organic cationic species and inorganic anionic species⁷³. They have no measurable vapor pressure and so do not release volatile organic

compounds, making them attractive for “green chemistry” applications. They can also be a potential solvent for many different kinds of chemical reactions.⁷⁴ What makes ionic liquids so attractive is the ability to customize them as “designer solvents” for specific processes. Their combinatorial nature opens up a parameter space of millions of liquids chosen with particular properties in mind based on the selection of specific cations, anions, and substituents. As a very basic rule of thumb, an ionic liquid’s chemical properties tend to be controlled by the anion and physical properties like density and viscosity tend to be controlled by the cation⁷³.

There has been much interest in using ionic liquids to exfoliate and disperse graphene over the last few years, again based on previous work in the nanotube literature^{37,75}. As such, the use of ionic liquids could greatly expand the range of exfoliation and dispersion solvents. Ionic liquids typically have viscosities that are two or three orders of magnitude larger than most organic solvents, which should dramatically reduce the critical shear rate of exfoliation. For instance, the room temperature viscosities of organic solvents like ODCB, NMP, and cyclopentanone are 1.32, 1.65, and 1.29 cP, respectively. In contrast, the room temperature viscosity of the ionic liquid 1-hexyl-3-methylimidazolium bis(trifluoromethylsulfonyl)imide ([C6mim][NTf2]), is 70 cP. Bis(hydroxyethyl)ammonium acetate ([NHEH,(C2OH)2][OAc]) has an even higher viscosity of 5647 cP.⁷⁶ Furthermore, ionic liquids possess a wider range of polarizabilities, as reflected through the index of refraction, which can be used to reduce platelet-platelet attraction and increase dispersion stability per the discussion in section 1.3. The refractive indices for the simple solvents ODCB, NMP, and cyclopentanone are narrow (1.55, 1.47, and 1.44, respectively). Ionic liquids have refractive indices in a range from 1.37 to 1.55⁷⁷.

Nuvoli was able to exfoliate up to 5.33 mg/mL of graphene in 1-hexyl-3-methylimidazolium hexafluorophosphate by sonication, the highest reported concentration of graphene

in any solvent⁷⁸. However, it is important to note that several of these studies, including Nuvovli's, use ionic liquids with the tetrafluoroborate ($[\text{BF}_4]^-$) or hexafluorophosphate ($[\text{PF}_6]^-$) anions^{37,79–81}, which can generate hydrofluoric acid in the presence of water and so is unlikely to be preferred in large-scale processes⁷³. Additionally, many of these studies do not directly exfoliate graphite into graphene³⁷, and very few do so through shear exfoliation^{75,82}. Better understanding of the role of viscosity and polarizability will enable design of ionic liquids specifically tuned to the exfoliation and dispersion of graphene for specific applications, and could also be generalized to designing ionic liquids for exfoliation of other 2D materials.

3.5 References for Chapter 3

1. Bianco, A. *et al.* All in the graphene family – A recommended nomenclature for two-dimensional carbon materials. *Carbon N. Y.* **65**, 1–6 (2013).
2. Partoens, B. & Peeters, F. M. From graphene to graphite: Electronic structure around the K point. *Phys. Rev. B - Condens. Matter Mater. Phys.* **74**, 1–11 (2006).
3. Fang, M., Wang, K., Lu, H., Yang, Y. & Nutt, S. Covalent polymer functionalization of graphene nanosheets and mechanical properties of composites. *J. Mater. Chem.* **19**, 7098 (2009).
4. Georgakilas, V. *et al.* Functionalization of Graphene: Covalent and Non-Covalent Approaches, Derivatives and Applications. *Chem. Rev.* **112**, 6156–6214 (2012).
5. Johnson, D. W., Dobson, B. P. & Coleman, K. S. A manufacturing perspective on graphene dispersions. *Curr. Opin. Colloid Interface Sci.* **20**, 367–382 (2015).
6. Wick, P. *et al.* Classification Framework for Graphene-Based Materials. *Angew. Chemie Int. Ed.* **53**, 7714–7718 (2014).
7. Gómez-Navarro, C. *et al.* Atomic structure of reduced graphene oxide. *Nano Lett.* **10**, 1144–1148 (2010).
8. Geim, A. K. & Novoselov, K. S. The rise of graphene. *Nat. Mater.* **6**, 183–191 (2007).
9. Lee, C., Wei, X., Kysar, J. W. & Hone, J. Measurement of the Elastic Properties and Intrinsic Strength of Monolayer Graphene. *Science (80-.)*. **321**, 385–388 (2008).
10. Zurutuza, A. & Marinelli, C. Challenges and opportunities in graphene commercialization. *Nat. Nanotechnol.* **9**, 730–734 (2014).

11. Ahn, J. *et al.* Things you could do with graphene. *Nat. Nanotechnol.* **9**, 737–737 (2014).
12. Perreault, F., Fonseca de Faria, A. & Elimelech, M. Environmental applications of graphene-based nanomaterials. *Chem. Soc. Rev.* **44**, 5861–5896 (2015).
13. Choi, W., Lahiri, I., Seelaboyina, R. & Kang, Y. S. Synthesis of Graphene and Its Applications: A Review. *Crit. Rev. Solid State Mater. Sci.* **35**, 52–71 (2010).
14. Aghigh, A. *et al.* Recent advances in utilization of graphene for filtration and desalination of water: A review. *Desalination* **365**, 389–397 (2015).
15. Unalan, I., Cerri, G. & Marcuzzo, E. Nanocomposite films and coatings using inorganic nanobuilding blocks (NBB): current applications and future opportunities in the food packaging sector. *RSC Adv.* 29393–29428 (2014). doi:10.1039/c4ra01778a
16. Khurana, I., Saxena, A., Bharti, Khurana, J. M. & Rai, P. K. Removal of Dyes Using Graphene-Based Composites: a Review. *Water, Air, Soil Pollut.* **228**, 180 (2017).
17. Ferrari, A. C. *et al.* Science and technology roadmap for graphene, related two-dimensional crystals, and hybrid systems. *Nanoscale* **7**, 4598–4810 (2015).
18. Avouris, P. & Dimitrakopoulos, C. Graphene: Synthesis and applications. *Mater. Today* **15**, 86–97 (2012).
19. Novoselov, K. S. *et al.* Electric Field Effect in Atomically Thin Carbon Films. *Science* (80-.). **306**, 666–669 (2004).
20. Talyzin, A. V. *et al.* Nanocarbons by high-temperature decomposition of graphite oxide at various pressures. *J. Phys. Chem. C* **113**, 11279–11284 (2009).
21. Stankovich, S. *et al.* Synthesis of graphene-based nanosheets via chemical reduction of exfoliated graphite oxide. *Carbon N. Y.* **45**, 1558–1565 (2007).
22. Hernandez, Y. *et al.* High-yield production of graphene by liquid-phase exfoliation of graphite. *Nat. Nanotechnol.* **3**, 563–568 (2008).
23. Yi, M. & Shen, Z. A review on mechanical exfoliation for the scalable production of graphene. *J. Mater. Chem. A* **3**, 11700–11715 (2015).
24. Arao, Y., Mizuno, Y., Araki, K. & Kubouchi, M. Mass production of high-aspect-ratio few-layer-graphene by high-speed laminar flow. *Carbon N. Y.* **102**, 330–338 (2016).
25. Varrla, E. *et al.* Turbulence-assisted shear exfoliation of graphene using household detergent and a kitchen blender. *Nanoscale* **6**, 11810–11819 (2014).
26. Bracamonte, M. V., Lacconi, G. I., Urreta, S. E. & Foa Torres, L. E. F. On the Nature of Defects in Liquid-Phase Exfoliated Graphene. *J. Phys. Chem. C* **118**, 15455–15459 (2014).

27. Paton, K. R. *et al.* Scalable production of large quantities of defect-free few-layer graphene by shear exfoliation in liquids. *Nat. Mater.* **13**, 624–630 (2014).
28. Yi, M. & Shen, Z. Kitchen blender for producing high-quality few-layer graphene. *Carbon N. Y.* **78**, 622–626 (2014).
29. Giordani, S. *et al.* Debundling of single-walled nanotubes by dilution: Observation of large populations of individual nanotubes in amide solvent dispersions. *J. Phys. Chem. B* **110**, 15708–15718 (2006).
30. Cheng, Q., Debnath, S., Gregan, E. & Byrne, H. J. Effect of Solvent Solubility Parameters on the Dispersion of Single-Walled Carbon Nanotubes. *J. Phys. Chem. C* **112**, 20154–20158 (2008).
31. Gilje, S. *et al.* Processable aqueous dispersions of graphene nanosheets. *Nat. Nanotechnol.* **3**, 101–105 (2008).
32. Shen, J. *et al.* Surface Tension Components Based Selection of Cosolvents for Efficient Liquid Phase Exfoliation of 2D Materials. *Small* **12**, 2741–2749 (2016).
33. Lyklema, J. The surface tension of pure liquids: Thermodynamic components and corresponding states. *Colloids Surfaces A Physicochem. Eng. Asp.* **156**, 413–421 (1999).
34. Tsierkezos, N. G. & Filippou, A. C. Thermodynamic investigation of N,N-dimethylformamide/toluene binary mixtures in the temperature range from 278.15 to 293.15K. *J. Chem. Thermodyn.* **38**, 952–961 (2006).
35. Hernandez, Y., Lotya, M., Rickard, D., Bergin, S. D. & Coleman, J. N. Measurement of Multicomponent Solubility Parameters for Graphene Facilitates Solvent Discovery. *Langmuir* **26**, 3208–3213 (2010).
36. Shen, J. *et al.* Liquid Phase Exfoliation of Two-Dimensional Materials by Directly Probing and Matching Surface Tension Components. *Nano Lett.* **15**, 5449–5454 (2015).
37. Peng, R., Wang, Y., Tang, W., Yang, Y. & Xie, X. Progress in Imidazolium Ionic Liquids Assisted Fabrication of Carbon Nanotube and Graphene Polymer Composites. *Polymers (Basel)*. **5**, 847–872 (2013).
38. Hamilton, C. E., Lomeda, J. R., Sun, Z., Tour, J. M. & Barron, A. R. High-Yield Organic Dispersions of Unfunctionalized Graphene. *Nano Lett.* **9**, 3460–3462 (2009).
39. Ausman, K. D., Piner, R., Lourie, O., Ruoff, R. S. & Korobov, M. Organic Solvent Dispersions of Single-Walled Carbon Nanotubes: Toward Solutions of Pristine Nanotubes. *J. Phys. Chem. B* **104**, 8911–8915 (2000).
40. Niu, L. *et al.* Production of Two-Dimensional Nanomaterials via Liquid-Based Direct Exfoliation. *Small* **12**, 272–293 (2016).

41. Kim, D. S., Nepal, D. & Geckeler, K. E. Individualization of Single-Walled Carbon Nanotubes: Is the Solvent Important? *Small* **1**, 1117–1124 (2005).
42. Bourlinos, A. B., Georgakilas, V., Zboril, R., Sterioti, T. a. & Stubos, A. K. Liquid-Phase Exfoliation of Graphite Towards Solubilized Graphenes. *Small* **5**, 1841–1845 (2009).
43. Hansen, C. M. The Three Dimensional Solubility Parameter and Solvent Diffusion Coefficient: Their Importance in Surface Coating Formulation. (Technical University of Denmark, 1967).
44. Cheng, Q. *et al.* Systematic Study of the Dispersion of SWNTs in Organic Solvents. *J. Phys. Chem. C* **114**, 4857–4863 (2010).
45. Ham, H. T., Choi, Y. S. & Chung, I. J. An explanation of dispersion states of single-walled carbon nanotubes in solvents and aqueous surfactant solutions using solubility parameters. *J. Colloid Interface Sci.* **286**, 216–223 (2005).
46. Bergin, S. D. *et al.* Multicomponent Solubility Parameters for Single-Walled Carbon Nanotube–Solvent Mixtures. *ACS Nano* **3**, 2340–2350 (2009).
47. Gallegos, E. J. Mass spectrometry and ionization energies of some condensed-ring aromatic and heterocyclic compounds. *J. Phys. Chem.* **72**, 3452–3456 (1968).
48. Steger, H., Holzapfel, J., Hielscher, A., Kamke, W. & Hertel, I. V. Single-photon ionization of higher fullerenes C76, C78 and C84. Determination of ionization potentials. *Chem. Phys. Lett.* **234**, 455–459 (1995).
49. Smith, F. T. Capacitive Energy and the Ionization of Aromatic Hydrocarbons. *J. Chem. Phys.* **34**, 793–801 (1961).
50. Lewis, G. R., Bunting, W. E., Zope, R. R., Dunlap, B. I. & Ellenbogen, J. C. Smooth scaling of valence electronic properties in fullerenes: From one carbon atom, to C60, to graphene. *Phys. Rev. A* **87**, 052515 (2013).
51. Mechtly, E. A. Properties of Materials. in *Reference Data for Engineers* 4-1-4–33 (Elsevier, 2002). doi:10.1016/B978-075067291-7/50006-6
52. Yu, Y.-J. *et al.* Tuning the Graphene Work Function by Electric Field Effect. *Nano Lett.* **9**, 3430–3434 (2009).
53. Diederich, L., Küttel, O. M., Aebi, P. & Schlapbach, L. Electron affinity and work function of differently oriented and doped diamond surfaces determined by photoelectron spectroscopy. *Surf. Sci.* **418**, 219–239 (1998).
54. Israelachvili, J. van der Waals Forces Between Surfaces. in *Intermolecular and Surface Forces* 176–212 (Academic Press, 1992).
55. Israelachvili, J. Interactions Involving the Polarization of Molecules. in *Intermolecular*

- and Surface Forces* 67–82 (Academic Press, 1992).
56. Ramanathan, T. *et al.* Functionalized graphene sheets for polymer nanocomposites. *Nat. Nanotechnol.* **3**, 327–31 (2008).
 57. May, P., Khan, U., Hughes, J. M. & Coleman, J. N. Role of solubility parameters in understanding the steric stabilization of exfoliated two-dimensional nanosheets by adsorbed polymers. *J. Phys. Chem. C* **116**, 11393–11400 (2012).
 58. Layek, R. K. & Nandi, A. K. A review on synthesis and properties of polymer functionalized graphene. *Polymer (Guildf)*. **54**, 5087–5103 (2013).
 59. Kim, H., Abdala, A. A. & Macosko, C. W. Graphene/Polymer Nanocomposites. *Macromolecules* **43**, 6515–6530 (2010).
 60. ortho- and peri-fused (polycyclic compounds). in *IUPAC Compendium of Chemical Terminology* (IUPAC). doi:10.1351/goldbook.O04333
 61. Xu, Y., Bai, H., Lu, G., Li, C. & Shi, G. Flexible Graphene Films via the Filtration of Water-Soluble Noncovalent Functionalized Graphene Sheets. *J. Am. Chem. Soc.* **130**, 5856–5857 (2008).
 62. An, X., Butler, T. W., Washington, M., Nayak, S. K. & Kar, S. Optical and Sensing Properties of 1-Pyrenecarboxylic Acid-Functionalized Graphene Films Laminated on Polydimethylsiloxane Membranes. *ACS Nano* **5**, 1003–1011 (2011).
 63. Liu, J. *et al.* Synthesis, Characterization, and Multilayer Assembly of pH Sensitive Graphene–Polymer Nanocomposites. *Langmuir* **26**, 10068–10075 (2010).
 64. Liu, J. *et al.* Thermosensitive graphene nanocomposites formed using pyrene-terminal polymers made by RAFT polymerization. *J. Polym. Sci. Part A Polym. Chem.* **48**, 425–433 (2010).
 65. Sunday, D. F. & Green, D. L. Thermal and Rheological Behavior of Polymer Grafted Nanoparticles. *Macromolecules* **48**, 8651–8659 (2015).
 66. Maas, J. H., Leermakers, F., Fleer, G. J. & Cohen Stuart, M. a. When tethered chains meet free ones; the stability of polymer wetting films on polymer brushes. in *Macromolecular Symposia* **191**, 69–79 (2003).
 67. Dutta, N. & Green, D. L. Nanoparticle stability in semidilute and concentrated polymer solutions. *Langmuir* **24**, 5260–9 (2008).
 68. Sunday, D., Ilavsky, J. & Green, D. L. A Phase Diagram for Polymer-Grafted Nanoparticles in Homopolymer Matrices. *Macromolecules* **45**, 4007–4011 (2012).
 69. McEwan, M., Egorov, S., Ilavsky, J., Green, D. L. & Yang, Y. Mechanical reinforcement of polymer nanocomposites: theory and ultra-small angle X-ray scattering (USAXS)

- studies. *Soft Matter* **7**, 2725 (2011).
70. Dutta, N. & Green, D. L. Impact of solvent quality on nanoparticle dispersion in semidilute and concentrated polymer solutions. *Langmuir* **26**, 16737–16744 (2010).
 71. McEwan, M. & Green, D. L. Rheological impacts of particle softness on wetted polymer-grafted silica nanoparticles in polymer melts. *Soft Matter* **5**, 1705 (2009).
 72. Tessonier, J. P. & Barteau, M. A. Dispersion of alkyl-chain-functionalized reduced graphene oxide sheets in nonpolar solvents. *Langmuir* **28**, 6691–6697 (2012).
 73. Stark, A. & Seddon, K. R. Ionic Liquids. in *Kirk-Othmer Encyclopedia of Chemical Technology* **26**, 836–920 (John Wiley & Sons, Inc., 2007).
 74. Nelson, W. M. Are Ionic Liquids Green Solvents? in *Ionic Liquids: Industrial Applications to Green Chemistry* (eds. Rogers, R. D. & Seddon, K. R.) 30–41 (Oxford University Press, 2002).
 75. Ravula, S., Baker, S. N., Kamath, G. & Baker, G. A. Ionic liquid-assisted exfoliation and dispersion: stripping graphene and its two-dimensional layered inorganic counterparts of their inhibitions. *Nanoscale* **7**, 4338–4353 (2015).
 76. Yu, G., Zhao, D., Wen, L., Yang, S. & Chen, X. Viscosity of ionic liquids: Database, observation, and quantitative structure-property relationship analysis. *AIChE J.* **58**, 2885–2899 (2012).
 77. Seki, S. *et al.* Comprehensive refractive index property for room-temperature ionic liquids. *J. Chem. Eng. Data* **57**, 2211–2216 (2012).
 78. Nuvoli, D. *et al.* High concentration few-layer graphene sheets obtained by liquid phase exfoliation of graphite in ionic liquid. *J. Mater. Chem.* **21**, 3428–3431 (2011).
 79. Zhang, B. *et al.* Stable dispersions of reduced graphene oxide in ionic liquids. *J. Mater. Chem.* **20**, 5401 (2010).
 80. Zhou, X. *et al.* Dispersion of graphene sheets in ionic liquid [bmim][PF6] stabilized by an ionic liquid polymer. *Chem. Commun. (Camb)*. **46**, 386–388 (2010).
 81. Zhao, Y. & Hu, Z. Graphene in Ionic Liquids: Collective van der Waals Interaction and Hindrance of Self-Assembly Pathway. *J. Phys. Chem. B* **117**, 10540–10547 (2013).
 82. Bari, R. *et al.* Direct exfoliation of graphene in ionic liquids with aromatic groups. *Colloids Surfaces A Physicochem. Eng. Asp.* **463**, 63–69 (2014).

4. Rheological Investigation of Few-Layer Graphene Production by Shear Exfoliation of Graphite

Abstract

Prior research into the liquid-phase exfoliation of graphite to produce few-layer graphene has focused primarily on the surface energy matching between graphite and solvent; however, the effect of other solvent properties, such as liquid viscosity, have not been systematically explored. In principle, a higher viscosity solvent should enable the production of graphene and other graphitic nanomaterials by liquid-phase exfoliation at lower shear rates than traditionally used organic solvents of low viscosity, such as N-methyl-2-pyrrolidone (NMP). Thus, at a given shear rate, more material should be exfoliated in the higher viscosity solvent. Hence, graphite suspensions in NMP, benzyl benzoate, and propylene glycol were exfoliated at various shear rates in a rheometer. Exfoliant concentrations were measured by ultraviolet-visual (UV-vis) spectroscopy and quality characterization was performed by Raman spectroscopy and scanning electron microscopy (SEM). Graphite exfoliation in the more viscous propylene glycol solvent resulted in a higher exfoliant concentration than in the less viscous NMP and benzyl benzoate solvents across all shear rates. Benzyl benzoate lowered exfoliant levels, likely due to a poor surface energy match, resulting in particle attraction and aggregation. Characterization showed that at least some of our material is few-layer graphene.

This chapter is adapted from the published article “The Effect of Solvent Viscosity on Production of Few-layer Graphene from Liquid-phase Exfoliation of Graphite” by Matthew A. Diasio and David L. Green, MRS Advances, 241-247 (2019).

4.1 Introduction

Graphene has caught the attention of scientists and engineers across fields because of its many impressive properties, especially its high mechanical strength and useful electronic properties^{1,2}. The inherent high surface area and specific volume of a two-dimensional material make graphene effective at the absorption of species for removal, or combined with the sensitivity of graphene's electronic properties to adsorbed molecules, make it a promising sensor^{3,4}. Graphene can also be used as a selective filter or impermeable barrier for liquids and/or gases depending on how it is processed, with applications ranging from water desalination to food packaging^{3,5,6}. There is also interest in modified graphene or graphene-based composites to break down pollutants^{3,7}.

Graphene can be produced in many different ways, with both bottom-up and top-down techniques being cost-effective depending on the desired application⁸. One of the most promising techniques for large-scale manufacture of few-layer graphene (FLG) is liquid-phase exfoliation of graphite. Much work on liquid-phase exfoliation has focused on sonication, where shock waves from collapsing cavitation bubbles provide the mechanical force⁹. However, sonication is hard to scale up^{10,11}, and graphene produced through sonication has a significant defect concentration. These defects are attributed to the extreme conditions of cavitation, such as high local temperatures and pressures, which can cause localized chemical modification of the graphene^{9,12}.

The disadvantages of sonication-assisted exfoliation have led to an interest in processes that primarily shear graphene layers off of each other instead. 10-20 times less energy is required to separate layers in graphite by sliding than by changing the interlayer distance¹⁰. In 2014, Paton et al., showed that it is possible to directly produce few-layer graphene flakes from graphite by applying a high rate of shear to both organic and aqueous suspensions of graphite¹³. The

graphene produced does not have significantly more defects than the graphite precursor, with the exception of edge defects attributable to the smaller size of the graphene flakes. This method is scalable to larger set-ups, which is promising for manufacturing. While the initial work used a high-shear rotor/stator mixer, it has also been found that turbulent flow in conventional blenders can provide the requisite shear for graphene exfoliation¹³⁻¹⁵. In the liquid-phase exfoliation literature, the choice of effective solvents for graphene is often based on finding liquids with a surface tension (or energy) close to that of graphite, minimizing the energy needed to form new liquid-graphene interfaces^{13,16,17}. This has been considered a “blunt tool”¹⁸ and while surface tension may be useful for choosing exfoliation liquids, it does not adequately predict dispersal behavior¹⁹.

Almost no prior research has been performed to study the effect of viscosity on the exfoliation of graphite. If viscosity is studied, it is often to analyze rheological behavior²⁰⁻²². Dong et al. discuss the importance of the suspension’s viscosity²³, but do not discuss that of the liquid itself. Most of the organic solvents used in prior exfoliation studies have viscosities on the order of 1 mPa·s, limiting the ability to study the role of the liquid’s intrinsic viscosity. Given that greater viscosity reduces the intensity of cavitation, viscous solvents may have been ineffective in studies of exfoliation by sonication and were excluded from further consideration. As research focuses more on exfoliation by shear, the role of liquid viscosity becomes more important to consider and the use of viscous solvents must be reevaluated. While the graphite/graphene particles add to the viscosity and increase the energy needed to deform the suspension, the particles do not transmit shear stresses beyond themselves while the continuous medium of the liquid does. Higher viscosity liquids more efficiently transfer shear between

adjacent regions, and we hypothesize this could improve the exfoliation of graphene layers from a precursor piece of graphite.

4.2 Methods

4.2.1 Materials

The precursor graphite material was Alfa Aesar natural graphite flakes, 99.8% purity (metal basis), -325 mesh size. Exfoliation solvents were NMP (Alfa Aesar, 99+%), propylene glycol (PG, Alfa Aesar, 99.5% min), and benzyl benzoate (BB, Alfa Aesar, 99+%). NMP is generally regarded as the best solvent for graphene exfoliation and dispersion and is chosen as a standard¹¹. PG and BB were chosen because they have significantly higher viscosities of 40.4 and 8.3 mPa·s., respectively²⁴, than common graphene and nanotube solvents such as NMP, which has a viscosity of 1.7 mPa·s²⁵, but a similar surface tension to NMP^{26,27}. These properties are summarized in Table 4.1 This enables a study focusing almost entirely on viscosity effects.

Table 4.1. Relevant physical properties of chosen liquids for graphene dispersions

Liquid	Surface tension (mN/m)	Viscosity	Dielectric constant
N-Methyl-2-pyrrolidone (NMP)	40	1.7 cP	33
Benzyl benzoate (BB)	43	8.3 cP	5
Propylene glycol (PG)	40	44 cP	27.5

4.2.2 Exfoliation

Exfoliations were performed in an Anton Paar MCR 301 rheometer using a concentric cylinder geometry with a gap of 0.1 mm at a controlled temperature of 25 C. The suspensions for exfoliation were 50 g/L graphite in the solvent, vigorously shaken for a minute before pouring into the cylinder. Exfoliation experiments began with a pre-shear step of 6 minutes at 600 s⁻¹ and the exfoliation step was for 1-4 hours at a variety of shear rates. This set-up was chosen to enable exfoliation at several shear rates above and below the critical shear rate of 10,000 s⁻¹ needed for exfoliation in NMP¹³, with times chosen to maximize the amount of material for

characterization. After exfoliation, the suspensions were centrifuged for 1 hour at 2500 rpm and decanted, performed twice, to separate the supernatant dispersion of exfoliated material from a pellet of unexfoliated material.

4.2.3 Characterization

Ultraviolet-visual (UV-vis) spectroscopy was performed in the 400-800 nm wavelength region to estimate material concentration in the dispersions after exfoliation. Absorbance at the 660 nm wavelength was used for the comparison following common practice in the literature. Spectra were acquired using a Shimadzu UV-2450 spectrometer with a 10 mm path length. Approximately 3 mL of dispersion was pipetted into 10 mm square glass cuvettes (Fisher Scientific and Science Outlet) for analysis. Spectra were taken with a baseline subtraction using pure solvent in another cuvette in a reference beam path. For quality characterization, supernatant dispersions were drop cast on heated silicon (for microscopy) and silica (for Raman) wafers (University Wafer) to evaporate off solvent. Raman spectroscopy was performed using a Renishaw inVia Raman microscope using a 200 mW 514 nm laser and 1800/cm grating. Scanning electron microscopy (SEM) was performed on an FEI Quanta 650 microscope at 10 or 5 kV accelerating voltage in secondary electron imaging mode.

4.3 Results

4.3.1 UV-Visual spectroscopy

Figure 4-1 shows the absorbance of suspensions exfoliated for 1 hour, measured within 18-24 hours of exfoliation. Based on the literature, the absorbance at 660 nm was chosen for comparison. Two solvents, NMP and PG, show increasing absorbance, and presumable exfoliated material, with increasing shear rate, suggesting that more material is exfoliated under higher shear as expected. BB shows lower absorbance and doesn't show an increasing trend in exfoliated concentration with increasing shear rate, which should hold true for all exfoliation

media. This variance in absorbance in BB within 24 hours suggest it is a poor dispersant on hours-long timescales and graphene platelets may be aggregating back into graphite. BB has a significantly lower dielectric constant than NMP or PG and also that of graphite. This may cause instability in graphene dispersions in BB, as the large difference in dielectric allows for significant interparticle interactions through the solvent, driving aggregation (see the discussion of relative polarizability and Eq. 3.13 in chapter 3)²⁸. PG shows a higher amount of material at all shear rates compared to NMP. As PG is significantly more viscous than NMP, Newton's equation of viscosity predicts that a higher viscosity liquid imparts greater stress at the particle interface, resulting in an increased concentration of exfoliated material (for stable dispersions).

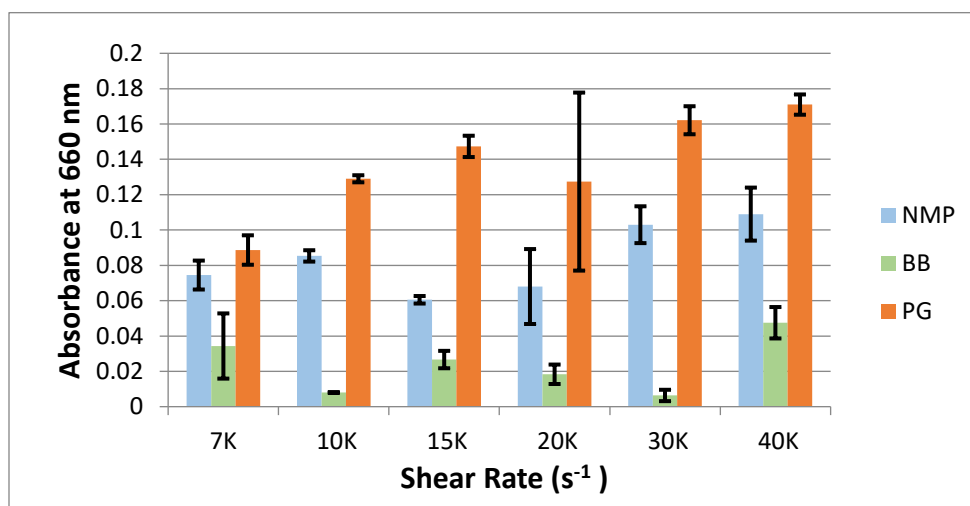


Figure 4-1. Absorbance of exfoliated suspensions within 24 hours of exfoliation. The error bars represent standard deviation across multiple measured aliquots ($n=3$).

Additionally, we studied the stability of the suspensions in NMP and PG by measuring the absorbance over time. BB was removed from further consideration due to its poor performance during the spectroscopy measurements. NMP is well-known for its relative long-term stability in dispersing graphene and carbon nanotubes^{11,29}. The absorbance was observed over the course of 100 hours in one NMP and one PG sample that had both been exfoliated at

30,000 s⁻¹. This is shown in Figure 4-2. Both solvents show very little decrease in absorbance over the 100-hour period, suggesting both NMP and PG are capable of stably dispersing graphene. The higher level of UV absorbance in PG is indicative of the effect of greater viscosity on increasing the exfoliant concentration.

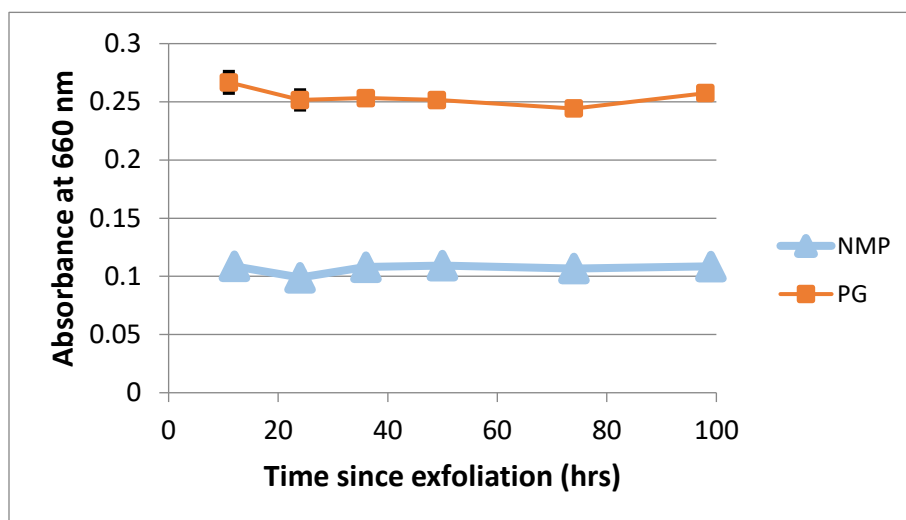


Figure 4-2. Absorbance of an NMP and PG exfoliated suspension for 100 hours after exfoliation.

4.3.2 Quality of Exfoliated Material

Figure 4-3 shows smoothed Raman spectra of the starting graphite and exfoliated material in PG (shear rate of 40,000 s⁻¹ for 4 hours), normalized to the highest intensity in each spectrum. Smoothing was done by taking the five-point moving average to reduce noise due to the low laser power needed to avoid sample damage. The 2D peak at ~2700 cm⁻¹ shows a less pronounced shoulder after shear and is higher relative to the G peak at ~1600 cm⁻¹, which are signs of more graphene-like character³⁰. The 2D peak shape resembles those for FLG of 5 or fewer layers¹⁷. Figure 4-4 shows an SEM image of material identically sheared at 40,000 s⁻¹ for 4 hours in PG. Many flakes in the image show a high degree of transparency to secondary electrons from structures underneath, indicative of thickness on the order of nanometers³¹, and based on the Raman spectrum, are highly likely to be flakes of FLG.

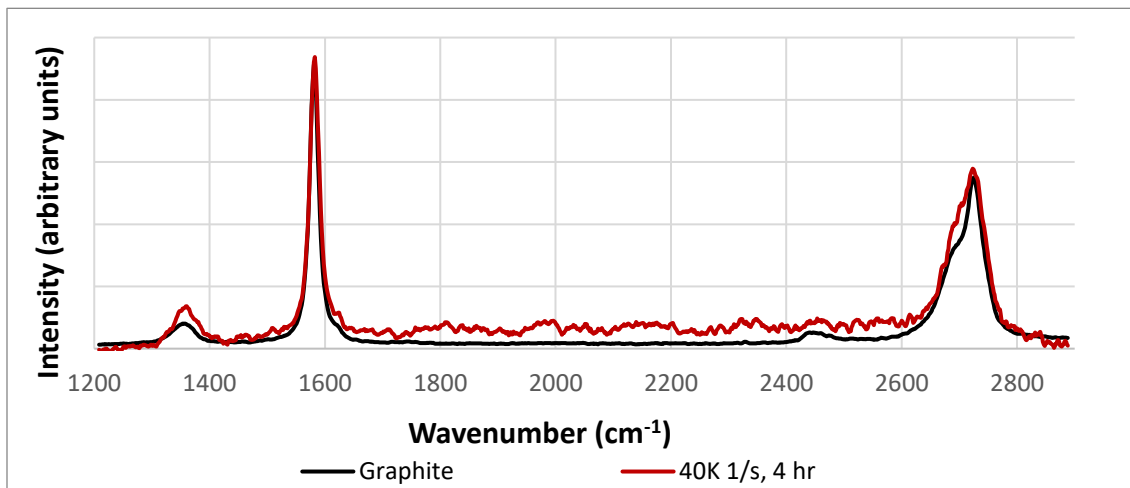


Figure 4-3. Raman spectra of starting graphite and shear exfoliated material in propylene glycol, normalized to the highest peak.

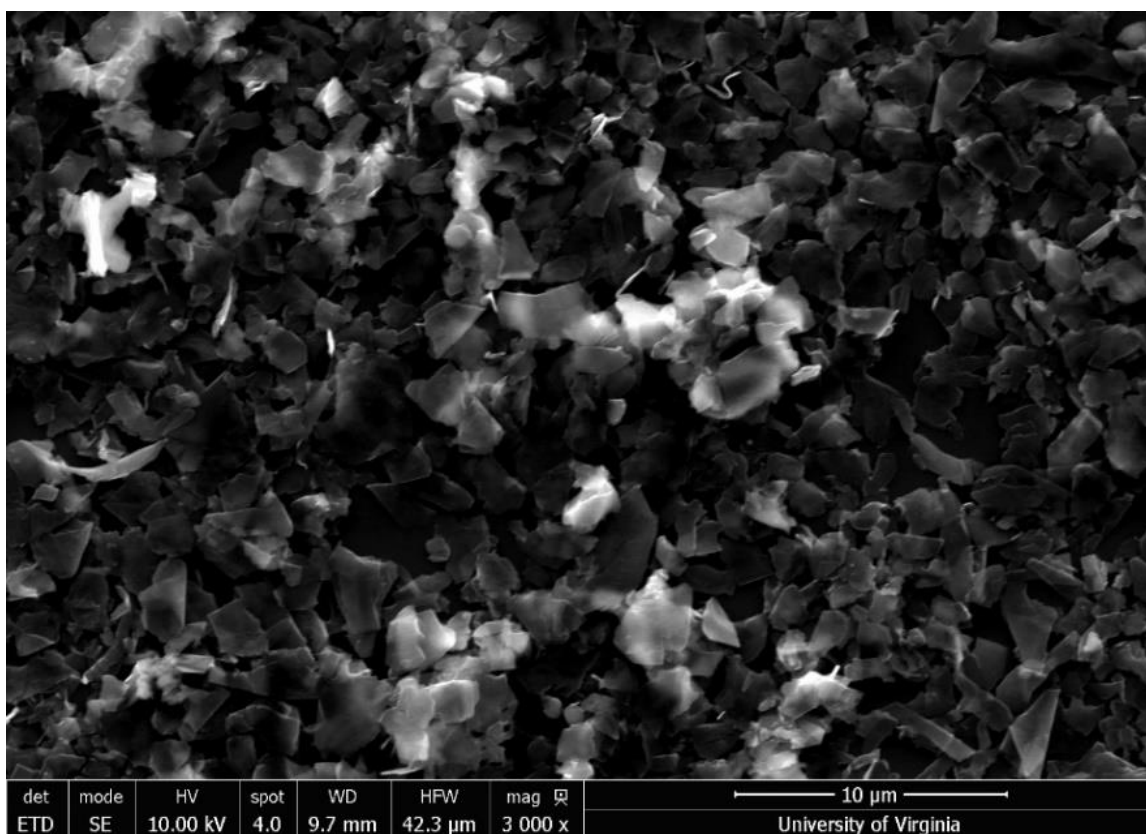


Figure 4-4. SEM image of sheared graphite. Many light flakes are electron transparent.

4.4 Conclusions

We have shown for the first time the products of liquid-phase shear exfoliation of graphite in propylene glycol. UV-vis spectroscopy shows that using a more viscous solvent increases exfoliation, among those that can stably disperse exfoliated material. Secondary

electron microscopy and Raman spectroscopy confirm that this sheared material includes FLG, showing that viscous solvents can also be used as exfoliation media for graphene production. The inconsistent performance of BB suggests the presence of particle attractions over that in NMP and PG.

4.5 Acknowledgements

This chapter is adapted from the published article “The Effect of Solvent Viscosity on Production of Few-layer Graphene from Liquid-phase Exfoliation of Graphite” by Matthew A. Diasio and David L. Green, *MRS Advances*, 241-247 (2019).

4.5 References for Chapter 4

1. Geim, A. K. & Novoselov, K. S. The rise of graphene. *Nat. Mater.* **6**, 183–191 (2007).
2. Lee, C., Wei, X., Kysar, J. W. & Hone, J. Measurement of the Elastic Properties and Intrinsic Strength of Monolayer Graphene. *Science* (80-.). **321**, 385–388 (2008).
3. Perreault, F., Fonseca de Faria, A. & Elimelech, M. Environmental applications of graphene-based nanomaterials. *Chem. Soc. Rev.* **44**, 5861–5896 (2015).
4. Choi, W., Lahiri, I., Seelaboyina, R. & Kang, Y. S. Synthesis of Graphene and Its Applications: A Review. *Crit. Rev. Solid State Mater. Sci.* **35**, 52–71 (2010).
5. Aghigh, A. *et al.* Recent advances in utilization of graphene for filtration and desalination of water: A review. *Desalination* **365**, 389–397 (2015).
6. Unalan, I., Cerri, G. & Marcuzzo, E. Nanocomposite films and coatings using inorganic nanobuilding blocks (NBB): current applications and future opportunities in the food packaging sector. *RSC Adv.* 29393–29428 (2014). doi:10.1039/c4ra01778a
7. Khurana, I., Saxena, A., Bharti, Khurana, J. M. & Rai, P. K. Removal of Dyes Using Graphene-Based Composites: a Review. *Water, Air, Soil Pollut.* **228**, 180 (2017).
8. Ferrari, A. C. *et al.* Science and technology roadmap for graphene, related two-dimensional crystals, and hybrid systems. *Nanoscale* **7**, 4598–4810 (2014).
9. Yi, M. & Shen, Z. A review on mechanical exfoliation for the scalable production of graphene. *J. Mater. Chem. A* **3**, 11700–11715 (2015).
10. Arao, Y., Mizuno, Y., Araki, K. & Kubouchi, M. Mass production of high-aspect-ratio few-layer-graphene by high-speed laminar flow. *Carbon N. Y.* **102**, 330–338 (2016).
11. Johnson, D. W., Dobson, B. P. & Coleman, K. S. A manufacturing perspective on

- graphene dispersions. *Curr. Opin. Colloid Interface Sci.* **20**, 367–382 (2015).
12. Bracamonte, M. V., Lacconi, G. I., Urreta, S. E. & Foa Torres, L. E. F. On the Nature of Defects in Liquid-Phase Exfoliated Graphene. *J. Phys. Chem. C* **118**, 15455–15459 (2014).
 13. Paton, K. R. *et al.* Scalable production of large quantities of defect-free few-layer graphene by shear exfoliation in liquids. *Nat. Mater.* **13**, 624–630 (2014).
 14. Varrla, E. *et al.* Turbulence-assisted shear exfoliation of graphene using household detergent and a kitchen blender. *Nanoscale* **6**, 11810–11819 (2014).
 15. Yi, M. & Shen, Z. Kitchen blender for producing high-quality few-layer graphene. *Carbon N. Y.* **78**, 622–626 (2014).
 16. Lyklema, J. The surface tension of pure liquids: Thermodynamic components and corresponding states. *Colloids Surfaces A Physicochem. Eng. Asp.* **156**, 413–421 (1999).
 17. Hernandez, Y. *et al.* High-yield production of graphene by liquid-phase exfoliation of graphite. *Nat. Nanotechnol.* **3**, 563–568 (2008).
 18. Hernandez, Y., Lotya, M., Rickard, D., Bergin, S. D. & Coleman, J. N. Measurement of Multicomponent Solubility Parameters for Graphene Facilitates Solvent Discovery. *Langmuir* **26**, 3208–3213 (2010).
 19. Shen, J. *et al.* Liquid Phase Exfoliation of Two-Dimensional Materials by Directly Probing and Matching Surface Tension Components. *Nano Lett.* **15**, 5449–5454 (2015).
 20. Zhang, B. *et al.* Stable dispersions of reduced graphene oxide in ionic liquids. *J. Mater. Chem.* **20**, 5401 (2010).
 21. Naficy, S. *et al.* Graphene oxide dispersions: tuning rheology to enable fabrication. *Mater. Horizons* **1**, 326 (2014).
 22. Barwich, S., Coleman, J. N. & Möbius, M. E. Yielding and flow of highly concentrated, few-layer graphene suspensions. *Soft Matter* **11**, 3159–3164 (2015).
 23. Dong, L. *et al.* A non-dispersion strategy for large-scale production of ultra-high concentration graphene slurries in water. *Nat. Commun.* **9**, 1–8 (2018).
 24. Viscosity of Liquids as a Function of Temperature. in *CRC Handbook of Chemistry and Physics* (eds. Rumble, John R., J., Bruno, T. J., Martinsen, D. & Lide, D. R.) (CRC Press, 2018).
 25. Henni, A., Hromek, J. J., Tontiwachwuthikul, P. & Chakma, A. Volumetric Properties and Viscosities for Aqueous N -Methyl-2-pyrrolidone Solutions from 25 °C to 70 °C. *J. Chem. Eng. Data* **49**, 231–234 (2004).

26. Yaws, C. L. & Richmond, P. C. Surface tension—Organic compounds. in *Thermophysical Properties of Chemicals and Hydrocarbons* 686–781 (Elsevier, 2009). doi:10.1016/B978-081551596-8.50026-2
27. Surface Tension of Common Liquids. in *CRC Handbook of Chemistry and Physics* (eds. Rumble, John R., J., Bruno, T. J., Martinsen, D. & Lide, D. R.) (CRC Press, 2018).
28. Israelachvili, J. Interactions Involving the Polarization of Molecules. in *Intermolecular and Surface Forces* 67–82 (Academic Press, 1992).
29. Hamilton, C. E., Lomeda, J. R., Sun, Z., Tour, J. M. & Barron, A. R. High-Yield Organic Dispersions of Unfunctionalized Graphene. *Nano Lett.* **9**, 3460–3462 (2009).
30. Paton, K. R. *et al.* Scalable production of large quantities of defect-free few-layer graphene by shear exfoliation in liquids. *Nat. Mater.* **13**, 624–630 (2014).
31. Seiler, H. Secondary electron emission in the scanning electron microscope. *J. Appl. Phys.* **54**, R1–R18 (1983).

5. Producing Few-Layer Graphene by Shear Exfoliation in a Viscous Liquid in a Large-Scale Mixer

Abstract

Our previous work has demonstrated production of few-layer graphene by shear exfoliation of graphite in a viscous liquid and that in Taylor-Couette flow, higher viscosity liquids can produce a higher concentration of few-layer graphene (FLG) than lower viscosity liquids at the same shear rate. Thus, by selecting liquids with higher viscosities, manufacturer could improve the yield of FLG they produce from exfoliation. Many studies in the literature suggest that turbulence is beneficial or necessary for large-scale exfoliation, depending on the mixing geometry and specific mechanisms involved in flake break-up. Thus, we investigate shear exfoliation in a viscous liquid, propylene glycol (PG), in comparison to the standard graphene solvent N-methyl-2-pyrrolidone (NMP) in an industrial impeller mixer. Through an analysis of the dispersion turbidity with ultraviolet-visual (UV-vis), spectroscopy, we calculate the second virial coefficient of FLG in both solvents as an estimate of thermodynamic stability and find that PG is more stable against aggregation. Additionally, though UV-vis spectroscopy, we show that PG exfoliates more material than NMP for all given exfoliation times, and Raman spectroscopy and transmission electron microscopy show that the FLG produced in PG is of similar quality to that produced in NMP. Thus, we demonstrate that PG and potentially other viscous solvents could be practical and efficient media for the production of FLG by liquid-phase exfoliation.

5.1 Introduction

The previous work demonstrated the ability of a viscous liquid, propylene glycol (PG), to produce few-layer graphene (FLG) by the shear exfoliation of graphite in the controlled flow

conditions of a rheometer. Additionally, dispersions produced in PG had a higher absorbance than dispersions produced at identical shear rates in N-methyl-2-pyrrolidone (NMP), the most commonly used graphene solvent, suggesting that the concentration of FLG produced is greater in PG than NMP. This is attributed to the higher viscosity of PG, which is $40.4 \text{ mPa}\cdot\text{s}^1$, than NMP, which is $1.66 \text{ mPa}\cdot\text{s}^2$, while both solvents have similar surface tensions^{3,4}. PG's higher viscosity enables it to more efficiently transfer shear forces to the graphite flakes, augmenting the exfoliation process.

However, the Taylor-Couette flow in the rheometer's concentric cylinder geometry may be significantly different from flow regimes found in the larger impeller mixers/blenders typically used in manufacturing, especially the development of turbulence. While Paton *et al.* showed that turbulence is not required for FLG production from liquid-phase shear exfoliation of pristine graphite⁵, that study as well as others suggest that turbulence may be beneficial to large-scale exfoliation⁶⁻⁸ in impeller mixers. Another study of Taylor-Couette flow showed exfoliation happening only in the turbulent regime⁹ and a recent study on tube-shear exfoliation showed laminar shear was insufficient to exfoliate graphite within the tube¹⁰. Arao *et al.* demonstrate FLG production by shear exfoliation in laminar flow conditions in a pressure homogenizer¹¹.

We estimate Reynolds (Re) numbers of ~ 280 for NMP and ~ 12 for PG at the highest shear rate in the concentric cylinder geometry, which corresponds to 3000 RPM. For the PG, this is well below any reported onset of turbulent flow, and the NMP flow is in a mixed regime far from fully developed turbulence¹². In a common shear mixer system at 3000 RPM, however, NMP has a Re $\sim 30,000$, well above the Re = 10,000 characteristic of fully developed turbulence, while PG is estimated to have Re ~ 1300 , which would be in the lower end of the mixed regime^{6,13,14}. The variance in FLG yield and morphology from these various flow systems

suggests that their different flow characteristics may affect the mechanisms of exfoliation within each system. Thus, investigating if results can be applied between systems may still be needed. Determining if the relationship between higher viscosity and increased FLG concentration holds outside of Taylor-Couette flow, in an impeller mixer designed for industrial scale-up is important for practical application of the rheological analysis.

Furthermore, given the surface tension literature's inability to predict dispersion stability in solvents¹⁵, there is a need for more detailed study of the stability of FLG dispersions, especially with a new solvent like PG. Through turbidimetry, it is possible to study particle interactions even in concentrated systems showing multiple scattering¹⁶. As many works on FLG dispersions produced by liquid-phase exfoliation already use ultraviolet-visual spectroscopy to measure concentration based on absorbance, it is easy to apply this analysis to FLG in new solvents. Concentrated FLG dispersions need to be stable over at least days-long timescales to allow for processing, and longer timescales to allow for storage.

5.2 Methods

5.2.1 Exfoliation

The precursor graphite material was Alfa Aesar natural graphite flakes, 99.8% purity (metal basis), -325 mesh size. Exfoliation solvents were NMP (Alfa Aesar, 99+%) and propylene glycol (Alfa Aesar, 99.5% min). Suspensions for exfoliation were 50 g/L graphite in the given solvents. Exfoliations were performed in a Silverson L5 rotor-stator mixer using a high shear screen as the workhead. Exfoliation samples were 120-140 mL of graphite suspension in a 200 mL beaker, with the mixer head centered. All exfoliations were run at 3000 RPM for times ranging from 10 minutes to 24 hours. After exfoliation, the suspensions were centrifuged for 1 hour at 2500 rpm and decanted, performed twice, to separate the supernatant dispersion of exfoliated material from a pellet of unexfoliated material.

5.2.2 Ultraviolet-Visual Spectroscopy

Ultraviolet-visual (UV-vis) spectroscopy was performed in the 400-800 nm wavelength region at 1 nm intervals. Spectra were acquired using a Shimadzu UV-2450 spectrometer with a 10 mm path length. Approximately 3 mL of dispersion was pipetted into 10 mm square quartz cuvettes (Fisher Scientific, Thor Labs) for analysis. Spectra were taken with a baseline subtraction using pure solvent in another cuvette in a reference beam path. Many samples showed a slight and steady decrease in absorbance in the first few minutes after preparation. This is attributed to the initial pipetting forming microbubbles in the suspension that scatter the beam until they dissipate, so analyzed spectra are only those where the sample has finished “bubble settling” and spectra do not show short-term changes on the scale of minutes.

5.2.2.1 Absorbance

To calibrate absorbance to concentration, some exfoliation samples were divided into two aliquots. One aliquot was filtered through a Nylon membrane with 0.22 μm pores (GVS Life Sciences) and the remaining material massed to determine concentration. The second aliquot was serially diluted through addition of the given solvent to determine the relationship between absorbance and graphene concentration in each solvent. In the dilute regime, absorbance is related to concentration by the Beer-Lambert law

$$A_{op} = \alpha Cl \quad (\text{Eq. 5.1})$$

where A_{op} is the optical absorbance, α is the absorption coefficient, C is the scatterer (FLG) concentration, and l is the optical path length.

5.2.2.2 Turbidimetry Analysis

Following the turbidity analysis of Apfel¹⁷ and Dutta¹⁸, we can determine the relationship between concentration and absorbance (as turbidity) outside the Beer-Lambert regime as well as determine the osmotic compressibility. Turbidity τ is related to absorbance A_{op} by

$$\tau = (A_{op} \ln 10)/l \quad (\text{Eq. 5.2})$$

where l is the optical path length. Transforming the equations of Apfel and Dutta, we find the relationship between turbidity and concentration C to be

$$\tau(\lambda^2, C) = C\alpha Q(\lambda^2, C)Z(\lambda^2, C) \quad (\text{Eq. 5.3})$$

where α is the absorption coefficient and $Q(\lambda^2, C)$ represents the integrated form factor and $Z(\lambda^2, C)$ represents the integrated structure factor of the scattering particles as a function of concentration and wavelength λ . For a given wavelength, Z is linear with C , so τ is quadratic. By interpolating the fit, we can determine the concentration of a dispersion in the concentrated and multiple scattering regimes.

Furthermore, it is possible to estimate the second virial coefficient of FLG in both solvents, which provides information on the interactions between dispersed particles, through calculation of the dimensionless osmotic compressibility¹⁶⁻¹⁸. In the dilute limit ($c \rightarrow 0$), Z approaches one as interparticle interactions become negligible. Thus,

$$\left(\frac{\tau}{C}\right)_{C=0} = \alpha Q(\lambda^2) \quad (\text{Eq. 5.4})$$

and $\alpha Q(\lambda^2)$ is found by extrapolating the y-intercept of the line fitting τ/C at each wavelength.

Then Z at a specific wavelength can be found by

$$Z(\lambda^2, C) = \frac{\tau/C}{(\tau/C)_{C=0}} \quad (\text{Eq. 5.5})$$

$Z(\lambda^2, C)$ can be broken down into

$$Z(\lambda^2, C) = S(0, C) + 8F \left(\frac{n\pi}{\lambda}\right)^2 + O\left(\frac{1}{\lambda}\right)^4 \quad (\text{Eq 5.6})$$

where $S(0, C)$ is the structure factor at vanishing scattering angle, and F is a coefficient related to the geometry of the photodetector's closure, n is the refractive index of the dispersing medium, and the $O(1/\lambda)^4$ term represents higher-order errors in the small scattering angle approximation.

In the infinite wavelength limit (which can be reached in the near-infrared range for small

particles), $S(0,C)$ is therefore equivalent to $Z(\lambda^2,C)$ and is found by taking the intercept of the linear fit of $Z(\lambda^2,C)$ plotted against $1/\lambda^2$. The inverse of $S(0,C)$ is the osmotic compressibility¹⁹, which can be written in the virial expansion as

$$S(0,C)^{-1} = 1 + 2B_2C + O(c^2) = Z(0,C)^{-1} \quad (\text{Eq. 5.7})$$

where B_2 is the second virial coefficient and the $O(c^2)$ term represents higher-order terms in the virial expansion. Thus, the second virial coefficient can be found as half the slope of the linear fit of the inverse of $S(0,C)$ against concentration.

5.2.3 Morphology Characterization

Characterization of the resulting FLG morphology was obtained through Raman spectroscopy and transmission electron microscopy (TEM). Raman samples were prepared by drop-casting exfoliated dispersions on heated silica wafers (University Wafer) to evaporate off solvent. TEM samples were prepared by drop-casting exfoliated dispersions onto holey carbon and lacey carbon films on 200 mesh Cu or Ni TEM grids (Ted Pella). The grids were heated at 40-80° C to evaporate the remaining solvent. Raman spectroscopy was performed using a Renishaw inVia Raman microscope using a 200 mW 514 nm laser and 1800/cm grating. Transmission electron microscopy was performed at 300 keV in an FEI Titan Transmission Electron Microscope.

5.3 Results

5.3.1 Ultraviolet-Visual Spectroscopy

Figure 5-1 shows the absorbance at 660 nm (divided by path length) against concentration of the serially diluted NMP and PG exfoliation samples (one sampled measured at each concentration). The absorbances for NMP appear to fit well with the Beer-Lambert law, and the estimated absorption coefficient for the exfoliated material dispersed in it is 2140 mL/(mg·m). This is close to other reported absorption coefficients for FLG in NMP in the literature, showing a relatively wide variance around 2460 mL/(mg·m)²⁰⁻²². However, PG is not well-described by the Beer-Lambert fit. This reflects that the Beer-Lambert law is only meant for the dilute regime, where scattering particles do not interact with each other and light is not multiply scattered^{17,23}. Given the difference in dielectric constant between NMP and PG, it is possible that FLG flakes may start to interact at different concentrations. In Figure 5-2, showing the turbidity, it is clear that PG shows nonlinear behavior and is better described by Eq. 5.3.

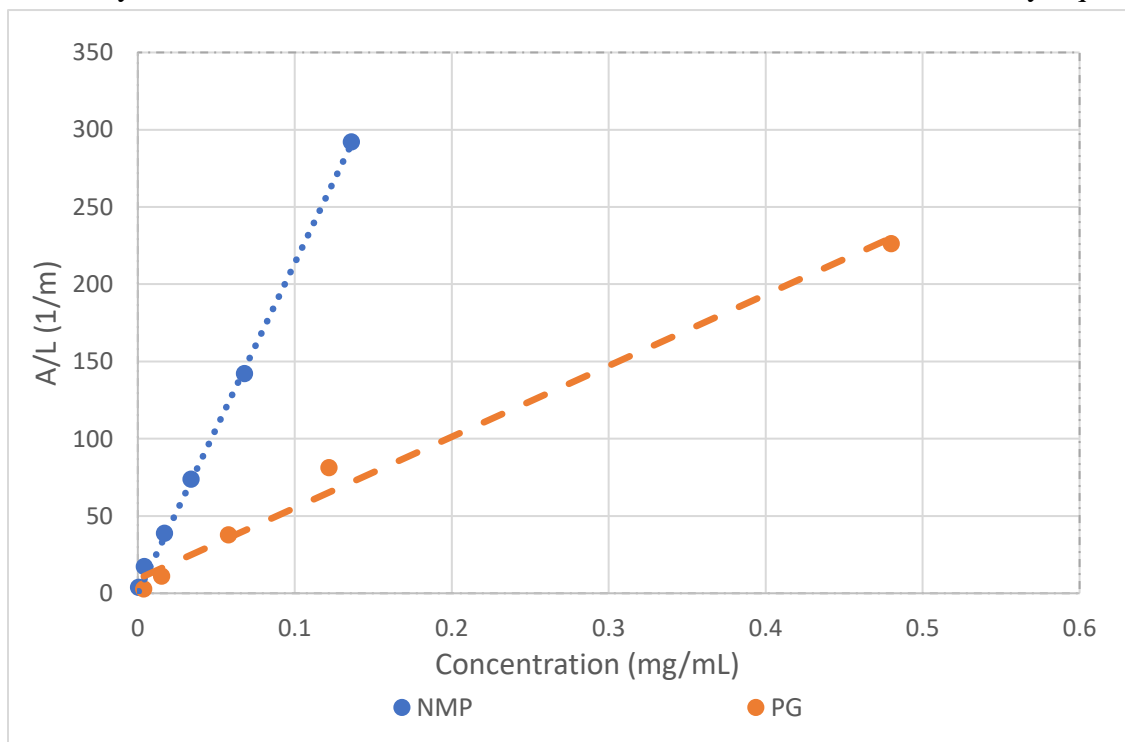


Figure 5-1. Absorbance at 660 nm divided by path length as a function of concentration for NMP and PG dispersions of known exfoliant concentration.

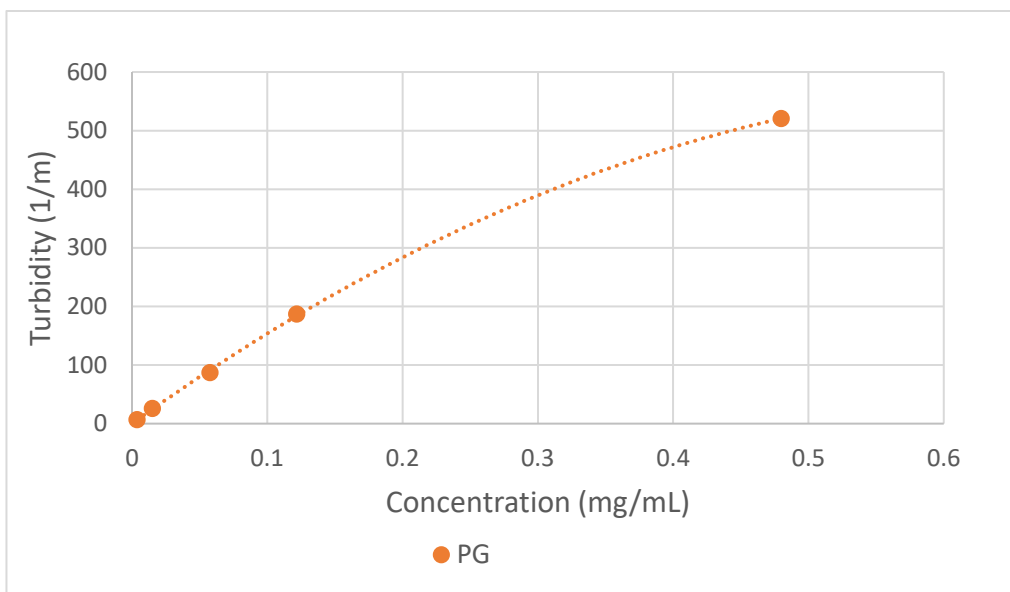


Figure 5-2. Turbidity at 660 nm as a function of concentration in PG.

Using this, absorbances from different exfoliation timepoints can be converted into estimated exfoliated FLG concentrations, given in Figure 5-3. At all time points, the exfoliated concentration in PG is higher than in NMP, continuing the trend shown in the rheometer. The estimated concentration achieved in PG of approximately 480 $\mu\text{g/mL}$ in 24 hours is believed to be one of the highest achieved by liquid-phase exfoliation in a simple organic solvent²⁴, as

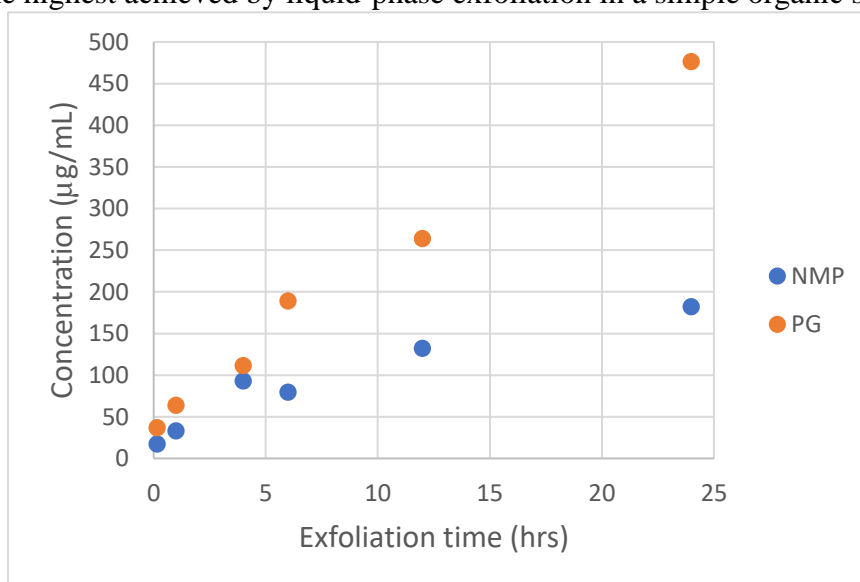


Figure 5-3. Exfoliated FLG concentration as a function of exfoliation time in both exfoliation solvents.

shown in Table 5.1. Additionally, the change in concentration over time after exfoliation was measured for two samples of exfoliated NMP and PG to determine the stability of these more concentrated (compared to the rheometer) dispersions, shown in Figure 5-4. NMP and PG both show little change over several days, and the change is attributed to settling of large flakes as agitation restores the measured concentration close to the original values (shown in NMP).

Table 5.1. High reported FLG concentrations from exfoliation studies in organic solvents

Exfoliation Medium	Method	Time (hr)	Concentration ($\mu\text{g/mL}$)	Reference
NMP	Impeller shear	1.6	100	Paton et al., 2014 ^{Ref 5}
NMP	Sonication	460	1200	Khan et al., 2010 ^{Ref 22}
NMP	Chaotic flow, then sonication	8 (sonication time)	430	Liu et al., 2015 ^{Ref 25}
Ortho-dichlorobenzene	Sonication	0.5	30	Hamilton et al., 2009 ^{Ref 26}
Acetone	Sonication	48	90	O'Neill et al., 2011 ^{Ref 27}
Chloroform			400	
Isopropanol			500	
NMP	Taylor-Couette shear	2	650	Tran et al., 2016 ^{Ref 9}
DMF	Impeller shear	8	220	Yi and Shen, 2014 ^{Ref 7}

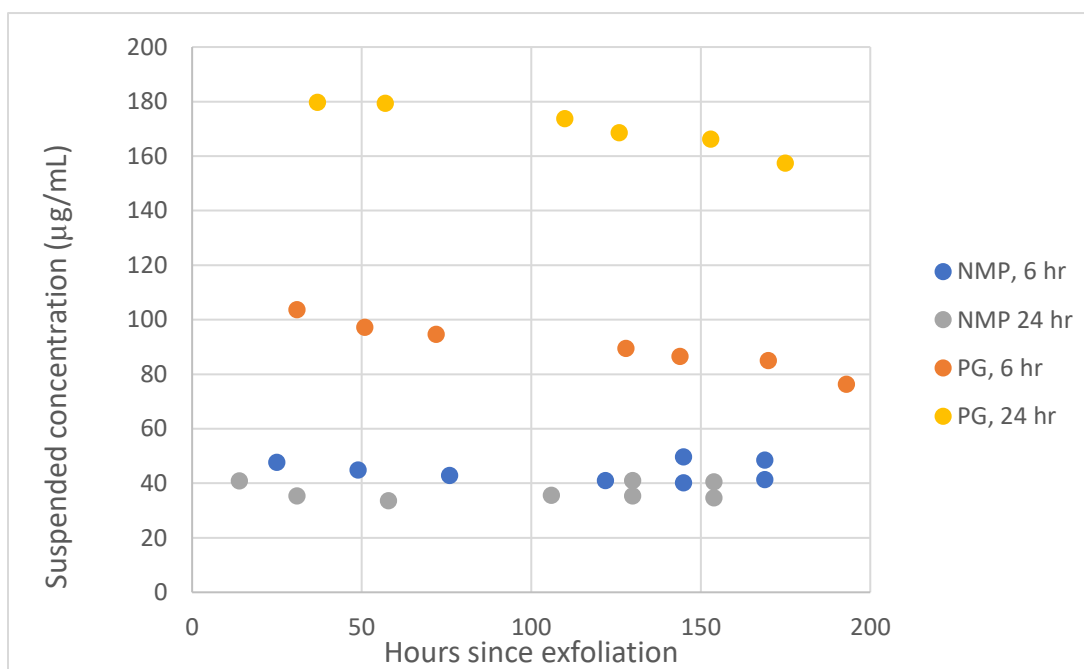


Figure 5-4. Change in suspension concentration over time in both solvents at different starting concentrations of exfoliated FLG.

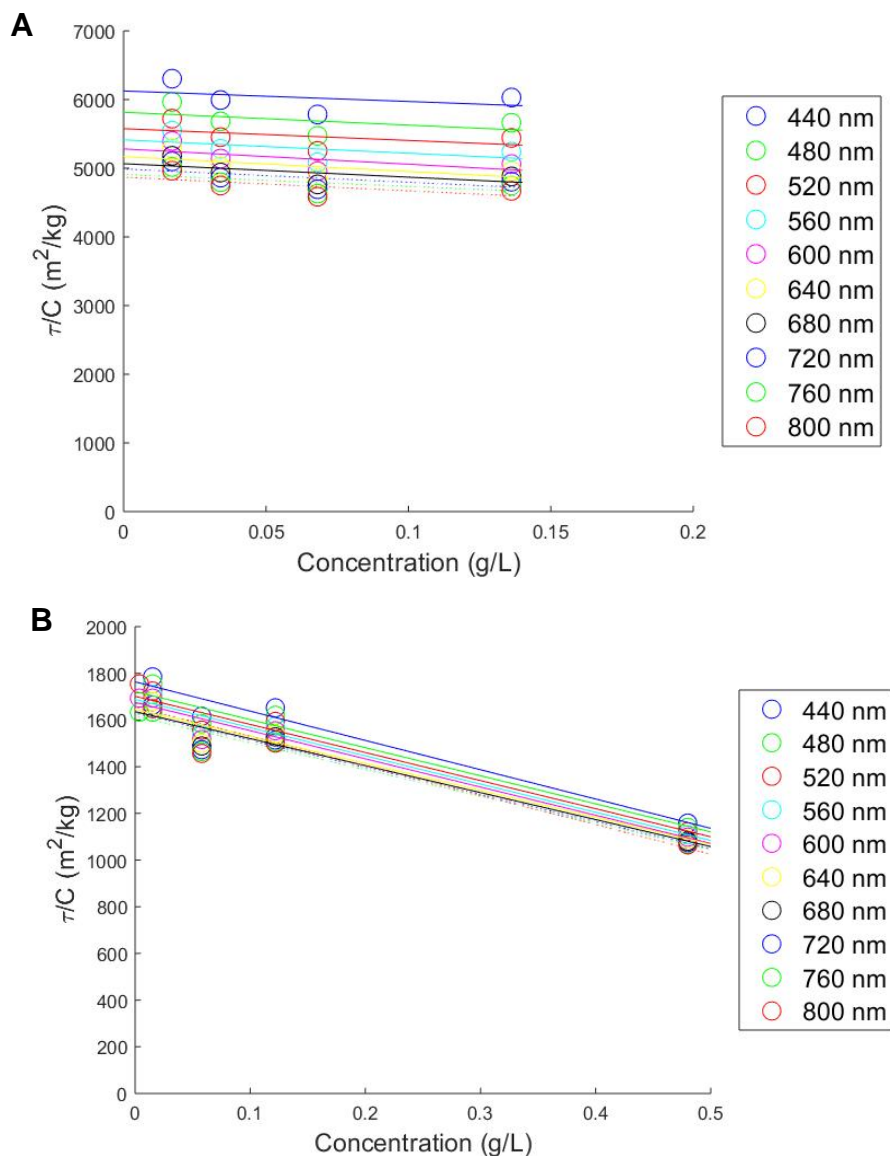


Figure 5-5. The specific turbidity of NMP (A) and PG (B) dispersions of FLG at selected wavelengths and the corresponding linear fits to find αQ .

Figures 5-5 and 5-6 show the steps represented by Eq. 5.4 and 5.5 in the turbidimetry analysis. The uncertainty in concentration increases with serial dilution, increasing error in the fitting, which is especially notable at the lower concentrations in NMP. Figure 5-7 shows the plot of the osmotic compressibility $S(0,C)^{-1}$ versus concentration for both solvents, and linear fits to find the second virial coefficient B_2 . We calculate that B_2 for FLG is $0.28 \text{ g/L} \pm 0.17$ in NMP and $0.55 \text{ g/L} \pm 0.06$ in PG. The positive sign of both values represents that pairwise interactions of

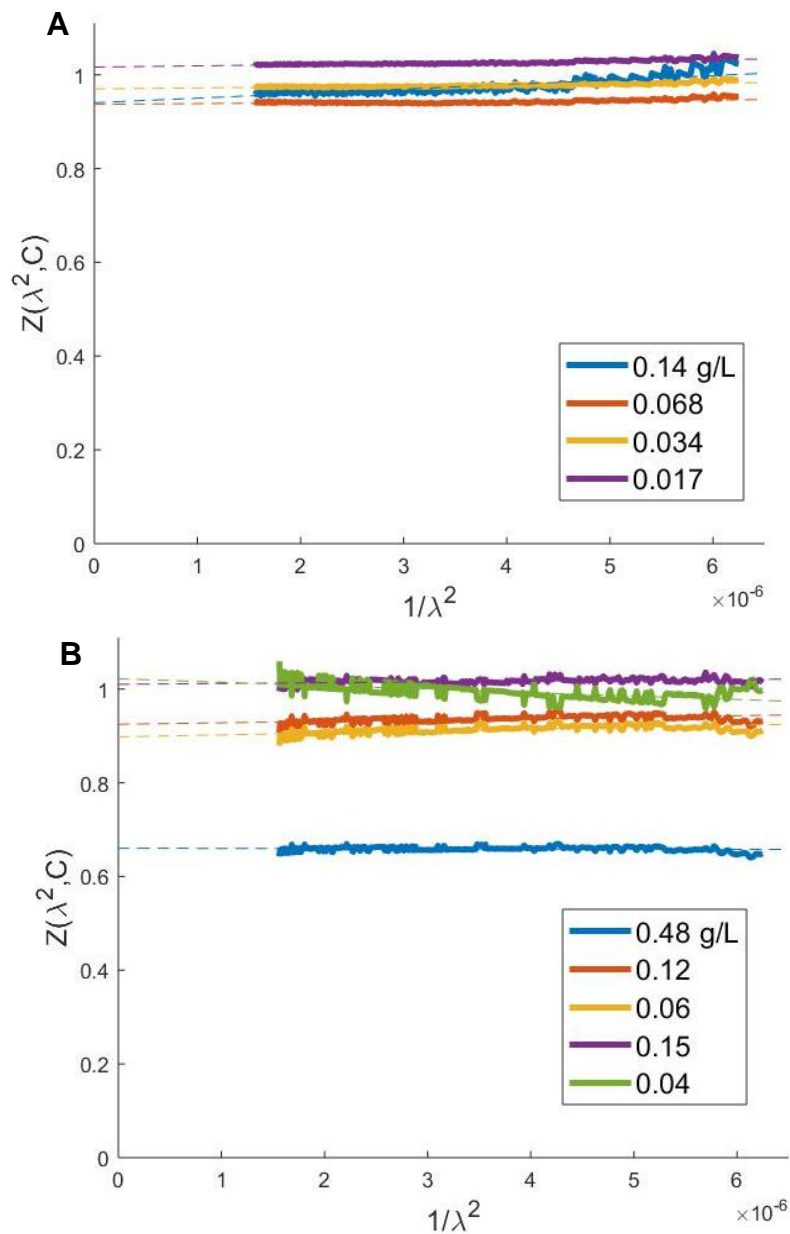


Figure 5-6. $Z(\lambda^2, C)$ plotted against $1/\lambda^2$ and the corresponding linear fits to find $S(0, C)$ in (A) NMP and (B) PG dispersions of FLG.

FLG are repulsive in both solvents. The relatively high error of NMP, due to the small number of concentrations probed, makes it difficult to compare relative stability, but if the values hold, PG's higher magnitude would suggest aggregation of flakes is less likely. This also fits with PG's dielectric constant being closer to graphene's than NMP's dielectric is, leading to a greater

reduction in interparticle attraction (see the discussion of relative polarizability in section 3.3 in chapter 3)²⁸.

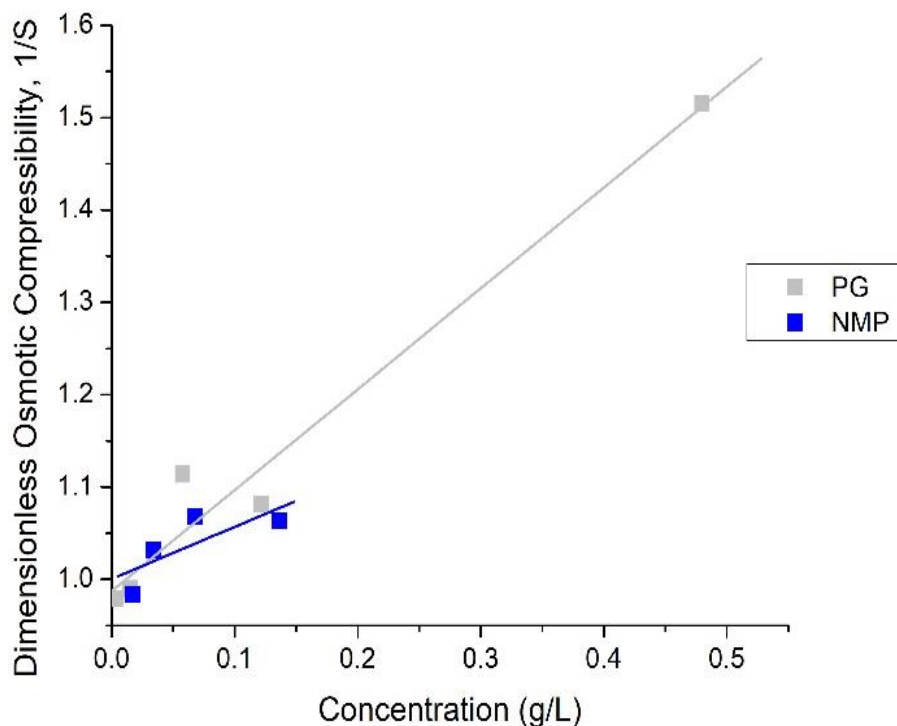


Figure 5-7. The osmotic compressibility, as $1/S(0,C)$, as a function of concentration in each solvent and the corresponding fits to find the second virial coefficient.

5.3.2 Morphology

Raman spectroscopy is commonly used to distinguish various carbon materials and is especially useful in evaluating the quality of graphitic materials like graphene and the fullerenes²⁹. Graphite has three main features in its Raman spectrum: (1) the D-band at ~ 1350 cm^{-1} , corresponding to defects, (2) the G-band at ~ 1580 cm^{-1} , which corresponds to in-plane stretching of C-C bonds, and (3) the 2D-band at ~ 2700 cm^{-1} , which is an overtone of the D-band. (Older literature may refer to the 2D peak as G', as it is the second most prominent peak in defect-free graphite³⁰. An alternate convention also uses X' to mark the first overtone of a given band X, so D' may refer to the 2D band. However, modern graphitic material research now uses

D' to describe a second defect-related peak at $\sim 1620\text{ cm}^{-1}$ that is a shoulder of the G peak at low defect concentrations and this paper uses that convention^{5,31,32}.)

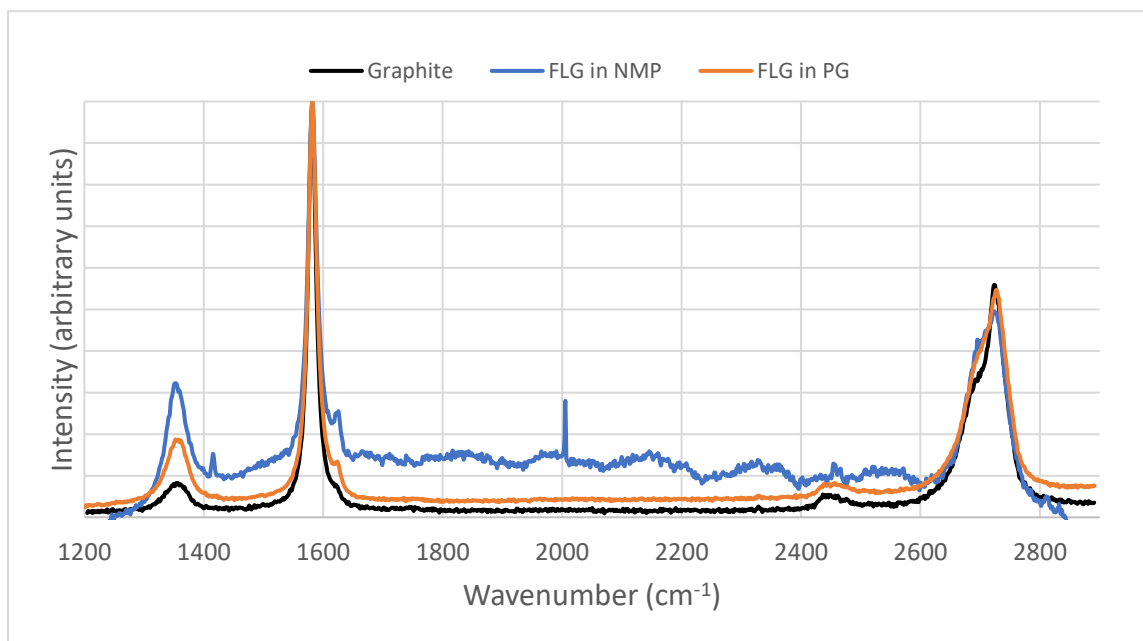


Figure 5-8. Normalized Raman spectra of a graphite standard compared to exfoliated material in NMP and PG.

Figure 5-8 shows normalized, average spectra taken from three different spots of mixer exfoliated material (6-hour exfoliation time) in NMP and PG, compared to pristine graphite. The NMP spectrum has also had a fluorescence baseline subtracted, believed to be caused by an interaction of NMP with the probe laser³³, which leads to a slight distortion of intensity values at the edge of the scanned range and also causes noise in the range between the G and 2D peaks. As expected, the D-band peak increases in both exfoliated materials, representing an increase in defect concentration. Given that the D'-band is still hard to distinguish from the G-band, however, the concentration should be relatively low. Additionally the low ratio of $I(D)/I(D')$ is suggestive of the defects primarily being edge defects due to the smaller lateral dimension of the FLG flakes compared to the precursor graphite^{31,34}. The intensity ratio for the D- and G-bands $I(D)/I(G)$ is ~ 0.16 for PG and ~ 0.30 for NMP, suggesting the material exfoliated in PG contains

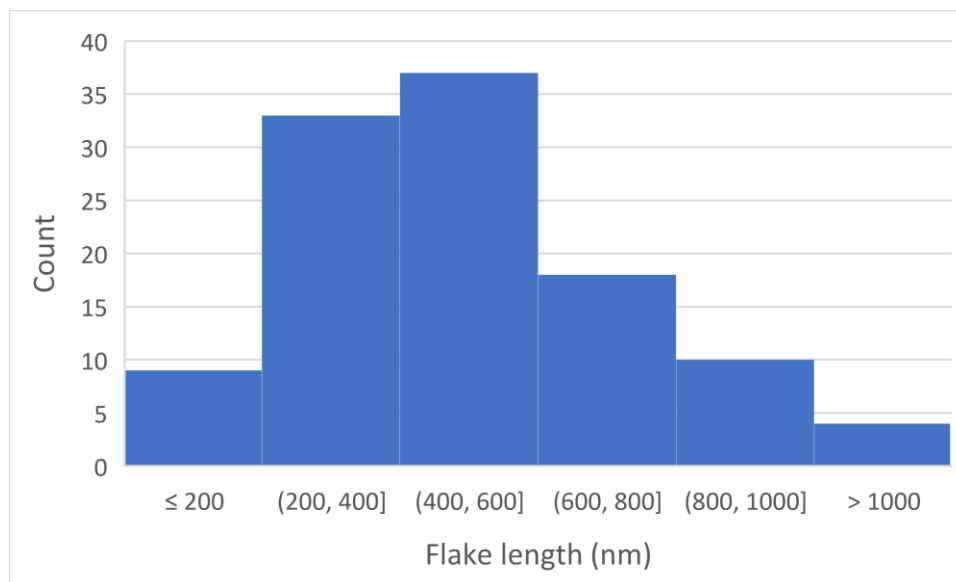


Figure 5-9. Histogram of FLG flake lengths exfoliated in PG.

fewer defects, though the fluorescence of NMP makes this an approximate comparison³². The 2D peak of both sets of exfoliated material is more Gaussian than that of the graphite, which is a sign of few-layer graphitic material (e.g. graphene)²⁰. Given the uncertainty caused by the fluorescence and the relative similarity of the peak shapes, it cannot currently be determined whether there is a difference in average thickness between the FLG produced by exfoliation in NMP or PG.

Transmission electron microscopy is often used to characterize the morphology of exfoliated nanomaterials. We are particularly interested in the lateral dimensions of exfoliated FLG flakes, which are important in determining possible applications of the material. TEM analysis was on flakes from material exfoliated for 24 hours to achieve high number concentrations. According to Paton, mean lateral flake size is independent of exfoliation time in a shear mixer¹², so this analysis should be applicable to nearly all practical time scales where exfoliation is observed. NMP had a tendency to disturb the carbon supports on the TEM grids, resulting in regions with no or minimal support and an insufficient number of FLG flakes were

counted for an independent length analysis. In PG, many flakes showed relatively large aspect ratio, so the reported length is the smaller of two bisecting lengths. The mean length observed in FLG flakes from PG is 500 nm (standard deviation 230 nm). FLG exfoliated in NMP in Paton's paper in an identical mixing set-up also had a mean length of 500 nm⁵. These lengths are lower than reported for FLG produced by sonication (mean length of 920 nm) and laminar shear in a homogenizer (mean length of 1410 nm)¹¹. A histogram of the observed lengths in PG is presented in Figure 5-9. However, observation of filtrates of the dispersions suggests there may be a difference in sampling. Figure 5-10 shows the filtrates obtained during gravimetry. The NMP filtrate is cloudy, while the PG is clear and closely resembles pristine PG. This suggests a nontrivial amount of exfoliated material in NMP is small enough to pass through the 0.22 μm pores in the filter, while almost all of the material in PG is larger than the pore size.

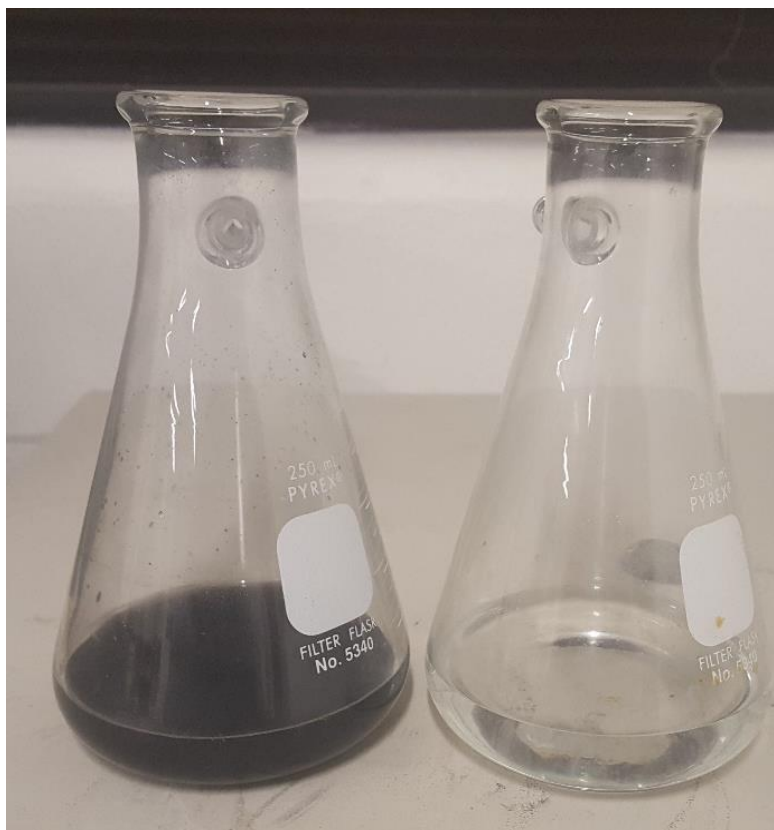


Figure 5-10. Filtrates of FLG dispersions. NMP is on the left, PG on the right.

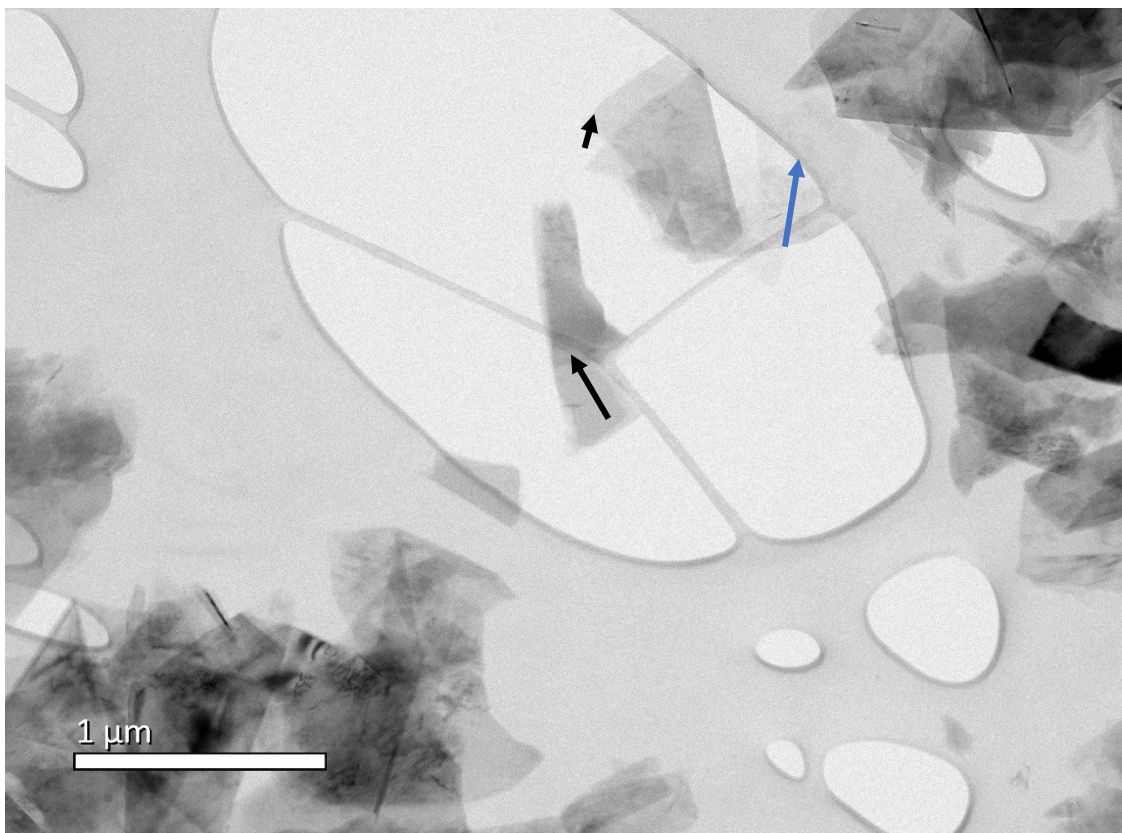


Figure 5-11. A representative TEM micrograph of FLG flakes in PG. Black arrows along the central flakes show suggested shearing layers. The blue arrow highlights a suspected monolayer flake.

Figure 5-11 shows a representative sample image of observed flakes. The two central flakes show layers that are displaced to each other, suggesting these are flakes that were still undergoing shear delamination, as has been reported in other papers^{5,7,11}. Many flakes also show wrinkling or folding, which is expected for freely-standing graphene, and could also occur as part of evaporating the solvent. Darker structures at the edge of the image are believed to be aggregates of flakes that formed as the solvent evaporated³⁵, as it is unlikely unexfoliated material was still dispersed after centrifugation. Electron opaque structures were excluded from the length analysis, because either aggregates or unexfoliated graphite would distort the data. At the right edge of the central hole is a flake that is believed to be monolayer graphene given its transparency and lack of visible internal edges.

5.4 Conclusions

In this chapter, we have demonstrated the production of few-layer graphene by liquid-phase shear exfoliation in a novel exfoliant, the viscous solvent propylene glycol, in an impeller mixer. Under identical mixing conditions, more FLG is produced in PG than the standard solvent, NMP, at all mixing times. The solutions show similar stability over the course of one week and both show positive second virial coefficients, suggesting PG should be at least as stable as NMP. Additionally, the FLG produced by exfoliation in PG is of similar quality to that produced in NMP, and may be longer when consider the sampling effect of the filter. Thus, we show that selecting more viscous solvents as the exfoliation medium is a practical way to achieve higher concentrations of high-quality FLG.

5.5 Acknowledgments

We wish to thank Dr. Chris Li (University of Virginia, Mechanical and Aerospace Engineering) for use of his laboratory's Silverson mixer for this project. We also wish to thank Dr. Li's postdoctoral associate, Dr. Zan Gao, for instruction on the mixer and for taking some of the TEM micrographs used in the length analysis. We would also like to thank research scientist Dr. Helge Heinrich (University of Virginia, Nanoscale Materials Characterization Facility) for obtaining the majority of the TEM micrographs used in the length analysis.

5.6 References for Chapter 5

1. Viscosity of Liquids as a Function of Temperature. in *CRC Handbook of Chemistry and Physics* (eds. Rumble, John R., J., Bruno, T. J., Martinsen, D. & Lide, D. R.) (CRC Press, 2018).
2. Henni, A., Hromek, J. J., Tontiwachwuthikul, P. & Chakma, A. Volumetric Properties and Viscosities for Aqueous N -Methyl-2-pyrrolidone Solutions from 25 °C to 70 °C. *J. Chem. Eng. Data* **49**, 231–234 (2004).
3. Yaws, C. L. & Richmond, P. C. Surface tension—Organic compounds. in *Thermophysical Properties of Chemicals and Hydrocarbons* 686–781 (Elsevier, 2009). doi:10.1016/B978-081551596-8.50026-2

4. Surface Tension of Common Liquids. in *CRC Handbook of Chemistry and Physics* (eds. Rumble, John R., J., Bruno, T. J., Martinsen, D. & Lide, D. R.) (CRC Press, 2018).
5. Paton, K. R. *et al.* Scalable production of large quantities of defect-free few-layer graphene by shear exfoliation in liquids. *Nat. Mater.* **13**, 624–630 (2014).
6. Varrla, E. *et al.* Turbulence-assisted shear exfoliation of graphene using household detergent and a kitchen blender. *Nanoscale* **6**, 11810–11819 (2014).
7. Yi, M. & Shen, Z. Kitchen blender for producing high-quality few-layer graphene. *Carbon N. Y.* **78**, 622–626 (2014).
8. Varrla, E. *et al.* Large-scale production of size-controlled MoS₂ nanosheets by shear exfoliation. *Chem. Mater.* **27**, 1129–1139 (2015).
9. Tran, T. S., Park, S. J., Yoo, S. S., Lee, T.-R. & Kim, T. High shear-induced exfoliation of graphite into high quality graphene by Taylor–Couette flow. *RSC Adv.* **6**, 12003–12008 (2016).
10. Blomquist, N. *et al.* Effects of geometry on large-scale tube-shear exfoliation of graphite to multilayer graphene and nanographite in water. *Sci. Rep.* **9**, 8966 (2019).
11. Arao, Y., Mizuno, Y., Araki, K. & Kubouchi, M. Mass production of high-aspect-ratio few-layer-graphene by high-speed laminar flow. *Carbon N. Y.* **102**, 330–338 (2016).
12. Paton, K. R. *et al.* SI for Scalable production of large quantities of defect-free few-layer graphene by shear exfoliation in liquids. *Nat. Mater.* **13**, 624–630 (2014).
13. Utomo, A. T., Baker, M. & Pacek, A. W. Flow pattern, periodicity and energy dissipation in a batch rotor-stator mixer. *Chem. Eng. Res. Des.* **86**, 1397–1409 (2008).
14. Dudukovic, M. Stirred Tanks. in 1–9 (2005).
15. Shen, J. *et al.* Liquid Phase Exfoliation of Two-Dimensional Materials by Directly Probing and Matching Surface Tension Components. *Nano Lett.* **15**, 5449–5454 (2015).
16. Tan, B. H., Tam, K. C., Lam, Y. C. & Tan, C. B. Osmotic compressibility of soft colloidal systems. *Langmuir* **21**, 4283–4290 (2005).
17. Apfel, U., Hoerner, K. D. & Ballauff, M. Precise Analysis of the Turbidity Spectra of a Concentrated Latex. *Langmuir* **11**, 3401–3407 (1995).
18. Dutta, N., Egorov, S. & Green, D. Quantification of Nanoparticle Interactions in Pure Solvents and a Concentrated PDMS Solution as a Function of Solvent Quality. *Langmuir* **29**, 9991–10000 (2013).
19. Jansen, J. W., de Kruif, C. G. & Vrij, A. Attractions in sterically stabilized silica dispersions. III. Second virial coefficient as a function of temperature, as measured by

- means of turbidity. *J. Colloid Interface Sci.* **114**, 492–500 (1986).
20. Hernandez, Y. *et al.* High-yield production of graphene by liquid-phase exfoliation of graphite. *Nat. Nanotechnol.* **3**, 563–568 (2008).
 21. Nuvoli, D. *et al.* High concentration few-layer graphene sheets obtained by liquid phase exfoliation of graphite in ionic liquid. *J. Mater. Chem.* **21**, 3428–3431 (2011).
 22. Khan, U., O’Neill, A., Lotya, M., De, S. & Coleman, J. N. High-Concentration Solvent Exfoliation of Graphene. *Small* **6**, 864–871 (2010).
 23. van de Hulst, H. C. Applications to Chemistry. in *Light Scattering by Small Particles* 394–413 (Dover Publications, 1981).
 24. Xu, Y., Cao, H., Xue, Y., Li, B. & Cai, W. Liquid-phase exfoliation of graphene: An overview on exfoliation media, techniques, and challenges. *Nanomaterials* **8**, (2018).
 25. Liu, W., Tanna, V. A., Yavitt, B. M., Dimitrakopoulos, C. & Winter, H. H. Fast Production of High-Quality Graphene via Sequential Liquid Exfoliation. *ACS Appl. Mater. Interfaces* **7**, 27027–27030 (2015).
 26. Hamilton, C. E., Lomeda, J. R., Sun, Z., Tour, J. M. & Barron, A. R. High-Yield Organic Dispersions of Unfunctionalized Graphene. *Nano Lett.* **9**, 3460–3462 (2009).
 27. O’Neill, A., Khan, U., Nirmalraj, P. N., Boland, J. & Coleman, J. N. Graphene dispersion and exfoliation in low boiling point solvents. *J. Phys. Chem. C* **115**, 5422–5428 (2011).
 28. Israelachvili, J. Interactions Involving the Polarization of Molecules. in *Intermolecular and Surface Forces* 67–82 (Academic Press, 1992).
 29. Dresselhaus, M. S., Jorio, A., Hofmann, M., Dresselhaus, G. & Saito, R. Perspectives on carbon nanotubes and graphene Raman spectroscopy. *Nano Lett.* **10**, 751–758 (2010).
 30. Ferrari, A. C. *et al.* Raman spectrum of graphene and graphene layers. *Phys. Rev. Lett.* **97**, 1–4 (2006).
 31. Eckmann, A. *et al.* Probing the nature of defects in graphene by Raman spectroscopy. *Nano Lett.* **12**, 3925–30 (2012).
 32. Bracamonte, M. V., Lacconi, G. I., Urreta, S. E. & Foa Torres, L. E. F. On the Nature of Defects in Liquid-Phase Exfoliated Graphene. *J. Phys. Chem. C* **118**, 15455–15459 (2014).
 33. Song, G. *et al.* Strong fluorescence of poly (N-vinylpyrrolidone) and its oxidized hydrolyzate. *Macromol. Rapid Commun.* **36**, 278–285 (2015).
 34. Varrla, E. *et al.* SI for Large-scale production of size-controlled MoS₂ nanosheets by shear exfoliation. *Chem. Mater.* **27**, 1129–1139 (2015).

35. Backes, C. *et al.* Guidelines for exfoliation, characterization and processing of layered materials produced by liquid exfoliation. *Chem. Mater.* **29**, 243–255 (2017).

6. Conclusions

6.1 Summary

In this work, I have used rheological methods and colloid theory to advance the study of novel manufacturing processes, both those using colloids and those meant to develop new colloids.

6.1.1 UV-Curable Maskants for Electroplating

Through evaluation of the structure-property-performance relationships of UV-curable masks for electroplating, I developed a more fundamental understanding of desirable characteristics for these maskants. The shorter-chained burn-off materials showed greater adhesion and resistance to plating species than their peel-off counterparts. The focus on macro scale parts and the maskant mechanical properties represent a novel contribution to the UV-curable coating literature. In addition, this work can improve the throughput of turbine blade manufacturing due to fast curing times¹ and by allowing automation using robotic spraying systems. This can also reduce environmental impacts due to the elimination of toxic solvents^{1,2}.

6.1.2 Graphene Production by Liquid-Phase Shear Exfoliation

I have evaluated liquid viscosity and dielectric constant as previously unstudied parameters potentially relevant to the production of few-layer graphene by liquid-phase shear exfoliation. This is especially important to consider as large-scale exfoliation research moves away from sonication³, where higher viscosity reduces cavitation energy⁴ but could improve shear-based production. Neglect of these parameters could help explain previously unaccounted for variances in FLG production by solvents with similar surface energies and/or solubility parameters⁵. Similarly this may explain observed differences between a liquid's exfoliation performance and its dispersion stability^{6,7}.

Through a controlled shear rate study, I demonstrated that a higher viscosity liquid can produce more FLG by shear exfoliation than a lower viscosity liquid under identical conditions, as demonstrated by propylene glycol in comparison to the standard graphene solvent NMP. The great variance of exfoliated material concentration benzyl benzoate also suggests that its short- to medium-term instability may be due to its very low dielectric constant in comparison to propylene glycol and NMP. This was then followed up by a larger-scale study in an industrial impeller mixer, where the higher viscosity liquid produced equivalent quality (and potentially larger) material compared to that exfoliated in NMP, and at higher concentrations. This suggests exfoliation in more viscous solvents is feasible for the large-scale manufacture of FLG, especially as other mixing parameters may still need to be optimized for propylene glycol.

6.2 Future Work

6.2.1 UV-Curable Maskants for Electroplating

A major limit to the current study was the unphysical FTIR curing results for two of the peel-off maskants, limiting our understanding of the precursor materials. Work with known prepolymer lengths and chemistries or more accurate identification through FTIR without convoluting additives would enable better quantitative analysis of the observed trends between uncured flow behavior and cured material hardness. Raman spectroscopy could also potentially help identify species in the uncured material.

Additionally, comparisons to the literature on UV-curable clearcoats suggests a new approach to mask and coating evaluation. Prior work on UV-curable coatings in the context of clearcoats has focused on maximizing the resin's flexibility as a way to obtain the most generally useful materials, using pencil hardness as a quick assessment, after additives are introduced². While part of this may be attributed to the long-term nature of clearcoat deployment, it is reasonable to think this could also apply to maskant coatings, as both applications are meant to

protect the underlying substrate from exposure to a chemical species in the environment. However, the burn-off maskants showed better performance as plating barriers and are harder than the peel-off maskants. I observed a positive relationship between adhesion and maskant hardness that has also been observed in UV-curable clearcoats, suggesting the results are generalizable². In comparison to clearcoats, this hardness may be desirable in maskants, as the hardest mask was the best plating barrier, which we attribute to the difficulty of delaminating it compared to cohesive failure. This may also be related to its rheological behavior, as the uncured material's high yield stress and low-shear viscosity may prevent the microscale separations between the maskant and substrate from developing between application and curing. Thus, the "flexibility approach" of previous studies should be supplemented by a "rheological approach" looking at flow behavior to select appropriate precursor chain lengths.

6.2.2 Two-Dimensional Nanomaterial Production by Liquid-Phase Shear Exfoliation

6.2.2.1 *Fundamental Studies*

Much more work still needs to be done to better understand the role of viscosity in the exfoliation process. As benzyl benzoate did deviate from the hypothesized trend, more studies should be done with solvents of varying viscosity, but otherwise similar surface tensions, solubility parameters, and/or dielectric constants. Propylene glycol and NMP should be miscible, and given their close surface tension and dielectric values, a study of exfoliation in a series of binary mixtures of the solvents could show the trend of exfoliation concentration and viscosity with minimal confounding effects from other solvent properties. Engineered room temperature ionic liquids could also be used for this purpose. As a very basic approximation, the cation species of an ionic liquid determines most its physical properties, while the anion is mainly responsible for the chemical properties⁸. Thus, a study could be done using ionic liquids with the same anion, but with cations of increasing chain length, which would have increasingly higher

viscosities but similar chemical interactions. These studies would better quantify the effect of viscosity and could be used to validate the viscosity parameter in the simple shear exfoliation model (Chapter 3, section 3.2 and equations 3.1-3.6). Additionally, the layer thickness of the exfoliated material should be evaluated to determine if this is affected by the solvent viscosity, as no existing model offers a predictive explanation for the differences in mean thickness and polydispersity observed between different exfoliation liquids.

Similarly, there is still much to evaluate in the role of the exfoliation liquid's electronic and optical properties (see section 3.3), which could distinguish properties controlling exfoliation versus those controlling dispersion stability⁹. The observed difference in the absorbance-concentration relationship between NMP and PG shows that the common assumption of all FLG solvents having similar absorption coefficients^{10,11} is inadequate for evaluation of novel solvents with varying optical properties¹²⁻¹⁴. Improved quantification is needed to explain an observed settling result, shown in figure 6-1. After 9 months of storage, an FLG dispersion in PG appears

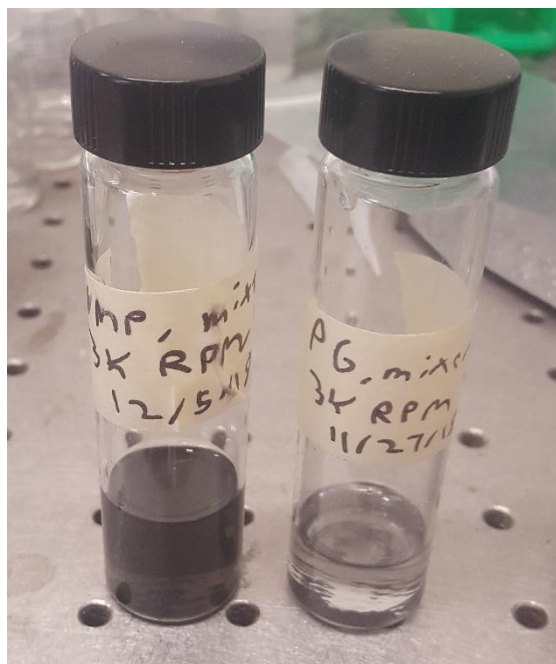


Figure 6-1. Vials of exfoliated FLG dispersions stored for at least 9 months, NMP on left and PG on right.

to have mostly settled out into aggregates, while an FLG dispersion exfoliated under identical conditions in NMP shows little settling. Given the calculated higher second virial coefficient B_2 in PG, and its higher viscosity, I would expect it to be at least as stable as NMP for storage at long timescales, if not more so. However, this may reflect the large error in my calculation of B_2 in NMP. More work should follow the analysis by

Dutta *et al.* as done in chapter 5¹⁵, to calculate B_2 of

FLG in various liquids, and more studies should measure the zeta potential^{3,16}. Improved quantification of these values would improve the theoretical understanding of colloidal stability of FLG dispersions. Dutta's, and this work, is also limited in its potential accuracy describing FLG because the scattering equations are based on spherical particles.

Given the many parameters that affect exfoliation and dispersion and simultaneous interest in many properties of the resulting exfoliated material, it is difficult to develop deep understanding of the process with studies primarily focusing on one variable. In addition, this makes it difficult to optimize the production process with given materials or for a specific application. This kind of problem, a complex process with multiple outcomes and objectives, is one that may benefit from the application of machine learning tools to discover new patterns in available information as well as guide further experimental studies¹⁷. Historically, soft matter has been given less focus in computational/machine learning studies in materials science due to greater modeling difficulties and the lack of large databases^{18,19}.

Early chemometrics research into graphene dispersibility²⁰ should be built on by experimental testing of more solvents under identical conditions following Hernandez *et al*⁶. This should be supported with standardized reporting of exfoliation set-ups to allow for study of varying mixing/exfoliation parameters, and standardized evaluations of graphene quality²¹, which could be combined to generate large-scale data sets appropriate for machine learning. Such standardized reporting is also necessary due to the poor classification scheme currently used for commercial graphene²² and would represent a major step forward along the international science and technology roadmap for graphene¹¹.

Finally, nearly all this work should be generalizable to other two-dimensional nanomaterials that can be produced from van der Waals solids, such as transition metal

dichalcogenide monolayers. Appropriately choosing a solvent based on the different electronic properties of the desired nanomaterial should be more efficient than just testing known graphene solvents for other 2D systems.

6.2.2.2 Applications of Two-Dimensional Nanomaterial Dispersions

Colloidal dispersions of two-dimensional nanomaterials have many potential uses, both as novel high-performance, and potentially multifunctional, fluids in themselves and as a platform for further manufacturing. For instance, there is an interest in using “nanofluids” for heat-transfer fluids with enhanced thermal properties due to the incorporation of conductive nanomaterials. In fact, propylene glycol-water mixtures are already candidates for graphene-based heat-transfer fluids²³, so FLG dispersions manufactured in PG could potentially be directly used or functionalized to improve stability²⁴. Graphene can also be added to lubricants to improve their tribological properties²⁵. Dispersions of 2D nanomaterials can be used as “inks” for printing or spray coating thin structures onto substrates²⁶ or could be incorporated into additive manufacturing.

As discussed in Chapter 3, a well-mixed graphene (or other 2D nanomaterial) dispersion is also useful for further chemical modification, and broadening the number of graphene solvents allows for a greater variety of chemical reactions. Dispersed graphene may be functionalized for multiple reasons. It can be modified with specific binders to form sensors^{27,28}. Graphene can be a support for molecules that break down pollutants^{27,29}. Functionalizing graphene with polymer chains should improve its dispersion stability in polymer nanocomposites³⁰⁻³³ as well as improve the resulting property enhancement³⁴.

6.3 Final Remarks

This dissertation has contributed to the fundamental understanding of advanced manufacturing processes using and producing colloidal materials. The conclusions drawn should

be generalizable to broader classes of materials, especially the studies on few-layer graphene produced by exfoliation. As development proceeds on technologies based on graphene and other 2D nanomaterials, there will be many opportunities for research to both better understand their colloidal behavior and improve the production of these materials for specific applications.

6.4 References for Conclusions

1. Nudelman, A. UV curable masking resins come of age. *Met. Finish.* **101**, 65–71 (2003).
2. Jusko, J. *et al.* *Ultraviolet (UV)-Curable Coatings for Aerospace Applications.* (2012).
3. Johnson, D. W., Dobson, B. P. & Coleman, K. S. A manufacturing perspective on graphene dispersions. *Curr. Opin. Colloid Interface Sci.* **20**, 367–382 (2015).
4. Liu, X. M. *et al.* Cavitation bubble dynamics in liquids of different viscosity. *2010 Symp. Photonics Optoelectron. SOPO 2010 - Proc.* 1–4 (2010).
doi:10.1109/SOPO.2010.5504305
5. Bergin, S. D. *et al.* Multicomponent Solubility Parameters for Single-Walled Carbon Nanotube–Solvent Mixtures. *ACS Nano* **3**, 2340–2350 (2009).
6. Hernandez, Y., Lotya, M., Rickard, D., Bergin, S. D. & Coleman, J. N. Measurement of Multicomponent Solubility Parameters for Graphene Facilitates Solvent Discovery. *Langmuir* **26**, 3208–3213 (2010).
7. Shen, J. *et al.* Liquid Phase Exfoliation of Two-Dimensional Materials by Directly Probing and Matching Surface Tension Components. *Nano Lett.* **15**, 5449–5454 (2015).
8. Stark, A. & Seddon, K. R. Ionic Liquids. in *Kirk-Othmer Encyclopedia of Chemical Technology* **26**, 836–920 (John Wiley & Sons, Inc., 2007).
9. Shen, J. *et al.* Surface Tension Components Based Selection of Cosolvents for Efficient Liquid Phase Exfoliation of 2D Materials. *Small* **12**, 2741–2749 (2016).
10. Hernandez, Y. *et al.* High-yield production of graphene by liquid-phase exfoliation of graphite. *Nat. Nanotechnol.* **3**, 563–568 (2008).
11. Ferrari, A. C. *et al.* Science and technology roadmap for graphene, related two-dimensional crystals, and hybrid systems. *Nanoscale* **7**, 4598–4810 (2015).
12. Nuvoli, D. *et al.* High concentration few-layer graphene sheets obtained by liquid phase exfoliation of graphite in ionic liquid. *J. Mater. Chem.* **21**, 3428–3431 (2011).
13. Mehrli, M. *et al.* Investigation of thermal conductivity and rheological properties of nanofluids containing graphene nanoplatelets. *Nanoscale Res. Lett.* **9**, 15 (2014).

14. Basic UV-Vis Theory, Concepts and Applications. *ThermoFisher Scientific* 1–28 (2013). Available at: <http://phystec.ir/images/UV.pdf>.
15. Dutta, N., Egorov, S. & Green, D. Quantification of Nanoparticle Interactions in Pure Solvents and a Concentrated PDMS Solution as a Function of Solvent Quality. *Langmuir* **29**, 9991–10000 (2013).
16. Liu, W. W., Wang, J. N. & Wang, X. X. Charging of unfunctionalized graphene in organic solvents. *Nanoscale* **4**, 425–428 (2012).
17. Butler, K. T., Davies, D. W., Cartwright, H., Isayev, O. & Walsh, A. Machine learning for molecular and materials science. *Nature* **559**, 547–555 (2018).
18. Berau, T., Andrienko, D. & Kremer, K. Research Update: Computational materials discovery in soft matter. *APL Mater.* **4**, (2016).
19. Ferguson, A. L. Machine learning and data science in soft materials engineering. *J. Phys. Condens. Matter* **30**, (2018).
20. Yousefinejad, S. & Hemmateenejad, B. A chemometrics approach to predict the dispersibility of graphene in various liquid phases using theoretical descriptors and solvent empirical parameters. *Colloids Surfaces A Physicochem. Eng. Asp.* **441**, 766–775 (2014).
21. Backes, C. *et al.* Guidelines for exfoliation, characterization and processing of layered materials produced by liquid exfoliation. *Chem. Mater.* **29**, 243–255 (2017).
22. Kauling, A. P. *et al.* The Worldwide Graphene Flake Production. *Adv. Mater.* **30**, 1–6 (2018).
23. Vallejo, J. P. *et al.* Flow behaviour of suspensions of functionalized graphene nanoplatelets in propylene glycol–water mixtures. *Int. Commun. Heat Mass Transf.* **91**, 150–157 (2018).
24. Agromayor, R. *et al.* Heat transfer performance of functionalized graphene nanoplatelet aqueous nanofluids. *Materials (Basel)*. **9**, (2016).
25. Zhao, J., Mao, J., Li, Y., He, Y. & Luo, J. Friction-induced nano-structural evolution of graphene as a lubrication additive. *Appl. Surf. Sci.* **434**, 21–27 (2018).
26. Naficy, S. *et al.* Graphene oxide dispersions: tuning rheology to enable fabrication. *Mater. Horizons* **1**, 326 (2014).
27. Perreault, F., Fonseca de Faria, A. & Elimelech, M. Environmental applications of graphene-based nanomaterials. *Chem. Soc. Rev.* **44**, 5861–5896 (2015).
28. Choi, W., Lahiri, I., Seelaboyina, R. & Kang, Y. S. Synthesis of Graphene and Its Applications: A Review. *Crit. Rev. Solid State Mater. Sci.* **35**, 52–71 (2010).

29. Khurana, I., Saxena, A., Bharti, Khurana, J. M. & Rai, P. K. Removal of Dyes Using Graphene-Based Composites: a Review. *Water, Air, Soil Pollut.* **228**, 180 (2017).
30. Sunday, D., Ilavsky, J. & Green, D. L. A Phase Diagram for Polymer-Grafted Nanoparticles in Homopolymer Matrices. *Macromolecules* **45**, 4007–4011 (2012).
31. McEwan, M., Egorov, S., Ilavsky, J., Green, D. L. & Yang, Y. Mechanical reinforcement of polymer nanocomposites: theory and ultra-small angle X-ray scattering (USAXS) studies. *Soft Matter* **7**, 2725 (2011).
32. Dutta, N. & Green, D. L. Impact of solvent quality on nanoparticle dispersion in semidilute and concentrated polymer solutions. *Langmuir* **26**, 16737–16744 (2010).
33. McEwan, M. & Green, D. L. Rheological impacts of particle softness on wetted polymer-grafted silica nanoparticles in polymer melts. *Soft Matter* **5**, 1705 (2009).
34. Layek, R. K. & Nandi, A. K. A review on synthesis and properties of polymer functionalized graphene. *Polymer (Guildf)*. **54**, 5087–5103 (2013).